



UNIVERSITÀ DEGLI STUDI DI TRIESTE

Dipartimento di Fisica

XXVI CICLO DEL DOTTORATO DI RICERCA
IN NANOTECNOLOGIE

MOLECULAR MODELING OF MULTIFUNCTIONAL NANOSTRUCTURED MATERIALS AND COATINGS

Settore scientifico disciplinare: ING-IND/24

Dottoranda:
Francesca Santese

Coordinatore:
Chiar.ma Prof.ssa Lucia Pasquato

Supervisore:
Chiar.mo Prof. Maurizio Fermeglia

Tutore:
Chiar.ma Prof.ssa Sabrina Pricl

Anno Accademico 2013-2014

ABSTRACT

MOLECULAR MODELING OF MULTIFUNCTIONAL NANOSTRUCTURED MATERIALS AND COATINGS

by

Francesca Santese

Nanostructured materials and coatings have the potential to change materials science significantly, as well as to provide a new generation of materials with a quantum improvement in properties. In this regard computational materials science becomes a powerful tool. It is able to rapidly reduce the time from concept to end product. Molecular simulation enables the prediction of properties of these new materials before preparation, processing, and experimental characterization, as well as a better understanding of the physical phenomena at the nanoscale level.

In this thesis we present several study cases in which we propose different computational recipes to deal with different important topics such as surface wettability, effect of nanoparticles size and shape and nanoparticles aggregation/dispersion.

In this context, we demonstrate the broad applicability of the molecular modelling and we ascertain that molecular simulation represent a powerful tool to understand and control the nanomaterials properties thus opening avenues for the *in silico* design of new materials.

Materiali e rivestimenti nanostrutturati possono potenzialmente apportare significativi cambiamenti nel campo della nanoscienze, nonché offrire una nuova generazione di materiali con caratteristiche e performance migliori. A questo proposito le tecniche computazionali

diventano uno strumento fondamentale, in grado di ridurre notevolmente i tempi che vanno dall'idea iniziale al prodotto finito. La simulazione molecolare permette infatti la previsione delle proprietà macroscopiche prima che i materiali vengano preparati e caratterizzati sperimentalmente; consente inoltre una migliore comprensione dei fenomeni fisici su scala nanometrica.

In questo lavoro di tesi sono presentati alcuni casi studio in cui vengono proposte diverse procedure computazionali per affrontare importanti aspetti come la bagnabilità della superficie, l'effetto della dimensione e della forma delle nanoparticelle e i loro meccanismi di aggregazione/dispersione.

In questo contesto, si è dimostrata la vasta applicabilità della modellazione molecolare evidenziando quindi come questa rappresenti un potente strumento per comprendere e controllare le proprietà finali di materiali nanostrutturati, aprendo così la strada ad una progettazione *in silico* di nuovi materiali.

Table of contents

1	INTRODUCTION	7
1.1	MOTIVATION AND RELEVANCE.....	7
1.2	OUTLINE	10
2	MODELING NANOMATERIALS	11
2.1	NANOMATERIALS.....	11
2.1.1	<i>Polymer Nanocomposite</i>	13
2.1.2	<i>Nanocomposite and nanostructured coatings</i>	14
2.1.3	<i>Design of new nanomaterials</i>	16
2.2	MOLECULAR MODELING	17
2.3	SIMULATION METHODS	21
2.3.1	<i>Atomistic methods</i>	21
2.3.2	<i>Mesoscale methods</i>	23
2.3.3	<i>Macroscale methods</i>	25
2.3.4	<i>Multiscale molecular modeling</i>	28
2.4	REFERENCES.....	31
3	POLYMER NANOCOMPOSITES WITH DIFFERENT NANOPARTICLES SHAPE	33
3.1	INTRODUCTION.....	34
3.2	SIMULATION PROCEDURE.....	36
3.2.1	<i>Atomistic molecular dynamics (MD) simulations</i>	37
3.2.2	<i>Mesoscale (MS) simulations</i>	39
3.2.3	<i>Finite elements (FEM) calculations</i>	42
3.3	RESULTS AND DISCUSSION.....	44
3.3.1	<i>Atomistic MD simulations</i>	44

3.3.2	<i>Mesoscale simulations</i>	47
3.3.3	<i>MicroFEM calculations of stack properties for intercalated PNCs</i>	50
3.3.4	<i>MicroFEM calculations of the properties for unmodified PNCs with interfaces</i>	51
3.3.5	<i>Macroscopic properties of all nanocomposite systems</i>	52
3.4	CONCLUSION	59
3.5	REFERENCES	60
4	IN SILICO ESTIMATION OF POLYMER SURFACE WETTABILITY	63
4.1	INTRODUCTION	64
4.2	COMPUTATIONAL DETAILS AND SIMULATION METHODOLOGY	68
4.2.1	<i>Pathway 1 (P1)</i>	69
4.2.2	<i>Pathway 2 (P2)</i>	73
4.3	EFFECT OF SURFACE NATURE ON WETTING BEHAVIOR OF AMORPHOUS POLYMERS	79
4.3.1	<i>Result from path 1</i>	79
4.3.2	<i>Wettability analysis of fluorinated amorphous surfaces</i>	87
4.4	CONCLUSIONS	97
4.5	REFERENCES	97
5	CHARACTERIZATION OF POLYMER-GRAFTED SILICA-BASED POLYMER NANOCOMPOSITES	100
5.1	INTRODUCTION	101
5.2	MATERIALS AND METHODS	102
5.2.1	<i>SANS experiments</i>	104
5.2.2	<i>SAXS experiments</i>	104
5.2.3	<i>Transmission electronic microscopy</i>	105
5.2.4	<i>Computational details</i>	105
5.3	RESULTS AND DISCUSSION	114
5.3.1	<i>Aggregation vs dispersion</i>	117
5.3.2	<i>Conclusions</i>	123
5.4	REFERENCES	124
6	CONCLUSIONS	126

1

Introduction

1.1 Motivation and relevance

Nanostructured materials have the potential to change materials science significantly, as well as to provide a new generation of materials with a quantum improvement in properties. The variety of nanomaterials is great, and their range of properties and possible applications appear to be enormous, from extraordinarily tiny electronic devices, including miniature batteries, to biomedical uses, and as packaging films, superabsorbants, and parts of automobiles. Hundreds of products containing nanomaterials are already in use and the number of products produced by nanotechnology or containing nanomaterials entering the market is increasing. Current applications include healthcare (in targeted drug delivery, regenerative medicine, and diagnostics), electronics, cosmetics, textiles, information technology and environmental protection.

Over the past decade, nanomaterials, notable for their extremely small feature size, have been the subject of enormous interest. As a result

of recent improvement in technologies to see and manipulate these materials, the nanomaterials field has seen a huge increase in funding from private enterprises and government, and academic researchers within the field have formed many partnerships.

Although widespread interest in nanomaterials is recent, the concept was raised over 50 years ago. Physicist Richard Feynman delivered a talk in 1959 entitled "There's Plenty of Room at the Bottom", in which he commented that there were no fundamental physical reasons that materials could not be fabricated by maneuvering individual atoms. Nanotechnology advanced rapidly in the 1980s with the invention of Scanning Tunneling Microscope (STM) and Atomic Force Microscope (AFM) which allows us to study nanoparticles which are not visible in the conventional microscopes otherwise. Within the last 20 years, many research institutions have recognized the need for a more systematic approach to new materials development, in order to predicted the properties of new materials before preparation, processing, and experimental characterization. This approach was one that would combine interdisciplinary research, new advances in computational modeling and simulation, and critical laboratory experiments to rapidly reduce the time from concept to end product.

In this regard computational materials science becomes a powerful tool since it involves and enables the visualization of concepts and materials processes which are otherwise difficult to describe or even imagine. Among other things, this field allows materials to be designed and tested efficiently. Computational materials science draws from physics and chemistry, but focuses on constitutive descriptions of materials that are useful in formulating macroscopic models of material performance. The benefits of the computational materials science approach are threefold. First, it encourages a reduced reliance on costly trial and error of the traditional approach to materials research. Second, it increases the confidence that new materials will possess the desired properties when scaled up from the laboratory level, so that lead-time for the introduction of new technologies is reduced. Third, the computational materials science approach lowers the likelihood of conservative or compromised designs that might have resulted from reliance on less-than-perfect materials.

Molecular modeling and simulation combines methods that cover a range of size scales in order to study material systems. These range from the sub-atomic scales of quantum mechanics(QM), to the atomistic level of molecular mechanics (MM),molecular dynamics (MD), to the micrometer focus of mesoscale modeling, to continuum scale with finite element methods (FEM).

In the last decades virtual experiments based on quantum/molecular mechanics theories (MQ/MM) and on molecular dynamic (MD) techniques have opened avenues in the calculation and prediction of structural, thermodynamic and transport properties of different kind of molecules ranging from small molecules up to synthetic and natural macromolecules. The big advantages of these microscopic level based techniques can be summarized as (a) a better comprehension and interpretation of the experimental results, (b) an a priori semi-quantitative prediction of the experimental results and, last but not least, (c) the possibility of interpolating and extrapolating experimental data in regions in which experiment are difficult or even impossible to carry out.

Mesoscale models represent solid materials, fluids, and gases using larger fundamental units than molecular models. Computer simulation determines the structure, properties and dynamics of these models. Mesoscale methods are applicable to larger systems over far longer length and time scales than molecular simulation. They permit to study complex liquids, polymer blends, and structured materials on the nanometer to micron scale. The possibility of predicting the nanostructure at mesoscale level opens up the design of the material 'in silico' by modifying the composition and the interactions in the system thus performing a 'what if' analysis that is the basis of the design procedure of the material.

Finite element methods allows to calculate structural, thermal, mechanical and transport properties of materials at macroscopic level, outputs needed for the material designer.

Multiscale simulation can be defined as the enabling technology of science and engineering that links phenomena, models, and information between various scales of complex systems. The idea of multiscale modeling is straightforward: one computes information at a smaller (finer) scale and passes it to a model at a larger (coarser) scale by leaving

out, degrees of freedom. Multiscale molecular modeling poses formidable challenges thanks to the huge range of length and time scales involved.

In the present work we tackle several study cases in which we propose different computational recipes, according to the particularity of the system of interest, based on molecular modeling techniques. Our aim is to demonstrate that molecular simulation represent a powerful tool to understand and control the nanomaterials properties and to study important topics such as surface wettability, effect of nanoparticles size and shape and nanoparticles aggregation/dispersion, thus opening avenues for the *in silico* design of new materials.

1.2 Outline

The present Chapter represents a brief introduction of the work ,motivations and objectives of the thesis are presented here. Chapter 2 consist in a review of the current research in the field of nanomaterials, stressing on the importance of the interface phenomena in this field, and in an explanation of the different molecular modeling techniques used in the present work. The core of this work is reported in the following chapters where we analyze different aspects of a variety of polymeric systems, in order to demonstrate the broad applicability of the molecular modeling. In Chapter 3 we will presenta multiscale computational approach to characterize a different set of polymer-based nanocomposites (PNCs) obtained with full/partial dispersion of different nanofillers with different size and shape in different polymeric matrices. In Chapter 4a molecular dynamics (MD) based recipe will proposed to investigate the wetting behavior of different polymeric solid surfaces, with different degree of hydrophobicity/hydrophilicity, in the presence of different solvent nanodroplets, as water, oil and a mixture of water and surfactants. In Chapter we study the dispersion/aggregation mechanism of nanocomposites made of polystyrene grafted-silica nanoparticles mixed with free chains of the same polymer using a combination of scattering (SAXS), imaging (TEM), and multiscale molecular simulation techniques. Finally, in Chapter 6conclusions and future perspectives will exposed.

2

Modeling nanomaterials

2.1 Nanomaterials

The field of nanoscience and nanotechnology which deals with materials and structures having dimensions that measure up to billionth of a meter (nanometer) extended the applications of physics, chemistry, biology, engineering and technology into infinitesimal length scales. Now, at nanoscale one enters a world where physics and chemistry meet and develop novel properties of matter. The leading advantage of this size regime is the large surface area/volume ratio exhibited by nanomaterials. Accordingly, this translates to a very high surface reactivity with the surrounding surface, ideal for catalysis or sensor applications. Further, since biological systems feature the systematic organization of nanoscale materials (e.g., proteins are 1–20 nm in size, the diameter of DNA is ca. 2.2 nm), being able to fabricate materials in this size regime holds promise for

artificial components within cells to diagnose/fight diseases, illnesses, viruses. Another key benefit for nanomaterials is the ability of varying their fundamental properties (e.g., magnetization, optical properties, color, melting point, hardness, etc.), relative to bulk materials without a change in chemical composition. Although bulk properties such as melting point and hardness are related to the enhanced surface interactions among nanoparticulates, the size-tunable electronic properties are due to quantum confinement effects. The so-called quantum size effect describes the physics of electron properties in solids with great reductions in particle size. This effect does not come into play by going from macro to micro dimensions. However, it becomes dominant when the nanometer size range is reached. Quantum effects can begin to dominate the behavior of matter at the nanoscale - particularly at the lower end (single digit and low tens of nanometers) - affecting the optical, electrical and magnetic behavior of materials. The bulk properties of any material are merely the average of all the quantum forces affecting all the atoms that make up the material. As you make things smaller and smaller, you eventually reach a point where the averaging no longer works and you have to deal with the specific behavior of individual atoms or molecules - behavior that can be very different to when these atoms are aggregated into a bulk material.

Surfaces and interfaces are also important in explaining nanomaterial behavior. In bulk materials, only a relatively small percentage of atoms will be at or near a surface or interface (like a crystal grain boundary). In nanomaterials, the small feature size ensures that many atoms, perhaps half or more in some cases, will be near interfaces. Surface properties such as energy levels, electronic structure, and reactivity can be quite different from interior states, and give rise to quite different material properties.

Not only in academia, but also in industries, the impact of the nanomaterials field is significantly increasing such as in ceramics, chemical polishing agents, scratch-resistant coatings, stain-resistant trousers, cosmetics, sunscreens, etc. Increased strength and hardness combined with engineering levels of ductility and toughness could provide a new generation of structural materials and coatings. Ceramic coatings with reduced thermal conductivity, elastic modulus, and higher

thermal expansion coefficient would make attractive thermal barrier coatings.^[1] Thus, synthesis of various nanoscale structures/particles has gained the interest for developing new nanomaterials and devices.

2.1.1 Polymer Nanocomposite

The idea behind is to use building blocks with dimensions in the nanometer range to design and create new materials with unprecedented flexibility and improvements in their physical properties. When designing the nanocomposite, scientists can choose constituents with different structures and composition and hence properties, so that materials built from them can be multifunctional. As a general definition a nanocomposite is an inorganic or organic matrix reinforced by nanoscale particles or nanostructures which are dispersed through the bulk material. In general nanocomposite materials can demonstrate different mechanical, electrical, optical, electrochemical, catalytic, and structural properties which are different from that of the individual components. Apart from the properties of the individual components, interfaces in a nanocomposite play an important role in determining the overall properties of the material. Due to the high surface area of nanostructures, nanocomposites present many interfaces between the intermixed phases, and often the special properties of the nanocomposite are a consequence of the interaction of its phases at the interface. In comparison, the interface in conventional composites constitute a much smaller volume fraction of the bulk material.

Since polymeric materials are rapidly replacing more traditional inorganic materials, such as metals, polymer nanocomposites, in last few decades, have become worldwide research interest for developing polymeric materials with improved/desired properties. Therefore polymer nanocomposites are a new class of composites that are particle-filled polymers for which at least one dimension of the dispersed particles is in the nanometer range. Nanoscale fillers include:

- a) Nanoparticles: When the three dimensions of particulates are in the order of nanometers, they are referred as equi-axed (isodimensional) nanoparticles or nanogranules or nanocrystals. Example silica.
- b) Nanotubes: When two dimensions are in the nanometer scale and the third is larger, forming an elongated structure, they are generally

referred as nanotubes or nanofibers/nanowhiskers/nanorods. Example, carbon nanotubes (CNTs), cellulose nanowhiskers.

- c) Nanolayers: The particulates which are characterized by only one dimension in nanometer scale are nanolayers/ nanosheets. These particulate is present in the form of sheets of one to a few nanometer thick to hundreds to thousands nanometers long. Clay (layered silicates), layered double hydroxides (LDHs).

Polymer nanocomposites offer the possibility of substantial improvements in material properties such as shear and bulk modulus, yield strength, toughness, film scratch resistance, optical properties, electrical conductivity, gas and solvent transport, among many with only very small amounts of nanoparticles (NPs) dispersed in the polymer matrix. The dramatically larger chain-particle interface area in the case of nanocomposites compared to microcomposites makes effects appearing negligible in microcomposites very prominent in nanocomposites [2]. The state of the dispersion of NPs in the polymeric matrix often has a large impact on the properties of polymeric materials. Additionally, the NPs geometry can also have a large impact on property changes, since it can affect both surface energetics and surface to volume ratio [3-6]. From a rheological point of view, a direct consequence of incorporation of fillers in molten polymers is a significant change in their steady shear viscosity behavior and the viscoelastic properties [7,8].

However, despite the large volume of literature published on the relationships between the nano-scale structural variables and macroscale physical and mechanical properties of polymer nanocomposites over the last 20 years, the understanding of the basic physical origin of these large property changes remains in its infancy. Moreover, since the polymer-nanocomposites are the staple of modern polymer industry, the ability to predict their mechanical properties is indispensable for future design and commercial use of these materials.

2.1.2 Nanocomposite and nanostructured coatings

As coating are integral to virtually any imaginable product or structure, nanomaterials are having a great impact in this field. Today's nanotechnology coating include polymer-nanoparticle and sol-gel composite coatings for improving scratch and UV resistance, IR reflection,

anti-microbial and self-cleaning activity, corrosion resistance, gas barrier properties and superhydrophobic characteristics. Nanotechnology application in coatings have shown remarkable growth in recent years. This is a result of two main factors: 1) increased availability of nano-scale materials such as various types of nanoparticles, and 2) advancement in processes that can control coating structure at the nanoscale. Another important reason for this growth is the potential of nanotechnology to address many performance challenges presented by the vast range of products and structures that coatings are an integral part of. Applications of coatings include interior and exterior house paints, interior furnishings, glass and facade coating for high-rise buildings, all types of transportation vehicles and structures (automobiles, airplanes, bridges, road markings, marine vessels, spacecrafts, etc.), and a wide variety of industrial and non-industrial maintenance coatings. At a much smaller scale, coatings are used in numerous electronic products and biomedical coatings. Coating layer thickness can vary from hundreds of micrometers (e.g. anti-skid coating on the deck of an aircraft carrier) to less than 100 nm (e.g. insulating coatings in microchips). Coatings play one or more of three key roles in these applications: 1) improve product's esthetic appeal, 2) protect the substrate from a wide range of abuses (e.g. damage due to scratches or impact, corrosion and long term weathering), and 3) provide specialized functionality to the product (e.g. conductivity, insulation, water repellency, and heat reflectance).^[9]

All of the coatings contain nanoscale structural features, and as such, are defined nanostructured. Incorporation of nanoscale inorganic materials to organic coatings has become one of the most prevalent approaches leading to nanocomposite coating products. Dispersing nanoparticles, instead of larger particles allows a coating formulator to increase the interfacial material content significantly. As we already said, the properties of the interfacial material at the interface between two materials are different from the bulk properties of each material. If the interfacial material has better properties that are not offered by individual materials of the composite, this approach would maximize such benefits.

The major challenges facing continued growth of nanocomposite based materials can be divided into three main categories: 1) dispersion, 2) characterization, 3) material cost.

The material cost has come down in recent years with increasing number of nanoparticles suppliers, improved manufacturing methods, and increased sales volumes.

Nanoscale dispersion is critical for realizing the potential benefits of incorporating nanoparticles in coatings. The high surface area of dispersed nanoparticles can significantly increase the dispersant demand. High viscosity caused by finely dispersed nanoparticles is another problem that needs to be addressed. The large surface area can increase viscosities due to the increase in interfacial forces and limit the amount of nanoparticles that can be incorporated. Adding the right surface functionality to address dispersibility and viscosity is another approach to address dispersion issue. In addition to promoting dispersion, functionalizing the particle surface enables the nanoparticle to be covalently linked to the organic resin matrix. The dispersion matter is one of the topic discussed in the present work; in chapter 5 it will be treated for a particular polymer-based nanocomposite system.

Surface characterizations requires also experimental advanced techniques such as Scanning Probe Microscopy (SPM) (e.g. Atomic Force Microscopy) and Scanning Electron Microscopy (SEM). Film cross-sectional analysis requires techniques such as Transmission Electron Microscopy (TEM), SEM, X-ray and neutron scattering. In more than one study case presented in this thesis it will be shown also the validation of our procedures through the comparison between simulation results and experimental results.

2.1.3 Design of new nanomaterials

The preparation of these nanomaterials is still largely empirical, and there isn't yet a good degree of control of their final properties. Optimizing of the processing conditions, designing of the new structures with the required properties as well as better understanding of the physical phenomena in polymers imply extensive trial-and-error experimental studies which can be both expensive and time-consuming. In order to reduce the experimental efforts in synthesis and optimization of material properties, computer simulations of the systems of interest can be very useful. Such simulations allow systematic variation of structural or physical parameters of the materials and can significantly lower

experimental costs in predicting the properties of new materials. These approaches may eventually allow for screening of a greater breadth of potential material chemistries than those that can be tried by experimental testing alone.

2.2 Molecular modeling

In the recent years, modeling and computer simulation have increasingly become fundamental tools in many branches of science and engineering. These techniques are generally intended for investigating the inner molecular arrangements of nanostructured materials as well as for predicting macroscopic properties of new materials before their synthesis. This approach can be very useful especially for those materials which present nanoscale features, as long as experimental characterization and manipulation at this scale represent an extremely difficult task.

There are many levels at which modeling can be useful, since in the computational material field have been developed different techniques for spanning both the length and time scales associated with analyses that describe material behavior. The starting point is a quantum description of materials; this is carried forward to an atomistic scale for initial model development. Models at this scale are based on molecular mechanics or molecular dynamics. At the next scale, the models can incorporate micro-scale features and simplified constitutive relationships. Further progress up the scale leads to the meso level that rely on combinations of micromechanics and well-established theories such as elasticity. The last step towards engineering-level performance is to move from mechanics of materials to structural mechanics by using methods that rely on empirical data, constitutive models, and fundamental mechanics.^[10]

However it is necessary to ensure that these methods can be applied routinely and successfully. Thus of primary importance are the validity and usability of each method on its own, followed by their interoperability in a common and efficient user environment. Of equal importance is the integration of the simulation methods with experiment. In modern materials research and development, one needs to be able to move from experimental knowledge to simulation and back again, requiring multiple input-output relationships at a range of materials length and time scales. The validation of methods across the complete

range of length and time scales requires advances in measurement sciences as well as advances in theory and models, coupled with integrated, interdisciplinary research. In Figure 2.1 is reported the comparison between simulation and measurement methods through length and time scales.

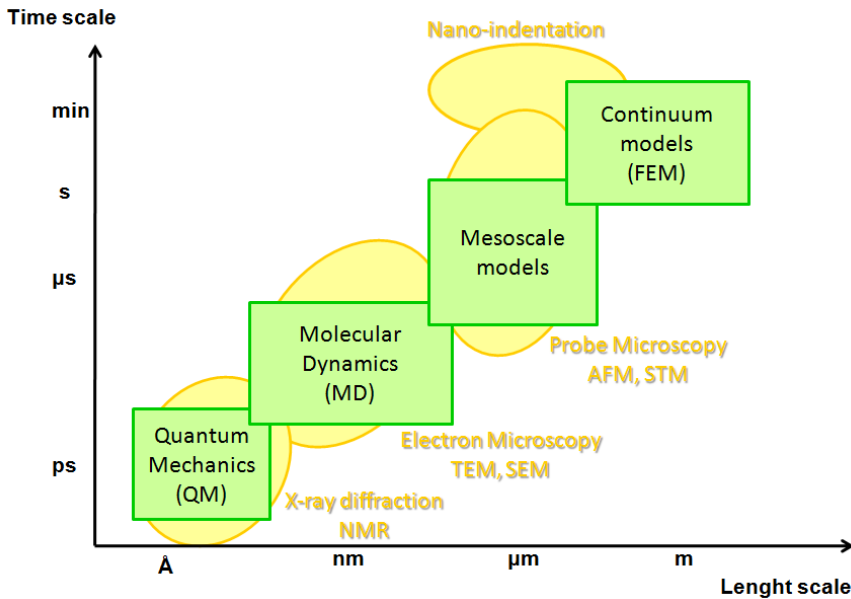


Figure 2.1: comparison between simulation and measurement methods through length and time scale.

Microscopy has consistently been a primary source of information on the fundamental structure of materials. Prior to the 1940s, microscopy was limited in resolution by the wavelength of visible light (approximately 10^{-6} - 10^{-7} m). The discovery of the Transmission Electron Microscope(TEM) occurred in the early 1940s and the first commercial electron microscopes became available around 1965. The Scanning Electron Microscope(SEM) is a microscope that uses electrons rather than light to form an image by scanning the beam across the specimen. Beginning with the scanning tunneling microscope (STM) in 1981, experimentalists developed new techniques and devices for discerning the most basic unit of materials, the atom. Instruments that use variations of the principles of the STM are often called scanning probe microscopes (SPM). All of these microscopes work by measuring a local property –

such as height, optical absorption, or magnetism – with a probe or “tip” placed very close to the sample. A successor to the STM, atomic force microscopy (AFM), works by measuring attractive or repulsive forces between the tip and the sample, and converting the basic displacement information of this tip into pictures of atoms on or in surfaces. Electron microscopes are strictly imaging devices, while the probe microscopes have some utility as imaging devices and in manipulation or characterization of materials. However, to date, the accuracy and repeatability of basic force/displacement measurements taken using probe microscopy has been as subject of debate. Because of this uncertainty, it appears that accurate, quantitative material testing is currently limited to devices that resolve only down to the microscale. Nanoindentors are commercial devices, built by using micro-electro-mechanical-systems, that operate at this resolution and they can be constructed with a high degree of repeatability and will operate under a range of environmental conditions. The nanoindenter is a high-precision instrument for the determination of the localized mechanical properties of thin films, coatings and substrates.^[10]

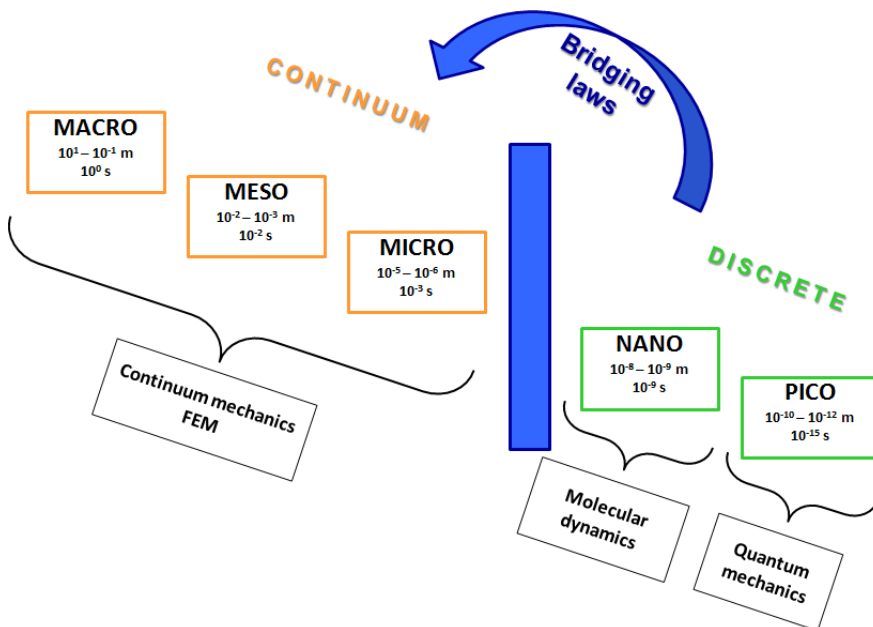


Figure 2.2: In order to bridge the gap between the discontinuous nano-scale structure and continuum macroscale models, it is recognized that physics-based bridging laws are needed.

In order to apply modeling and computer simulation to enhance the development of nanostructured materials systems, it is necessary to consider the structure–property relationships. These relationships relate the intrinsic structure of the material to the desired engineering-level property or performance. To this purpose it is necessary to resort to multiscale simulation method in order to move from one length scale to another and from one model to another. Multiscale modeling and simulation aims at linking the different length and time scales, bridging different models and computational methods in order to predict macroscopic properties and behavior from fundamental molecular processes [11,12,13]. The intent is to assist the material developer by providing a rational approach to material development and concurrently assist the structural designer by providing an integrated analysis tool that incorporates fundamental material behavior.

The problem here is that the method of coarsening the description from atomistic to mesoscale or mesoscale to continuum is not trivial. In order to bridge the gap between the discontinuous nano-scale structure and continuum macroscale models, it is recognized that physics-based bridging laws are needed (Figure 2.2). But classical continuum mechanics cannot be applied when the length scale of heterogeneity is below 20 nm [14,15]. On the other hand, molecular dynamics (MD) simulations are limited to nano-scale and cannot deal with the micro-scale sized bodies. Moreover the coarsening from QM to MD relies on basic principles and can be easily generalized in a method and in a procedure, while the coarsening at higher scales is system dependent.

Scale integration can be done using two different approaches: sequential and concurrent. The former is based on a hierarchical combination of different methods relevant to each scale, in which quantities calculated at one level are used as parameters for models with different characteristic dimensions. The latter, on the contrary, combines several computational methods in a general model in which events at different scales are considered simultaneously and interacts with each other [16]. In Chapter 2.3.4 we will illustrate our multiscale procedure that can be regarded as a sequential parameter – passing process.

2.3 Simulation methods

Several methods suitable for particular length and time scales are available to treat aspects of materials phenomena that operate only over those scales. In this Chapter, we will present a summary of the main simulation methods we principally employed in this thesis.

2.3.1 Atomistic methods

The modeling and simulation methods at molecular level usually employ atoms or small atom clusters (in coarse-grain approaches) as the basic units considered. These models aim at investigating thermodynamics and kinetics of the formation, molecular structure and interactions.

Beyond Quantum Mechanical (QM) methods, which incorporate quantum effects and are applicable only to very small systems due to their computational cost, the most popular methods include molecular mechanics (MM), Molecular Dynamics (MD) and Monte Carlo (MC).

MM methods can establish the minimum-energy structure statically and molecular dynamics can resolve the nanosecond-scale evolution of a molecule or molecular assembly. These approaches can model both bonded and nonbonded forces (e.g., Van derWaals and electrostatic).

MC methods, conversely, generate configurations of a system by making random changes to the positions of its elements, using a special set of criteria to decide whether or not to accept each new configuration. Amongst the different MC algorithms which have been developed, the Rotational Isomeric State (RIS) method^[17] represents one of the most common for the generation of polymer chains configurations.

2.3.1.1 Molecular Dynamic (MD)

MD is a computer simulation technique that allows one to predict the time evolution of a system of interacting particles (e.g., atoms, molecules) and estimate the relevant physical properties. The information generated from MD simulations are atomic positions, velocities and forces from. The conversion of this information to macroscopic observables such as pressure, energy, heat capacities, etc., can be obtained by means of statistical mechanics. Molecular dynamics simulation techniques are also

widely used to help interpret experimental results from X-ray crystallography and nuclear magnetic resonance spectroscopy.

In classical MD, the particle movement in the simulation is driven by the forces on each particle which is described by a set of functions, the force field, used to describe how the particles interact. By using Newton's second law to calculate a trajectory, one only needs the initial positions of the atoms, an initial distribution of velocities and the acceleration, which is determined by the gradient of the potential energy function. In a molecular dynamics simulation, the time dependent behaviour of the molecular system is obtained by integrating Newton's equations of motion:

$$F_i(t) = m_i \frac{d^2 r_i}{dt^2} \quad (2.1)$$

Where F_i is the force acting on the i th atom or particle at time t which is obtained as the negative gradient of the interaction potential U , m_i is the atomic mass and r_i the atomic position. A physical simulation involves the proper selection of interaction potentials, numerical integration, periodic boundary conditions, and the control of pressure and temperature to mimic physically meaningful thermodynamic ensembles.

The interaction potentials together with their parameters, i.e., the so-called *force field*, describe in detail how the particles in a system interact with each other, i.e., how the potential energy of a system depends on the particle coordinates. Such a forcefield may be obtained by quantum methods, empirical methods or quantum-empirical method. The criteria for selecting a forcefield include the accuracy, transferability and computational speed.

A typical interaction potential U may consist of a number of bonded and nonbonded interaction terms, which can be calculated for each of the N particles.

$$U(r_1, r_2, \dots, r_N) = U_{bond} + U_{angle} + U_{torsion} + U_{inversion} + U_{vdw} + U_{electrostatic} \quad (2.2)$$

The first four terms represent bonded interactions, i.e., bond stretching U_{bond} , bond-angle bend U_{angle} , dihedral angle torsion $U_{torsion}$ and inversion interaction $U_{inversion}$, while the last two terms are non bonded

interactions, i.e., van der Waals energy U_{vdw} and electrostatic energy $U_{electrostatic}$.

Usually, equations of motion are integrated applying one of the many algorithms using finite difference methods.

MD simulations can be performed in many different ensembles, such as microcanonical (NVE), canonical (NVT) and isothermal–isobaric (NPT). The constant temperature and pressure can be controlled by adding an appropriate thermostat and barostat.^[16]

The result of the simulation is a time series of conformations or the path followed by each atom.

2.3.2 Mesoscale methods

Coarse-graining the MD simulation increases the time scale accessible by about two orders of magnitude. Although molecular dynamics methods provide the kind of detail necessary to resolve molecular structure and localized interactions, this fidelity comes with a price: both the size and time scales of the model are limited by numerical and computational boundaries. To help overcome these limitations, coarse-grained methods are available that represent molecular chains as simpler models. Although the coarse-grain models lack the atomistic detail of MD, they do preserve many of the important aspects of the chemical structure and allow for simulation of material behavior above the nano-scale^[18,19], characteristic dimensions range from hundreds of nanometers to microns.

Mesoscale methods aim at linking microscale methods, i.e. atom based simulations, with macroscale methods based on continuum models. Various simulation methods have been proposed to study the mesoscale structures, most common being Brownian Dynamics (BD), Dissipative Particle Dynamics (DPD), Lattice Boltzmann (LB), time–dependent Ginsburg–Landau (TDGL) theory, and Dynamic Density Functional Theory (DDFT). In these methods, a molecule is usually treated with a field description or microscopic particles that incorporate molecular details implicitly. Therefore, they are able to simulate the phenomena on length and time scales currently inaccessible by the classical MD methods.

DPD has been chosen for mesoscale modelling in this work and will be treated in more detail below.

2.3.2.1 Dissipative Particle Dynamic (DPD)

DPD was originally developed by Hoogerbrugge and Koelman.^[20,21] It can simulate both Newtonian and non-Newtonian fluids, including polymer melts and blends, on microscopic length and time scales. Similar to molecular dynamics (MD), DPD is a particle based method. However, its elementary unit is not a single atom, but groups of atoms or molecules, referred to as beads, whose movement is determined by forces resulting from mutual direct interactions and dissipative and random contributes.

The DPD interaction is mesoscopic since the internal degrees of freedom of the fluid elements are ignored and only their center of mass motion is resolved. If the mass of all particles is set equal to unity, the time evolution of the positions ($\mathbf{r}_i(t)$) and momenta ($\mathbf{p}_i(t)$) is governed by Newton's equations:

$$\frac{d\mathbf{r}_i}{dt} = \mathbf{v}_i(t) \quad \frac{d\mathbf{v}_i}{dt} = \mathbf{f}_i(t) \quad (2.3)$$

where the mass of each particle i is set to unity, and \mathbf{r}_i , \mathbf{v}_i , and \mathbf{f}_i are the position vector, velocity, and total force, respectively, acting on particle i .

The force acting on the particles, which is pairwise additive, can be decomposed into three elements: a conservative (\mathbf{F}_{ij}^C), a dissipative (\mathbf{F}_{ij}^D), and a random (\mathbf{F}_{ij}^R) force. Accordingly, the effective force \mathbf{f}_i acting on a particle i is given by:

$$\mathbf{f}_i = \sum_{i \neq j} \left(\mathbf{F}_{ij}^C + \mathbf{F}_{ij}^D + \mathbf{F}_{ij}^R \right) \quad (2.4)$$

where the sum extends over all particles within a given distance r_c from the i th particle. This distance practically constitutes the only length scale in the entire system.

The conservative force is a soft repulsion, given by:

$$\mathbf{F}_{ij}^C = \begin{cases} a_{ij}(1-r_{ij})\hat{\mathbf{r}}_{ij} & (r_{ij} < 1) \\ 0 & (r_{ij} \geq 1) \end{cases} \quad (2.5)$$

where a_{ij} is the maximum repulsion between particles i and j , r_{ij} is the magnitude of the particle-particle vector $\mathbf{r}_{ij} = \mathbf{r}_i - \mathbf{r}_j$, and $\hat{\mathbf{r}}_{ij}$ is the unit

vector joining particles i and j . The other two forces, \mathbf{F}_{ij}^D and \mathbf{F}_{ij}^R , are both responsible for the conservation of the total momentum in the system, and incorporate the Brownian motion into the larger length scale. They are given by the following expressions:

$$\mathbf{F}_{ij}^D = -\gamma \omega^D(r_{ij})(\hat{\mathbf{r}}_{ij} \cdot \mathbf{v}_{ij})\hat{\mathbf{r}}_{ij} \quad (2.6)$$

$$\mathbf{F}_{ij}^R = \sigma \omega^R(r_{ij})\theta_{ij} \hat{\mathbf{r}}_{ij}$$

where $\mathbf{v}_{ij} = \mathbf{v}_i - \mathbf{v}_j$, ω^D and ω^R are r -dependent weight functions tending to zero for $r = r_c$, and θ_{ij} is a randomly fluctuating variable with zero mean and unit variance. It has been shown that one of the two weight functions in Equation 2.6 can be chosen arbitrarily, thereby fixing the other weight function. However, the weight function and constants should obey:

$$[\omega^R(r)]^2 = \omega^D(r) \quad \sigma^2 = 2\gamma k_B T \quad (2.7)$$

where k_B is the Boltzmann constant.

Further incorporation of chain molecules simply requires the addition of a harmonic spring force between the beads allowing them to interconnect to highly complex topologies:

$$\mathbf{F}_{ij}^{spring} = K(\mathbf{r}_{ij} - \mathbf{r}_{eq}) \quad (2.8)$$

where K is the spring constant and \mathbf{r}_{eq} is the equilibrium spring length. Many different formulations of the DPD method have been proposed, i.e. with inclusion of angle potentials and electrostatics.^[22,23]

2.3.3 Macroscale methods

Macroscale methods are those simulation techniques in which models can be regarded as representative of the average structure and properties of the whole material and simulations can be performed regardless of the molecular processes occurring at the microscale. Macroscale methods allow the calculation of some specific macroscopic property (i.e. Young's modulus, electrical conductivity, gas permeability, ...) of a material by considering a continuous distribution of its components throughout its volume, ignoring discrete atomic and molecular structures and their influence on system behaviour. These

methods aim at representing an heterogeneous material as an equivalent homogeneous one.

Such a description could be as well suited for the definition of micromechanics according to some authors,^[16] for which micromechanics model provides a transition from the microscale to the macroscale, bridging and determining relationship between microstructures and macroscopic (mechanical) properties. Micromechanics assumes small-deformation continuum mechanics; continuum mechanics, in general, assumes uniform material properties within the boundaries of the problem. At the microscale, this assumption of uniformity may not hold and hence the micromechanics method is used to express the continuum quantities associated with an infinitesimal material element in terms of the parameters that characterize the structure and properties of the micro-constituents of the element.^[24]

A central theme of micromechanics models is the development of a representative volume element (RVE) that is a statistical representation of the local continuum properties. The RVE is constructed to ensure that the length scale is consistent with the smallest constituent that has a first-order effect on the macroscopic behavior.^[25] The RVE is then used in a repeating or periodic nature in the full-scale model. Defining RVE and its minimum dimensions is obviously a non trivial task and amenable of different interpretations. Besides setting the RVE, macroscale methods usually involve the definition of appropriate constituent laws and implementation of relationships between structural features and macroscopic properties.

Possible macroscale modeling strategies can be grouped into methods: analytical models, which directly calculate overall properties from system parameters, like the well known Halpin-Tsai or Mori-Tanaka models of composite materials, and computational methods, the best known of which is the Finite Element (FE) method. Since for our multiscale procedure we chose a particular calculation technique based on this method, we will report more details on this approach in the next Section.

2.3.3.1 Finite Element Methods (FEM)

The FEM goal is to provide a numerical, approximate solution to initial-value and boundary-value problems including time-dependent processes. The method uses a variational technique for solving the differential equations wherein the continuous problem described by the differential equation is cast into the equivalent variation form and the solution is found to be a linear combination of approximation functions.^[26,27]

In this approach the region of interest is covered with a mesh determined by contiguous components called 'elements' and the solution of the differential equation is discretized on the mesh points, called nodes, and interpolated within the elements. A partial (ordinary) differential equation is thereby replaced by a set of coupled ordinary (algebraic) equations and solved numerically at the nodal points. The energy in FE method is taken from the theory of linear elasticity and thus the input parameters are simply the elastic moduli and the density of the material.

In the following we will refer only to the specific form of the method based on the work of Gusev^[28,29] and its implementation in the software Mesoprop and Palmyra by Matsim GmbH.^[30]

This FEM approach consists in a constant-strain-tetrahedra displacement-based technique with an iterative solver. An adaptive (Palmyra)/fixed (Mesoprop) mesh is built using specific criteria to model particle – matrix interface effectively in the RVE. For calculation of thermo-mechanical properties, six different infinitesimally small deformations are applied to the composite mesh and the total strain energy for each of these deformations is minimized using the conjugate gradient method in order to calculate the elastic composite properties. To calculate thermal expansion of the composite a seventh "deformation" (an increase of temperature by 1 Kelvin) is applied in order to obtain the linear thermal expansion coefficients. For other physical properties such as conductivities, dielectric constants, and transport properties a Laplace solver is used, that applies a field in the three main directions to the finite element mesh and minimizes the energy of the composite.

2.3.4 Multiscale molecular modeling

The linking of the atomistic to the macroscopic scale through the mesoscale is probably the greatest challenge to develop reliable method for practical materials' design applications. Only by establishing this connection from microscale to mesoscale it is possible to build first principles method for describing the properties of new materials.

The main problem here is that the method of coarsening the description from atomistic to mesoscale or mesoscale to continuum is not as obvious as it is going from electrons to atoms.^[31]In other words, as already mentioned the coarsening from QM to MD relies on basic principles and can be easily generalized in a method and in a procedure, while the coarsening at higher scales is system specific. For example, the strategy for polymers seems quite different than for metals, which seem different from ceramics or semiconductors.

In DPD chemical interactions are described via a conservative force F_c . This conservative force between two particle i and j , as mentioned previously in this Chapter, is a soft repulsion acting along the line of the particle centers, and is given in absolute value and within the cut-off radius r_c by the Equation 2.5.

The interaction parameter a_{ij} has been linked to the χ -parameter in a Flory-Huggins type model by Groot and Warren^[23], or with the bead size by Maiti and McGrother.^[32]In this work, we use an alternative approach, developed by Scocchi et al.^[33], in which the interaction repulsive DPD parameters are coupled to the energies values resulting from the atomistic molecular dynamics simulations. Accordingly, the derivation of the conservative repulsion from a lower scale (i.e. atomistic) modeling constitutes a bottom-up multiscale approach to the simulation of complex systems. Further, the proposed strategy is not system dependent and can be applied in principle to polymer, polymer solution, systems including solid inclusions.

The proposed multiscale simulation procedure is based on the following steps:

- Fully *atomistic molecular dynamics simulations* are performed to retrieve fundamental structural and energetical information at the molecular level; molecular dynamics energies among each mesoscale specie are calculated. Considering a system made up of single particles i and j ,

the total energy of the system is given, in the hypothesis of neglecting the ternary contribution to interaction, by:

$$\mathbf{E}_{system}^{tot} = n_{ii}E_{ii} + n_{jj}E_{jj} + n_{ij}E_{ij} + n_{ji}E_{ji} \quad (2.9)$$

where

$$n_{ii} = \frac{n_i(n_i - 1)}{2} \quad (2.10)$$

is the number of contacts between the n_i particles of type i , and

$$n_{ij} = \frac{n_i n_j}{2} \quad (2.11)$$

is the number of contacts between n_i particles of type i and n_j particles of type j . Since the mixed energy terms (E_{ij} and E_{ji}) and the number of contacts (n_{ij} and n_{ji}) are the same, the expression for the total system energy becomes

$$\mathbf{E}_{system}^{tot} = n_{ii}E_{ii} + n_{jj}E_{jj} + 2n_{ij}E_{ij} \quad (2.12)$$

The values of the self-interaction energies (E_{ii} and E_{jj}) are easily obtainable dividing the corresponding molecular value by the appropriate number of contacts, while the value of the system total energy is derived straightforwardly from MD.

- Map the atomistic model to the *mesoscale model* reproducing thermodynamic or structural properties, like stiffness (i.e. through Kuhn segment), geometrical quantities, which can be intramolecular (distance between two adjacent super-atoms, angles between three subsequent super-atoms, dihedral angles between four subsequent super-atoms, principal values of radius of gyration tensor, and so forth) or intermolecular (distances between super-atoms belonging to different chains, distances between the centers of mass of different chains or chains fragment, and so on).^[34,35] Which one actually being used depends on the intended purpose of the coarse-grained model. Then, select two reference DPD interactions. Having fixed these two parameters, their values are associated with the corresponding

values of the DPD energies rescaled from MD simulations. All the remaining

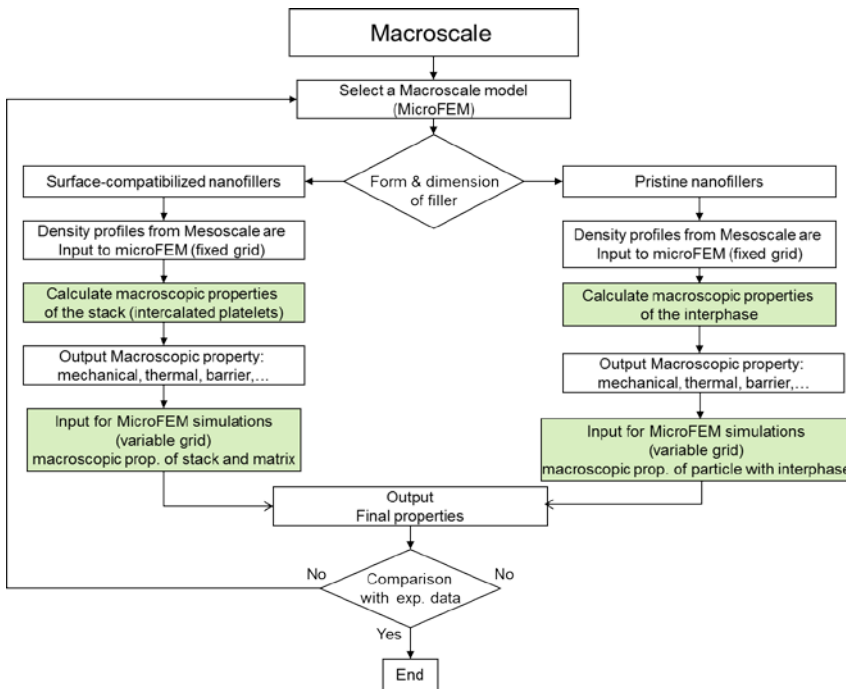
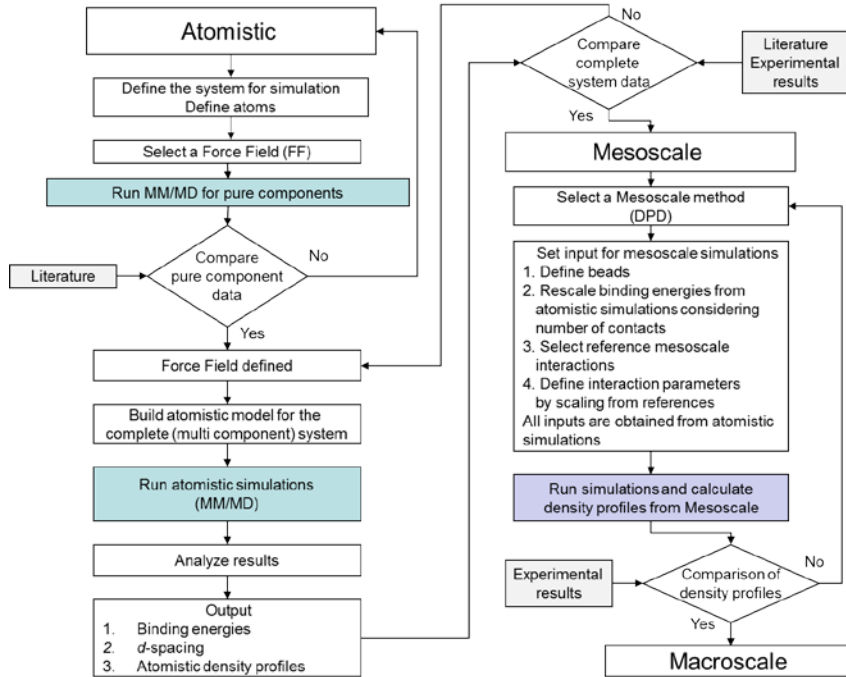


Figure 2.3: General schema of the multiscale simulation protocol adopted in this work.

DPD interaction parameters are derived using this reference relationship.

The primary output of mesoscale modelling are phase morphologies with size up to the micron level. These morphologies are of interest per se, although little prediction of the material properties is available with the mesoscale tools.

An internal consistency is established by comparing the density fields obtained from DPD and MD on the same system using the obtained interaction parameters.

- Export density fields of each mesoscale specie to *FE calculation*, choosing fixed and variable grid according to the complexity and the morphology of the system.

Palmyra and Mesoprop software have been developed to be able to perform FEM analysis also on the density fields generated using the mesoscale techniques. Importing the morphology of the composite as obtained from mesoscale simulation in form of 3-D density distribution of each constituent, FE calculation is performed, so realizing a complete multiscale approach to the prediction of macroscopic properties of nanomaterials.

Figure 2.3 presents our multiscale simulation protocol, which can be used as template for calculation of macroscopic property of different nanoscale systems.

2.4 References

- [1] Maurice Gell; Application opportunities for nanostructured materials and coatings, *Materials Science and Engineering A204* **1995**, 246-251.
- [2] Kalfus J; Jancar J.; *Polymer* **2007**, *48*, 3935.
- [3] Odegard GM; Clancy TC; Gates TS.; *Polymer* **2005**, *46*, 553-62.
- [4] LeBaron PC; Wang Z; Pinnavaia TJ.; *Applied Clay Science* **1999**, *15*, 11-29.
- [5] Andrews R; Weisenberger MC.; *Current Opinion in Solid State and Materials Science* **2004**, *8*, 31-37.
- [6] Douglas JF; Garboczi EJ.; In: Prigogine I, Rice SA, editors. *Advances in chemical physics*, *41*. New York: J.Wiley; **1995**, 85-153.
- [7] Cassagnau P.; *Polymer* **2008**, *49*, 2183.
- [8] Kalfus J.; *Viscoelasticity of glassy polymer nanocomposites*. In: Karger- Kocsis J, Fakirov S, editors. *Nano- and micro-mechanics of polymer blends and composites*. Munich: Hanser; **2009** [Chapter 6].

- [9] Rymond H. Fernando; Nanocomposite and Nanostructured Coatings: Recent advancement, *American Chemical Society* **2009**.
- [10] T.S. Gates; G.M. Odegard; S.J.V. Frankland; T.C. Clancy; *Composites Science and Technology* **65**, **2005**, 2416–2434.
- [11] M. Fermeglia and S. Pricl; *Prog Org Coat* **2006**, **58**:187.
- [12] J. C. Charpentier; *Chem Eng Sci* **2002**, **57**:4667.
- [13] S. C. Glotzer and W. P. Paul, *Annu Rev Mater Res*, **2002**, **32**:401
- [14] Tanguy A; Wittmer JP; Leonforte F; Barrat J-L.; *Physics Review B* **2002**, **66**:174205.
- [15] Maranganti R; Sharma P.; *Journal of the Mechanics and Physics of Solids* **2007**, **55**:1823-52.
- [16] Q. H. Zeng et al.; *Prog Polym Sci*, **2008**, **33** :191.
- [17] D. N. Theodorou and U. W. Suter; **1985**, *Macromolecules*, **18**:1467.
- [18] Kremer K., Muller-Plathe F.; *Mater Res Soc Bull* **2001**(March): 205–14.
- [19] Hinkley J.A., Young J.A.; *Monte Carlo simulation of endlinking oligomers, NASA Langley Research Center, NASA/TM-1998-207649*; **1998**.
- [20] P. J. Hoogerbrugge, and J. M. V. A. Koelman; *Europhys Lett* **1992**, **18**:155.
- [21] J. M. V. A. Koelman and P. J. Hoogerbrugge; *Europhys. Lett*, **1993**, **21**:363.
- [22] P. Espanol and P. B. Warren; *Europhys Lett*, **1995**, **30**:191.
- [23] R. D. Groot and P. B. Warren, *J Chem Phys*, **1997**, **107**:4423.
- [24] Nemat-Nasser S, Hori M. *Micromechanics: overall properties of heterogeneous materials*. 2nd ed. Amsterdam: Elsevier; **1999**.
- [25] Odegard GM, Clancy TC, Gates TS. *Prediction of mechanical properties of polymers with various force fields*. In: 46th AIAA/ASME/ASCE/AHS/ASC structures, structural dynamics, and materials conference, Austin, TX; **2005**.
- [26] Reddy JN. *An introduction to the finite element method*. New York: McGraw-Hill; **1984**.
- [27] Raabe D. *Computational materials science*. Weinheim: Wiley-VCH; **1998**.
- [28] Gusev, A. A. *J Mech Phys Solids* **1997**, **45**, 1449-1459.
- [29] Gusev, A.A. *Macromolecules* **2001**, **34**, 3081-3093.
- [30] MatSim GmbH, Zurich (CH), **2009**. www.matsim.ch.
- [31] Glotzer, S. C.; Paul, S. C. *Annual Review of Materials and Research* **2002**, **32**, 401–436.
- [32] Maiti, A.; McGrother, S. J. *Chem Phys*. **2004**, **120**, 1594-1601.
- [33] Scocchi G., Posocco P., Fermeglia M., and Pricl S., *J. Phys. Chem. B*, Vol. 111, No. 9, **2007**, 2143
- [34] Müller-Plathe, F. *ChemPhysChem* **2002**, **3**, 754-769.
- [35] Scocchi, G.; Posocco, P.; Handgraaf, J. – W.; Fraaije, J. G. E. M.; Fermeglia, M.; Pricl S. *Chem. Eur. J.* **2009**, **15**, 7586-7592.

3

Polymer nanocomposites with different nanoparticles shape

In this chapter we present a multiscale computational approach to characterize a different set of polymer-based nanocomposites (PNCs) obtained with full/partial dispersion of different nanofillers in different polymeric matrices. This approach relies on a step-by-step message-passing technique from atomistic to mesoscale to finite element level, and the calculated results are compared to available experimental evidences. In details, 13 PNC systems have been studied by different molecular modelling methods, such as atomistic Molecular Mechanics and Molecular Dynamics, mesoscale Dissipative Particles Dynamics, and macroscale Finite Element Methods, and their mechanical, thermal and barrier properties have been predicted in agreement with the available experimental data.

This work is published in Toth, R.; Santese, F.; Pereira, S. P.; Nieto, D. R.; Pricl, S.; Fermeglia, M.; Posocco, P., *J. Mater. Chem.*, **2012**,*22*, 5398-5409.

3.1 Introduction

Manufacturers and producers add nanoparticles to polymers in order to improve the stiffness and the toughness of the materials, to amend their barrier properties, to enhance their resistance to fire and ignition or, simply, to reduce costs. These nanofillers come in the form of different shape, such as spheres,¹ tubes,² platelets and discs,³⁻⁵ or fibres.^{6,7} Both scientific and industrial interest in this new class of materials has skyrocketed in the last decades; however, the production of these nanomaterials still includes various accustomed techniques, their preparation is still largely empirical, and a finer degree of control of their ultimate properties cannot be achieved so far. Thus, from an experimental point of view, at least two grand challenges remain: i) the structural characterization and ii) the precise manipulation of the fabrication of these hybrid nanostructure materials. As the final properties of PNCs commonly depend on their structure, a detailed knowledge of the morphology of each PNC system is of paramount importance. To this purpose, the development of theories and the application of computer simulation techniques have opened avenues for the design of these materials, and the a priori prediction/optimization of their structures and properties.¹¹

As documented by Feynman over half century ago¹³: “Atoms on a small scale behave like nothing on a large scale, for they satisfy the laws of quantum mechanics. So, as we go down and fiddle around with the atoms down there, we are working with different laws and we can aspect different things”. In other words, as we already said, as the size scale of matter becomes smaller, down to the nanoscale, the material behaviour can be understood on the basis of intermolecular forces (e.g., van der Waals and hydrogen bonding, electrostatic attractions and repulsions, or steric repulsions). Since all of these forces have a limited distance of influence, ranging from a few angstroms to a few nanometres, proper tools and techniques need to be involved in characterization process in order to provide detailed information about behavior, structural

morphology, and final properties of such nanomaterials. A multiscale molecular modelling approach which bridges the macroscale properties of matter to its atomistic nature via its mesoscopic morphology can be one of those techniques, as its field of operation covers levels ranging from angstroms to micrometres.

Multiscale molecular modelling (MsM) of polymer-based nanocomposite materials poses formidable challenges due to the huge range of length and time scales involved, influencing their structures and physical properties.¹⁴ These challenges can only be met through the development of suitable hierarchical analysis and simulation strategies encompassing many interconnected levels, where each level addresses a phenomenon over a specific window of length and time.

In a previous works of our group²⁶ it has been developed MsM tools that model polymer-based nanocomposite systems from the molecular to the continuum scale. Although each tool performs independent calculations by using only one method at a time, the output from one method can be used directly as input for another, allowing an off-line bridging between the different scales. Further, our recent efforts in the field of molecular modelling also consisted of atomistic calculations concerned with binding energy evaluations for well-characterized systems^{26a-d} using molecular mechanics and molecular dynamics (MM/MD) methods. At the same time, part of our activities was focused on the development and application of mesoscale simulation (MS) tools to polymer blends and nanocomposites morphology investigations, and on the integration of these tools with both atomistic^{26e-h,m,n} and macroscale approaches through finite element method calculations.^{26i,j,l}

In this work we used our wealth of knowledge for a thorough characterization of a set of different PNCs of industrial interest. In detail, we studied the behaviour of different nanofillers (pristine or modified by the addition of, e.g., a compatibilizer) in different polymer matrices (see Table 3.1) by using a multiscale molecular modelling protocol. This, with the final aim of i) predicting some fundamental macroscopic properties of existing nanocomposite materials, ii) compare them with the available experimental data and, iii) ascertain the robustness and validity of this *in silico* approach as a valuable, less-expensive, and time-saving tool for the design of new PNCs with desired performances.

System	Matrix	Filler	Surface modifier
PP/C10A ^a	PP	MMT	(H ₃ C) ₂ N(C ₁₈ H ₃₇)(C ₂ H ₄ Ph)
PP/C15A ^a	PP	MMT	(H ₃ C) ₂ N(C ₁₈ H ₃₇) ₂ [*]
PP/C20A ^a	PP	MMT	(H ₃ C) ₂ N(C ₁₈ H ₃₇) ₂ [*]
PP/C30B ^a	PP	MMT	(H ₃ C)N(C ₁₈ H ₃₇)(C ₂ H ₄ OH) ₂
PP/ODA	PP	MMT	H ₃ N(C ₁₈ H ₃₇)
PA6/C20A ^a	PA6	MMT	(H ₃ C) ₂ N(C ₁₈ H ₃₇) ₂
PA6/C30B ^a	PA6	MMT	(H ₃ C)N(C ₁₈ H ₃₇)(C ₂ H ₄ OH) ₂
PA6/M ₃ C ₁₈	PA6	MMT	(H ₃ C) ₃ N(C ₁₈ H ₃₇)
TPU ^b /C30B	TPU	MMT	(H ₃ C)N(C ₁₈ H ₃₇)(C ₂ H ₄ OH) ₂
PP/HT ^c /FA	PP	HT	C ₁₆ -C ₁₈ fatty acids
PP/SEP ^d	PP	SEP	no surfactant
PP/BOE ^e	PP	BOE	no surfactant
PP/TiO ₂	PP	TiO ₂	no surfactant

Table3.1: Names and compositions of polymer-based nanostructured systems studied in this work. Abbreviations: PP = poly(propylene); PA6 = poly(amide) 6; TPU = thermoplastic poly(urethane); MMT = montmorillonite (platelets); HT = hydrotalcite (platelets); SEP = sepiolite (fibres); BOE = boehmite (spheres); TiO₂ = titania (spheres).^aCloisite C10A, C15A, C20A, and C30B, Southern Clay, USA. ^bElastollan 1185A, BASF, Germany. ^cF100, Akzo Nobel, The Netherlands.; ^dCD1, Tolsa, Spain. ^eDisperal, Sasol, Germany. ^{*}Cloisites C15A and C20A have the same surface modifier but differ in cation exchange capacity (CEC): 125 and 95 mequiv/100 g clay, respectively.

3.2 Simulation procedure

The proposed multiscale simulation procedure is fully described in chapter 2.3.4. Briefly, it is based on the following ansatz: 1) fully atomistic molecular dynamics simulations are performed to retrieve fundamental structural and energetical information at the molecular level; 2) the data gathered at point 1) are mapped into the corresponding structural and energetical information necessary to run coarse-grained simulations at a mesoscopic level; 3) the main output of point 2), i.e., the system mesoscopic morphologies and density distributions finally constitute the input for finite element calculations and macroscopic properties predictions. The core step in the entire computational recipe is undoubtedly constituted by point 2), or the mesoscale level simulations. In mesoscale modelling, the familiar atomistic description of the molecules is coarse-grained, leading to beads of material (representing the collective degree of freedom of many atoms). These beads interact

through pair-potentials which capture the underlying interactions of the constituent atoms. The primary output of mesoscale modelling are phase morphologies with size up to the micron level. These morphologies are of interest per se, although little prediction of the material properties is available with the mesoscale tools. Finite element modelling then comes into play, and the material properties of interest can be calculated accordingly by mapping the material structures formed at the nanometre scale onto the finite element grid and coupling this information with the properties of the pure components that comprise the complex system. Using standard solvers the finite element code can then calculate the properties of the realistic structured material.

3.2.1 Atomistic molecular dynamics (MD) simulations

As mentioned above, atomistic MD simulations constitute the first MsM step, necessary to gather basic structural and energetical information of each PNC system at the molecular level. In particular, the interaction energies among all system components are of paramount importance, as they will, after proper remapping, constitute the major input parameter for performing mesoscale simulations. Hence, the choice of a reliable force field for the description of inter- and intra- molecular interactions in atomistic MD simulations is a critical issue in the entire protocol. Our previous experience,²⁶ coupled with a thorough literature survey,^{15,27} led us to the adoption of the *Compass* force field (FF).^{28,29}

The optimized montmorillonite (MMT) model was taken from our previous work.^{26c,k} Starting from the crystal coordinates of Mg/Al hydrotalcite as determined by Bellotto et al.,³⁰ the 3D model of hydrotalcite (HT) was built and optimized by adapting the procedure adopted for MMT.^{26c,k} The unit cells of sepiolite (SEP), boehmite (BOE), and titanium dioxide (rutile form, TiO₂) were optimized starting from the original structures available in the *Materials Studio* (v.5.5, Accelrys, USA) structure database. To generate a mineral surface apt for simulation, the lattice constant *c* of each mineral cell was extended to 150 Å,^{26c,d} while the lateral dimensions of the cell were increased to the point where the total number of atoms in each model was approximately equal.

The model structures of the MMT and HT surface modifiers (i.e., quaternary ammonium salts and C16-C18 fatty acids, respectively) were

built and subjected to an initial energy minimization process followed by a thorough conformational search. The generation of accurate model amorphous structures for polymers was conducted as follows. First, the constitutive repeating unit (CRU) of each polymer was built and its geometry optimized by energy minimization again using Compass^[28,29]. Hence, each CRU was polymerized to a conventional degree of polymerization (DP) equal to 53 for PP, 25 for Nylon and 12 for TPU. Polymers of similar lengths have been already successfully employed by us in similar studies^[26]. Explicit hydrogens were used in all model systems. The Rotational Isomeric State (RIS) algorithm^[62] as modified by Theodorou and Suter^[63] was used to create the initial polymer conformation at T = 298 K. Each resulting polymer structure was then extensively relaxed to minimize energy and avoid atom overlaps. Subsequently, an NVT MD with temperature increasing to 373 K during 200 ps followed by an NVT MD at 373 K for 500 ps, and a cooling to 298 K over 200 ps was performed on each polymer sample.

After each component was modelled, the overall PNC systems were built, and production molecular dynamics simulations in the canonical (NVT) ensemble were run at T = 298 K. Each MD run consisted of an equilibration phase of 50 ps, followed by a data collection phase extended up to 0.5 ns. The Berendsen thermostat was used to control temperature, while an atom-based cutoff and the Ewald summation technique^[64] were employed to treat dispersion and electrostatic nonbonded interactions, respectively. From the equilibrated part of the MD trajectory of each PNC, the interactions energies among all system components were extracted according to a well-validated procedure.^[26] Since, by definition, the binding energy (E_{bind}) between each generic pair of PNC components A and B is the negative of the corresponding interaction energy, each E_{bind} term can be simply obtained from the corresponding interaction energies as:

$$E_{bind(A/B)} = E_A + E_B - E_{A/B} \quad (3.1)$$

In the case of modified nanoparticles (i.e., MMT and HT), starting from an equilibrated NVT MD snapshot further MD simulations in the isothermal-isobaric (NPT) ensemble were performed to estimate the interlayer (basal) spacing d among the mineral layers.^{26c,k,i} In this case,

during each MD both mineral layers were treated as rigid bodies by fixing all cell dimensions except for c , and all atoms in the interlayer space (including ions and counterions) were allowed to move without any constraint.

3.2.2 Mesoscale (MS) simulations

In order to simulate the morphology of the nanocomposite systems at a mesoscopic level, we used the Dissipative Particle Dynamics (DPD)^[32] simulation tool as implemented in the *Materials Studio* DPD modelling suite. In DPD, a group of atoms is coarse-grained into a bead, thereby substantially reducing the number of particles to be simulated. Further, rather than interact through Lennard-Jones forces, each bead feels a simple soft pair-wise conservative potential which embodies the essential chemistry of the system. This force is of short range, and has a simple analytical form, which results in fast computation per time step and, hence, provides the opportunity to expand the simulation from nanoseconds to real time periods. In the framework of our multiscale approach to PNCs simulation, the interaction parameters needed as input for the mesoscale level DPD calculations have been obtained by a mapping procedure of the binding energy values between different species obtained from simulations at a lower (atomistic) scale.^{26e,i} The complex procedure for mesoscale simulation of our PNC systems consists of several steps: i) choice the bead size, ii) determination of system dimension and bead numbers, and iii) definition of bead-bead interaction parameters. In the case of surface-modified nanocomposites, according to the fundamental DPD concept that different DPD bead types should have equal roughly volumes, and starting with the surface modifier molecules (which consist of a strongly polar head and one/two almost apolar tails) we considered them as made up by two different type of beads H and T , respectively. The corresponding mesoscopic polymer chains were chosen to be constituted of 100 beads of type P . To represent the filler surface, a repulsive wall in the simulation box perpendicular to the z -axis at the origin was employed. Further, we introduced a bead type M with no connectivity and no repulsion towards the wall, in order to fill the space between the two wall surfaces, thus representing a nanofiller layer. A parallel approach and utterly similar concepts were used to build all

remaining PNCs. In the case of unmodified nanoparticle-based PNCs, however, the corresponding mesoscopic cells contained only two type of beads; indeed, beads of the type M were again used to represent the filler (i.e., SEP, BOE, and TiO_2), and beads of the type P were still employed for the polymers.

The next, important issue in DPD simulations is to capture the essential intra-and intermolecular interactions taking place among all molecular actors of the mesoscopic simulations as expressed by the values of the conservative parameter a_{ij} . This quantity accounts for the underlying chemistry of the system considered. In this work, we employed a well-validated strategy that correlates the interaction energies estimated from a lower scale (atomistic MD) simulations to the mesoscale a_{ij} parameter values. Following this computational recipe, the interaction energies among all PNC system components estimated from MD simulations were rescaled onto the corresponding mesoscale segments adapting the procedure described in detail in^[26e,i]The bead-bead interaction parameter for the polymer beads P was set equal to $a_{PP} = 25$, in agreement with the value of DPD density $\rho = 3$ ^[32]. The value of the polymer-filler interaction (i.e., a_{PM}) was chosen to reflect the corresponding atomistic energy value^[26]. Once these two parameters were assigned, all the remaining bead-bead interaction parameters required for the DPD simulations were easily obtained, starting from the relevant atomistic interaction energies values. The entire set of DPD interaction parameters are summarized in Table3.2.

a_{ij}	P	T	H	M	W
PP/C10A					
P	25	31	30.9	32	320
T	31	31.3	35.3	30.4	304
H	30.9	35.3	55.5	5.2	52
M	32	30.4	5.2	15	1
PP/C15A					
P	25	29.5	33.6	34	340
T	29.5	32.2	35	30.7	307
H	33.6	35	62.2	3.5	35
M	34	30.7	3.5	15	1
PP/C20A					
P	25	32.7	32.6	33	330
T	32.7	32.8	36	30.7	307
H	32.6	36	64.2	4	50
M	33	30.7	4	15	1

Polymer nanocomposites with different nanoparticles shape

PP/C30B	P	T	H	M	W
P	25	31.1	31	31	310
T	31.1	30.3	32.9	30.1	301
H	31	32.9	54.1	4.7	47
M	31	30.1	4.7	15	1
PP/ODA	P	T	H	M	W
P	25	31	30.9	32	320
T	31	31.3	35.3	30.4	304
H	30.9	35.3	55.5	5.2	52
M	32	30.4	5.2	15	1
PA6/C20A	P	T	H	M	W
P	25	33.6	34.1	33.1	331
T	33.6	32.11	33.1	30.7	307
H	34.1	33.1	62.4	4.1	41
M	33.1	30.7	4.1	15	1
PA6/C30B	P	T	H	M	W
P	25	32	30	29	290
T	32	30.2	32.7	30.1	301
H	30	32.7	54.3	4.7	47
M	29	30.1	4.7	15	1
PA6/M3C 18	P	T	H	M	W
P	25	31.5	31.1	31.8	318
T	31.5	31.8	30.9	30.6	306
H	31.1	30.9	55.1	5.2	52
M	31.8	30.6	5.2	15	1
TPU/C30B	P	T	H	M	W
P	25	32.5	33.3	31	310
T	32.5	31.1	35.8	30.8	308
H	33.3	35.8	55.2	4	40
M	31	30.8	4	15	1
PP/HT/FA	P	T	H	M	W
P	25	23.3	28.2	24	240
T	23.3	31	24.5	22	220
H	28.2	24.5	57	3	30
M	24	22	3	15	1
PP/SEP	P	T	H	M	W
P	25	-	-	30.4	304
M	30.4	-	-	15	1
PP/BOE	P	T	H	M	W
P	25	-	-	29	290
M	29	-	-	15	1
PP/TiO₂	P	T	H	M	W
P	25	-	-	30.4	304
M	30.4	-	-	15	1

Table3.2: Bead-bead interaction parameter a_{ij} values used in the DPD simulations.

3.2.3 Finite elements (FEM) calculations

The last step of the proposed MsM procedure is constituted by the prediction of a set of important macroscopic properties for the considered polymer nanocomposites as a function of filler loading. To this purpose, finite element (FE) calculations were performed using the software Palmyra (v. 2.5, MatSim, Zürich, CH). FE calculations were applied in order to analyse both platelet stacks and overall nanocomposite properties, using fixed (i.e., *MesoProp* technique)³⁶ and variable grid, respectively. In particular, the Young modulus E , the thermal conductivity κ , and the gas permeability P were the macroscopic properties of election, since not only these quantities are of primary industrial interest but, perhaps more importantly, direct comparison with the corresponding experimental data could be made.

MesoProp technique³⁶ is a method based on finite elements for estimating properties of a complex material starting from the density distribution at mesoscale. The method used the results of a mesoscale simulation under the form of three dimensional density maps and transforms such information into a fixed grid that is used for the integration of the equations for determining macroscopical properties. *MesoProp*³⁶ uses a numerical method to determine the overall properties of composites, with arbitrary morphologies from the properties of the components based on small homogeneous grid elements. The morphology is defined by a number of phases in a periodically continued base cell of cubic or orthorhombic shape, where the phases may consist of any material. Accordingly, the resolution depends solely on the number of grid elements used.

Following a previous work,^{26,k} MMT and HT particles (both single particles and stacks) were modelled as disks with a toroidal rim. Each platelet thickness was defined by the height of the corresponding symmetry axis h and diameter D , thus being characterized by an aspect ratio of $a = D/h$. By setting $D = 120$ nm and $h = 1$ nm for each single particle, the aspect ratio a was equal to 120, a value in agreement with common literature data for layer silicates. Orientation to the platelets was imparted by assigning a value of 0.06 to the eigenvalues 1 and 2. Accordingly a value of 0.88 was automatically assigned to the eigenvalue 3. A highly exfoliated system was defined as having 32 platelets with an

aspect ratio of 120 and 8 stacks of two platelets each. Such a system corresponds to 66.7% exfoliated platelets. The aspect ratio of the stacks ranged from 10 to 13, according to the different basal spacing obtained from the corresponding MD simulations. To simulate a weight fraction Φ_w of 4.6% w/w for all MMT and HT PNCs, a volume fraction Φ_v of 1.5% v/v was used in the case of PP-based PNCs, while a value of $\Phi_v = 1.9\%$ v/v was employed for TPU- and PA6-based systems, respectively. TiO_2 particles were considered as spheres with diameter $\phi_{\text{TiO}_2} = 20$ nm. A volume fraction of 1.07% v/v was used, resulting in a corresponding weight fraction of 4.6% w/w. Boehmite is generally synthesized in crystallites of a platelet or rod shape. The widely employed commercial sample Disperal, however, consists of small crystallites agglomerated. During processing, the agglomerates decrease in size, but still the complete dispersion of the crystallites cannot be achieved.³⁸ Accordingly, this system was defined considering spherical agglomerates of BOE with an average ϕ of 140 nm.³⁹ A volume fraction of 1.43% v/v was used, corresponding to a system with a weight fraction of 4.6% w/w. Finally, the commercial CD1 sepiolite fibers were assumed to have a length $L = 200$ nm and a diameter $\phi_{\text{SEP}} = 10$ nm. A $\Phi_v = 2.1\%$ v/v was considered, corresponding to a system with $\Phi_w = 4.6\%$ w/w.

Interfacial interactions, however, invariably develop in composite systems based on untreated nanofillers, due to the ever-existing van der Waals or electrostatic forces among the particles and the polymer chains. These lead to the formation of a non-negligible interface which, in turn, may considerably influence the macroscopic properties of the relevant PNC. To account for the presence of this interphase layer in the BOE, SEP, and TiO_2 systems, as determined from mesoscale simulations, we resorted to a pseudo “core-shell” model particles at the FEM level. These models consist in spherical (for BOE and TiO_2) and spherocylindrical (for SEP) particles with radius equal to the sum of the pristine nanoparticle radius (constituting the “core” part of the particle) and the interface thickness (making up the “shell”). The overall, main thermophysical properties of these particles were then estimated by mediating each corresponding property of the nanoparticle core (i.e., the pure nanoparticle property) and of the interphase (as obtained by running fixed-grid calculations using the

mesoscopic density distribution as input information) by the corresponding volumetric fractions.

As mentioned previously, the density profiles of each component obtained from mesoscale simulations were used as an input for macroscopic property calculation of the stacks for intercalated systems according to the MsM procedure.

Finally, the bulk properties of each pure component of the diverse PNCs listed in Table3.3constituted the last information necessary to run FEM calculations. All listed data were obtained from literature.⁴⁰ Thermal conductivities of MMT, BOE, SEP and HT were assumed to be the same and equal to the value found for bentonite clay.⁴⁰ⁱ As each nanofiller itself was considered to be impermeable to gases, a very low permeability value (i.e., $P = 0.0001$ barrer) was selected.

	PP	PA6	TPU	MMT
E	1.55 ^{40a}	2.80 ^{40e}	0.02 ^{40g}	178 ^{40h}
ν	0.36 ^{40b}	0.35 ^{40b}	0.45 ^{40b}	0.2 ^{40h}
κ	0.25 ^{40c}	0.28 ^{40f}	0.20 ^{40f}	1.14 ⁴⁰ⁱ
P_{O_2}	9.6 ^{40d}	4.7 ^{40d}	2.1 ^{40d}	10 ⁻⁴
	TiO ₂	SEP	BOE	HT
E	230 ^{40j}	200 ^{40l}	253 ^{40m}	139 ⁴⁰ⁿ
ν	0.25 ^{40j}	0.2 ^{40l}	0.20 ^{40m}	0.30 ⁴⁰ⁿ
κ	11.7 ^{40k}	1.14 ⁴⁰ⁱ	1.14 ⁴⁰ⁱ	1.14 ⁴⁰ⁱ
P_{O_2}	10 ⁻⁴	10 ⁻⁴	10 ⁻⁴	10 ⁻⁴

Table3.3: Macroscopic properties of all PNC pure components: Young Modulus (E , GPa), Poisson ratio (ν), thermal conductivity (κ , W/MK), and gas permeability (P , barrer).

3.3 Results and discussion

3.3.1 Atomistic MD simulations

Interaction energies, basal spacing values d for intercalated PNCs, and density profiles are all major information gathered from atomistic MD simulations and necessary for running next-level simulations, as mentioned above. Table3.4 presents the binding energies between the individual PNC components obtained from the corresponding NVT MD simulations. As somewhat expected, the presence of a modifier on the nanoparticle surface always results in a decrease of the interaction energy between the polymer and nanofillers itself. Indeed, the values $E_{NF/P}$ for the systems devoid of surface modifiers are all above 100 kcal/mol, while

substantially lower values are estimated for those PNC with surface-modified nanoparticles. The binding energy between a polymer/surface-modified nanofillers couple strongly depends upon the volume of organic modifier and the eventual presence of polar groups in its chains (see last column of Table 3.4). A significant exception is constituted by the system PP/ODA, a finding easily rationalized considering the substantially apolar nature and small dimension of ODA which, in turn, exert a low influence on the interactions between the polymer and the filler.

System	$E_{NF/P}^a$	$E_{NF/SM}^b$	$E_{P/SM}^c$	V^d (Å ³)
PP/C10A	75	394	94	483
PP/C15A	25	854	131	735
PP/C20A	47	440	99	735
PP/C30B	85	418	99	470
PP/ODA	120	293	66	345
PA6/C20A	6	475	155	735
PA6/C30B	27	433	156	470
PA6/M ₃ C ₁₈	33	444	163	383
TPU/C30B	95	384	143	470
PP/HT/FA	52	1925	100	314 (C ₁₆) 346 (C ₁₈)
PP/SEP	102	-	-	-
PP/BOE	172	-	-	-
PP/TiO ₂	102	-	-	-

Table3.4: Binding energies between the individual PNC components obtained from atomistic MD simulations. All energies are in kcal/mol. ^a $E_{NF/P}$ = interaction energy between the nanofillers and the polymer. ^b $E_{NF/SM}$ = interaction energy between the nanofillers and the surface modifier. ^c $E_{P/SH}$ = interaction energy between the polymer and the surface modifier. ^d V = molecular volume of the surface modifier.

In the case of PP/MMT-based PNCs, we also found that the mineral CEC exerts a significant effect on the energetics of the corresponding systems. In fact, when the MMT CEC is higher (i.e., system PP/C15A), the binding energy values clearly reveal stronger interactions between polymer and organic modifiers, and MMT and organic modifiers, respectively, while the interactions between the nanofillers and the polymer are hindered due to the crowding of the organics on the MMT surface which leave less free space for polymer/filler favorable contacts.

The nature of the bonds between the surface modifiers and the nanofillers for all PP/MMT, PP/HT, PA6/MMT, and TPU/MMT systems analyzed is ionic. Thus, it is not surprising that for all these PNCs the binding energies $E_{NF/SM}$ are significantly higher than the values of $E_{NF/P}$ and $E_{P/SM}$, respectively. Also, since HT is characterized by a high charge

density in the interlayer space, this last property can be invoked to support the evidence that the binding energy $E_{NF/SM}$ for the system PP/HT is quite higher (1925 kcal/mol) than the corresponding MMT-based systems.

Interestingly, no major differences were observed in those systems containing pristine nanofillers. In all these cases, since the interactions between the nanoparticles and the polymeric chains are mainly determined by van der Waals interactions, the corresponding values of $E_{NF/P}$ are comparable, the one for the PP/BOE system being slightly higher than the other two PNCs (PP/TiO₂ and PP/SEP, respectively).

Table 3.5 lists the predicted interlayer distance values d for all intercalated PNCs considered, as obtained from the corresponding atomistic NPT MD simulations. Intuitively, organic surface modifier characterized by larger molecular dimensions (see last column of Table 3.4) induce a larger inter-gallery distance in the corresponding modified mineral. More importantly, perhaps, is the good agreement of the *in silico* values with the corresponding experimental results^{26e,37,42,43} (shown in parenthesis in Table 3.5 for comparison), since this quantity constitutes a direct input parameter for the successive, i.e., mesoscopic, set of simulations.

Stack	Interlayer spacing [nm]
PP/C10A	3.73 (3.71 ⁴²)
PP/C15A	4.90
PP/C20A	4.10
PP/C30B	3.68
PP/ODA	3.73
PA6/C20A	4.22 (4.22 ⁴³)
PA6/M ₃ C ₁₈	4.00
PA6/C30B	4.22
TPU/C30B	4.22
PP/HT/FA	4.10 (4.1 ³⁷)

Table 3.5: Basal spacing of stacks in intercalated PNCs calculated by MD simulations. Available experimental data are reported in parenthesis, for comparison.

Figure 3.1 presents a selected example of the atomistic models employed in the MD simulations for the calculation of the interaction energies (NVT MD) and, specifically for layered nanoinclusions, the estimation of the interlayer d spacing (NPT MD), respectively.

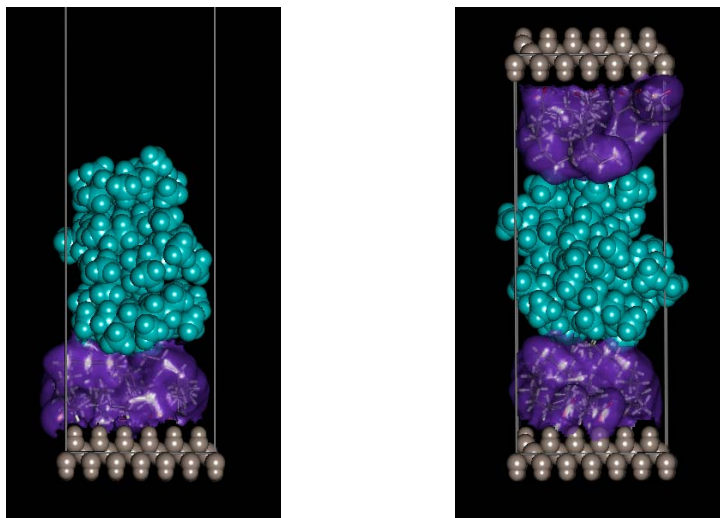


Figure 3.1: (Left) Equilibrated molecular model system used in atomistic NVT MD simulations for binding energy calculations in PNC systems with surface modifier. (Right) Equilibrated molecular model systems used in atomistic NPT MD simulations for interlayer spacing determination in PNC with surface modifier. The system PP/HT/FA is shown as an example.

3.3.2 Mesoscale simulations

The application of computer-based simulation techniques at the mesoscale level aims both at filling the gap between detailed atomistic and coarse continuum level, and to avoid their shortcomings. In the specific field of PNCs, mesoscale simulations are employed to study the structural evolution, the microphase structure and the phase separation of these systems. Figure 3.2 shows an illustration of the equilibrated model obtained from DPD simulations of the PP/HT/FA PNC system as an example.

In order to validate our mesoscale calculations, performed using parameters generated via a mapping procedure based on the information stemming from the lower scale MD simulations, we chose to compare the number density profiles calculated from MD trajectories with those obtained by analysis of the DPD runs. The density profiles capture the arrangement of the total organic matter (polymer and surface modifiers) in the mineral galleries, through a plane normal to the galleries (z -direction). In the case of polymer-intercalated clay stacks, there is general agreement amongst researchers about the arrangement of organic species within the gallery systems:^{26e,i,44,45} intercalated species usually exhibit high

and low density layers alternating from the clay surface, rapidly reaching bulk polymer density in the centre of the gallery. This arrangement indeed confirmed by the distribution of the organic density obtained from both MD and DPD simulations, as shown in Figure 3.3 again for the system PP/HT/FA as an example.

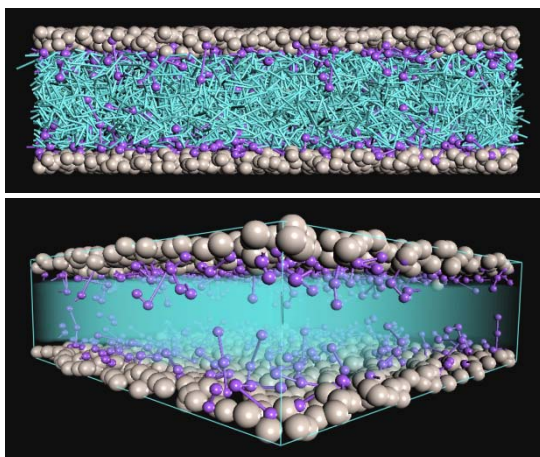


Figure 3.2: Front (top) and side (bottom) view of the equilibrated mesoscopic model obtained from DPD simulations of the PP/HT/FA PNC system. Colour code: gray, HT; purple, FA; light blue, PP. In the bottom panel, the PP beads are replaced by a light blue field, to highlight the distribution of the FA molecules within the HT layers.

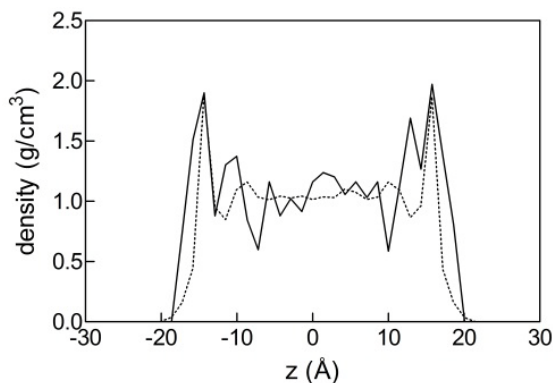


Figure 3.3: Comparison between interlayer densities of organic species (surface modifiers and polymer) in the gallery space of the PP/HT/FA PCN as obtained from MD (continuous line) and DPD (dotted line) simulations, respectively.

As we can see from Figure 3.3, the system organizes into layers inside the clay gallery. This layering effect is well-known for confined liquids,⁴⁶⁻⁴⁸ and arises mainly from solvation forces. The rough and

irregular shape of the profile obtained for confined macromolecules – if compared, for instance, to the smooth and regular one exhibited by low molecular weight confined fluids – is due to the additional constraints to which the polymer atoms are subjected, as being connected along chains that run across many adjacent organic layers. However, Figure 3.3 clearly shows that the peaks have different heights and widths, depending on their location within the gallery. The highest density peaks are those closer to the clay layers; their height is indicative of the strong affinity between the adsorbed organic/polymer chains and the clay surface. The adjacent peaks are lower, as a consequence of the adsorption of the first layer that partially shields the attractive potential of the clay surface. In the centre of the gallery, practically only polymer chains are found. Since the overall arrangement and, in particular, the presence of high density peaks next to the clay surface is in agreement with the current literature on similar systems,⁵¹⁻⁵³ these evidences constitute a further confirmation that the adopted atomistic/mesoscopic mapping procedure correctly reproduces density distributions of polymer chains and surface modifier molecules within inorganic layers.

For the PNCs with pristine nanofillers, the arrangement of the DPD polymer beads near the different inorganic surfaces reflects the trends determined by atomistic MD calculations as well. Interestingly, the partial adsorption of the polymer molecules onto the filler surface results in the development of a polymer layer, as evidenced by the corresponding density maps (see Figure 3.4) which, in principle, might have properties different from those of the bulk polymer matrix.⁵⁴ The thickness of this interphase, as expected, depends on the type and strength of the interaction between the nanoparticle surface and the polymer, being usually generated by secondary van der Waals or electrostatic forces. Thus, values from 1 nm to several microns have been reported in literature for the most diverse PNCs.⁵⁵ As can be inferred from Figure 3.4, the interphase thickness obtained from our mesoscopic simulations for the BOE, SEP and TiO₂ PNCs are similar, the one for the TiO₂-based system (~1.7 nm) being slightly larger than that estimated for the BOE and SEP PNCs (1.1-1.2 nm). Interestingly, these values are in line with experimental evidences available on similar systems.⁵⁵

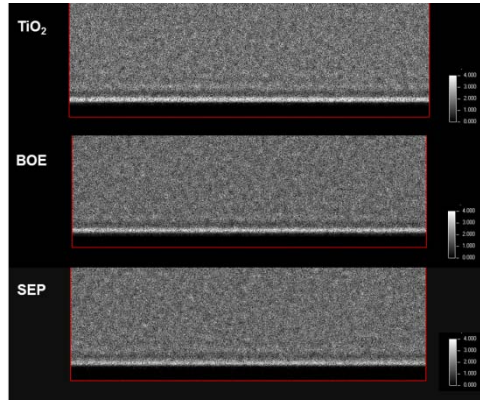


Figure 3.4: Mesoscopic density maps obtained for TiO₂- (top), BOE- (centre), and SEP- (bottom) based systems.

3.3.3 MicroFEM calculations of stack properties for intercalated PNCs

To calculate a set of macroscopic properties of a PNC stack (see Figure 3.5), we resorted to finite-element fixed-grid (*MesoProp*) calculations. In particular, the Young modulus E , the thermal conductivity κ , and the gas permeability P were the macroscopic properties of election, since not only these quantities are of primary industrial interest but, perhaps more importantly, direct comparison with the corresponding experimental data could be made.³⁷

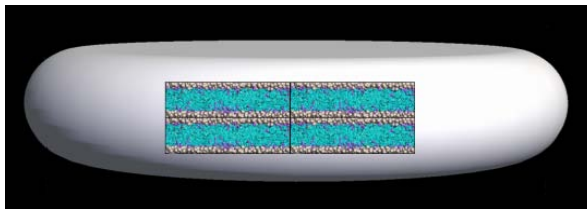


Figure 3.5: Example of the intercalated stack model for the PP/HT/FA PNC system used in the FE.

Aside pure component properties, the mesoscopic density matrices obtained from DPD simulations for each PNC systems were used as input information as well. We must note here that, for permeability, a value of $P = 0.0001$ barrer was chosen for the MMT and HT platelets, as the stacks were reasonably assumed to be non-permeable to gases. All relevant results are presented in Table 3.6. Each property is expressed as an average value in the x and y direction with respect to the orientation of the platelets.

Stack	E (GPa)	κ (W/mK)	P_{O_2} (barrer)
PP/C10A	70.06 (0.19)	1.070 (0.076)	1.69×10^{-3} (1.1×10^{-4})
PP/C15A	75.44 (0.43)	1.092 (0.079)	1.93×10^{-3} (1.3×10^{-4})
PP/C20A	72.36 (0.70)	1.078 (0.078)	1.84×10^{-3} (1.1×10^{-4})
PP/C30B	70.34 (0.57)	1.070 (0.075)	1.74×10^{-3} (1.2×10^{-4})
PP/ODA	88.22 (0.46)	1.186 (0.090)	1.32×10^{-3} (1.1×10^{-4})
PA6/C20A	110.30 (0.07)	1.298 (0.080)	9.00×10^{-4} (0.95×10^{-4})
PA6/M3C18	110.39 (0.15)	1.295 (0.083)	8.20×10^{-4} (0.89×10^{-4})
PA6/C30B	110.30 (0.12)	1.295 (0.082)	8.60×10^{-4} (0.91×10^{-4})
TPU/C30B	100.05 (0.11)	1.088 (0.112)	4.02×10^{-4} (0.44×10^{-4})
PP/HT/FA	104.22 (0.15)	1.283 (0.080)	5.64×10^{-3} (1.3×10^{-4})

Table 3.6: Properties of intercalated PNC stacks estimated using fixed-grid calculations performed exploiting the density profiles of each system derived from mesoscale simulations. Symbols: E = young modulus; κ = thermal conductivity; P = permeability. Standard deviations are given in parenthesis.

3.3.4 MicroFEM calculations of the properties for unmodified PNCs with interfaces

As briefly mentioned above, non-treated filler have high energy surfaces. Accordingly, during the most common PNC preparation process (i.e., melt mixing), intermolecular forces lead to a partial adsorption of polymer chains onto the filler surfaces. The thickness and the properties of the resulting interphase have not be indisputably unveiled so far. Indeed, if the formation of a softer interphase was claimed by some authors, other, more frequent reports reveal the presence of a stiffer interface which, in turn, contributes to the overall increase of the PNC stiffness. In order to account for the existence of this interphase in our surface-pristine PNCs, we performed *MesoProp* fixed-grid calculations using the corresponding DPD density maps (see Figure 3.4) as input.

PNC	E (GPa)	κ (W/mK)	$P(O_2)$ (barrer)
PP/BOE	241.89 (0.22)	1.130 (0.08)	0.97 (0.11)
PP/SEP	152.07 (0.30)	1.070 (0.06)	4.93 (0.61)
PP/TiO ₂	172.75 (0.26)	8.94 (0.45)	4.73 (0.62)

Table 3.7: Properties of nanoparticles with interfaces estimated using the interface thickness and properties inferred from mesoscale and fixed-grid simulations. Standard deviations are given in parenthesis.

With these information at hand, we then estimated the properties of the corresponding pseudo “core-shell” model nanoparticles as listed in Table 3.7. Finally, these values were employed in the last FEM calculations, yielding the overall macroscopic properties of each corresponding PNCs.

3.3.5 Macroscopic properties of all nanocomposite systems

The prediction of the macroscopic properties of the entire polymer nanocomposite systems was achieved with FEM calculations using a variable-grid approach.⁵⁶ In the case of surface-modified nanoparticle PNCs, a cell was created and objects as single platelets and stacks were added until the required volume fraction was achieved. Figure 3.6 shows the FEM model adopted for the PP/HT/FA PNC system as an example.

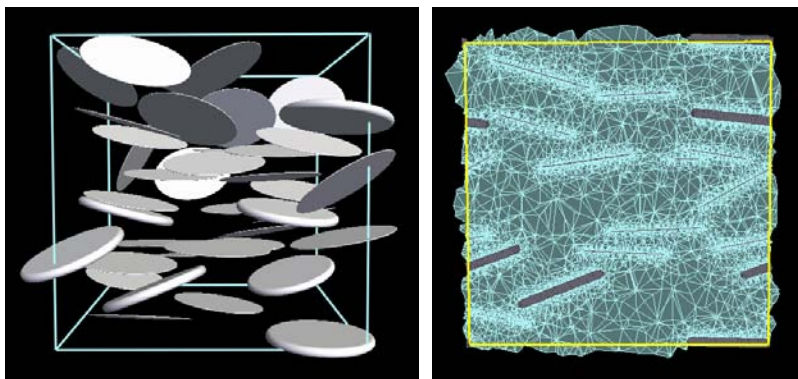


Figure 3.6: Global model configuration (left) and relative meshed volume (right) used in the FE calculations for the PP/HT/FA PNC system.

The properties of pure components (polymers, MMT and HT) were inserted in materials database together with the properties of the stacks as obtained using the fixed-grid (*MesoProp*) calculations described above. On the other hand, in the case of system without organic modifiers the cell was generated using the pseudo “core-shell” filler models, and assigning to these the corresponding values listed in Table 3.7.

The set of properties and their values calculated for all the different nanocomposite systems are shown in Figure 3.7 in terms of enhancement factor $E_f = P_c/P_m$, i.e., the ratio between a given property value for the nanocomposite (P_c) and the corresponding value for the pristine polymer matrix (P_m).

In the *intercalated system* *In the s*, in general, an increase of 60% on mechanical properties is observed when a 4.6 % w/w of MMT is added to PP or PA6 matrices. Since the elastic modulus of neat PP is lower than that of PA6, FEM calculations show that the elastic modulus of the PA6/MMT nanocomposites is also slightly higher than that of PP/MMT systems (see Figure 3.7), which can be further attributed to the higher mechanical properties of PA6/MMT stacks with respect to the corresponding PP/MMT counterparts (Table 3.6).

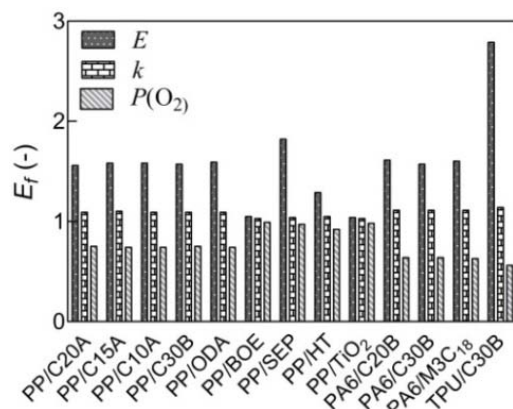


Figure 3.7: Predicted enhancement factor $E_f = P_d/P_m$ of the macroscopic properties of different nanocomposite systems.

According to fixed-grid calculations, substituting MMT with HT in PP-based PNCs results in PP/HT stacks with higher elastic modulus than the PP/MMT stacks (see Table 3.6). This enhancement can be due to the high affinity between PP chains and HT platelets, as testified by the low value of the DPD interaction parameter $a_{M/P}$ for the PP/HT system (see Table 3.2). Notwithstanding, a moderate increase in mechanical property is predicted in the case of PP/HT PNC, as a result of the low elastic modulus of pristine hydrotalcite. It is well known that intercalation of HT is linked with difficulties due to the high charge interlayer density, which leads to strong electrostatic interactions between the sheets. Experimental trials to produce this kind of nanocomposite showed that HT particles of 10 μm tend to de-agglomerated into smaller, disk-like aggregates with diameters ranging from 200 to 500 nm and consisting of 3-4 layers of layered double hydroxides.⁵⁷ De-agglomeration, poor dispersion and different aspect ratios are usually invoked to explain the high range of variability in the enhancement factor of the Young modulus of these

nanocomposites (e.g. from 1.07 for 10 % w/w of HT³⁷ to 1.28 for 3 % w/w of HT⁵⁸). Taking all these aspects into account, our estimated value of $E_f = 1.29$ for the 4.6 %w/w proves the predictive character of our multiscale approach.

Neat TPU has an elastic modulus significantly lower than the other polymers considered (Table 3.3). Interestingly, reinforcing this low-modulus matrix with nanofillers has the highest beneficial effect which, in turn, reflects in the highest increase in the Young modulus of the relevant TPU/MMT PNC with respect to all other intercalated PNCs (Figure 3.7).

Concerning the other macroscopic properties considered, an increase of about 10% in thermal conductivity and a decrease of ~ 25% (PP) and 36% (PA6) in permeability is predicted by our MsM approach. The gas permeability in a PNC depends mainly on orientation, aspect ratio and volume fraction of the filler in the matrix. A rationale for the fact that the PA6/MMT nanocomposite systems offer a higher barrier to the diffusion of gas with respect to the PP-based nanocomposites can be based on the fact that i) both the volume fraction of MMT in the PA6 matrix is higher, and ii) the density of PA6 polymer is higher than that of PP. Other differences might be noted depending on the surface modifiers used which, in turn, stem from the diverse stack properties and dissimilar aspect ratios.

A series of different measurements and morphological characterizations were reported by Fornes et al.⁵⁹ in a complex study where sodium montmorillonite was modified with a series of organic amine salts. Interestingly, a good agreement is found between the experimental data of Fornes and the present results in a direct comparison for PA6-based nanocomposite systems with $\Phi_w = 4.5$ % w/w. Indeed, the experimental enhancement factors E_f of 1.57, 1.62 and 1.69 for the Young modulus E of the systems PA6/C20A, PA6/C30B, and PA6/M₃C₁₈ quite nicely correspond to our calculated values of 1.61, 1.57, and 1.60, respectively. In the case of the PA6/C30B and PA6/M₃C₁₈ systems, the calculated E_f values are somewhat lower than those obtained by simulation. These small discrepancies can be justified by considering the very high level of exfoliation and dispersion of the MMT platelets in the experimental samples.⁵⁹ However, it is clear that the system with M₃C₁₈ as clay modifier yields a greater enhancement in Young modulus than the

C30B composite according to both simulated and experimental results. On the other hand, our simulations show that PA6/C20A offers the highest increase of the Young modulus, which is not supported by experiments due to the partial intercalation that takes place by using this kind of surfactant.⁵⁹

In the case of TPU-based nanocomposites, a good agreement of the predicted Young modulus is found with the experimental results,⁴⁶ since an E_f value of 2.96 for TPU loaded with 5 % w/w of C30B well compares with the *in silico* value of 2.76. For the same system, also the experimental $E_f = 1.18$ for thermal conductivity^{40f} quite nicely matches the predicted value of 1.14. It is important to note here that a substantially higher increase in the conductivity value along the x and y directions with respect to the z direction was observed, which was due to the alignment of the platelets on those directions.

Lastly, given the small difference between calculated and experimental κ values (approximately 3.5%), we can state that the predictive power of the multiscale procedure is validated also for this property.

Now we will discuss the results concerning the *PNC systems without surface modifiers*. Recently, in the framework of the jointed European integrated project (IP) *Multihybrids*, Tabuani et al.³⁷ experimentally evaluated the mechanical properties of the same series of pristine PNCs based on SEP, BOE, MMT, and HT. In the case of PP/SEP nanocomposite, our calculated enhancement factor for the Young modulus $E_f = 1.47$ is in an excellent agreement with the experimental values of 1.46³⁷ and 1.50.⁶⁰ Figure 3.8 illustrates the FE model used for the prediction of the mechanical properties of the PP/SEP PNC.

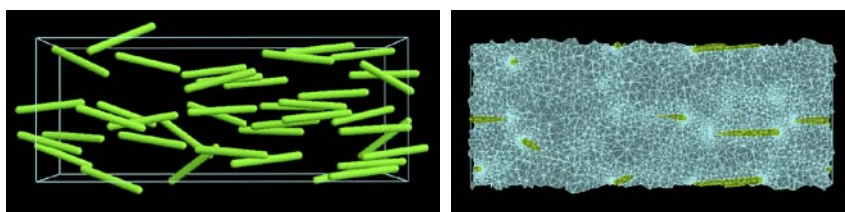


Figure 3.8: (Left) FEM PP/SEP model and (right) the corresponding FEM mesh.

Due to the incomplete dispersion/agglomeration of the filler which takes place during processing, the PP/BOE system was defined

considering agglomerates of spherical shape. Figure 3.9 shows a comparison between the TEM images of the PP/BOE PNC agglomerates⁶¹ and our simulated system. The corresponding, predicted Young modulus ($E_f = 1.05$) is slightly lower than the available experimental values ($E_f = 1.11^{49}$ and 1.18^{37}), due to a) the definition of the filler as a spherical object in a trial approximation of the real shape of the aggregates (see Figure 3.9), and b) the somewhat different volume fraction employed in the real PNC (5 vs. 4.6 %w/w). Notwithstanding the degree of approximation, our computational predictions and the relevant experimental results can be considered in very good agreement.

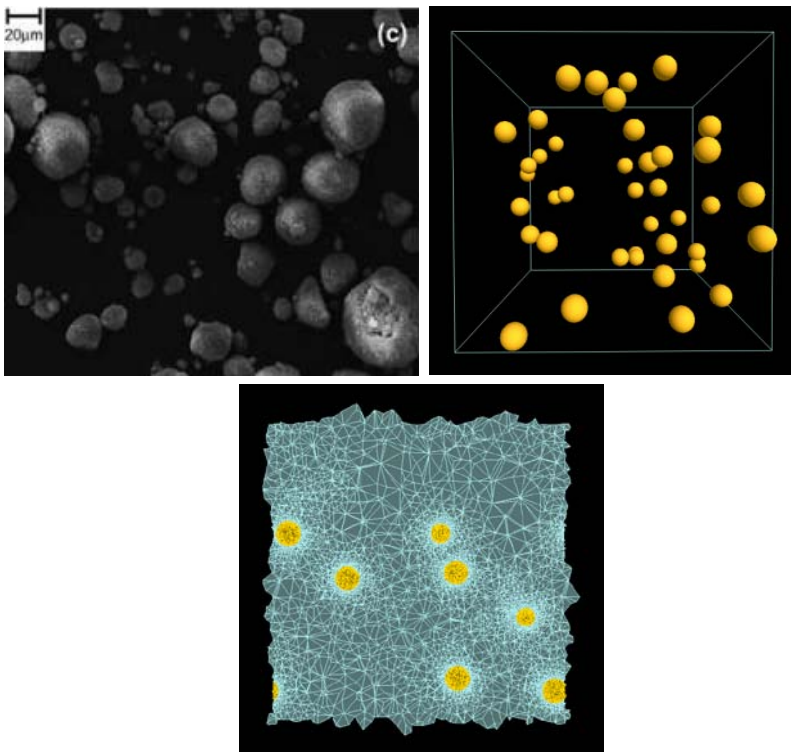


Figure 3.9: (Top, left) SEM image of PP/BOE PNC agglomerates studied in this work. (Top, right) FEM PP/BOE model and (bottom) the corresponding FEM mesh.

The lowest increase in elastic modulus E for the entire set of PNCs considered in this work was observed for those systems loaded with spherical fillers, as exemplified by the modest 4% increase of the Young modulus E for the PP/TiO₂ system (see Figure 3.7 and Figure 3.10).

An experimental characterization of the dimensions of titania nanoparticles performed again in the Multihybrids IP framework³⁹ revealed quite a broad distribution 10-100 nm, with a marked peak centered around 20 nm. Although no experimental E_f values are available for this system, the MsM procedure predicts a reliable increase of $\sim 3.4\%$ in the thermal conductivity κ and a concomitant decrease of 2% in the oxygen permeability P_{O_2} . Based on the results obtained for the PP/TiO₂ and PP/BOE PNCs we can conclude that, as intuitively expected by virtue of the low aspect ratio, spherical nanofillers exert a limited influence on the thermophysical properties of the corresponding polymer nanocomposites.

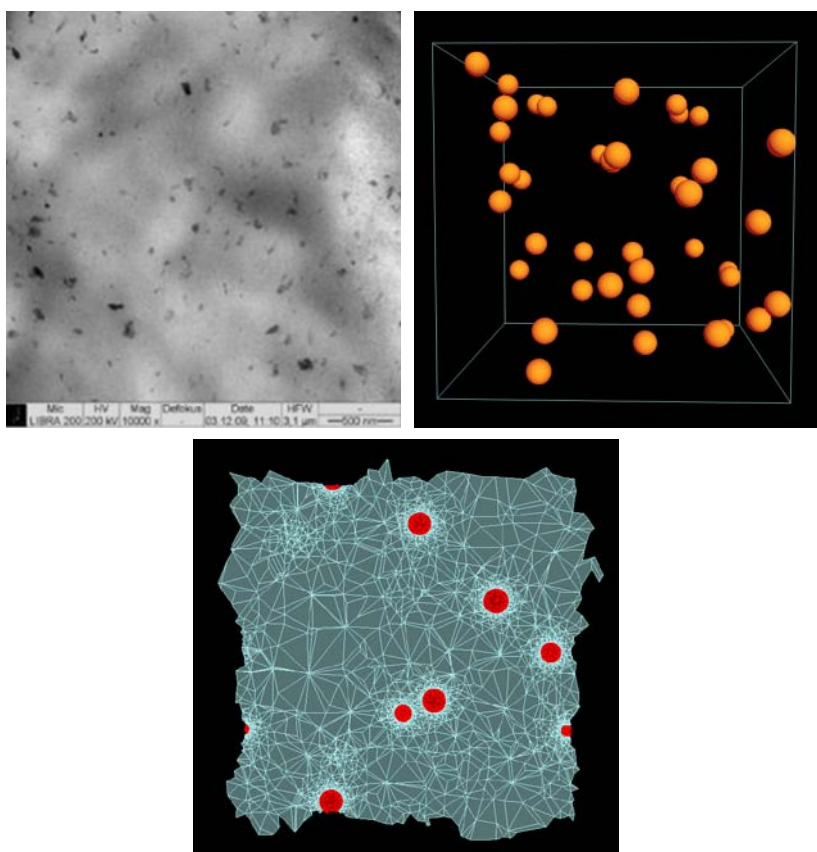


Figure 3.10: (Top, left) TEM image of the PP/TiO₂ PNC studied in this work.³⁹(Top, right) FEM PP/TiO₂ model and (bottom) then corresponding FEM model mesh.

From a general perspective, our calculations confirm and substantiate the general assumption that aspect ratio and/or shape of the

filler significantly influence the mechanical properties of polymer-based nanocomposites. In our comprehensive study, fibres (i.e., sepiolite) and platelets in the system TPU/C30B significantly offer the highest E_f in terms of mechanical behaviour (see Figure 3.7). In the first case, this increment is clearly induced by the shape and aspect ratio of the filler, while in the second case it is the very low Young modulus of the pristine TPU polymer that plays a fundamental role in the enhancement of the value of E (Table 3.3). On the other hand, the lowest increase (<10%) in the mechanical properties is observed for those systems with spherical fillers (PP/BOE and PP/TiO₂), while platelet-based PNCs show a considerable increase up to 60% for MMT-based PNCs. Also, the presence and the different nature of small organics as surface modifiers may ultimately contribute – although to a more limited extent – to the overall improvement of the PNC mechanical performances.

Concerning thermal conductivity, even if no substantial differences were predicted among the different PNCs considered, some global conclusions can be presented. Even if the thermal conductivity of TiO₂ is quite high with respect to the other fillers (see Table 3.3), no significant increase in the κ value for the corresponding PP/TiO₂ PNC is observed. A similar value of E_f for thermal conductivity is predicted for another system with spherical filler (PP/BOE), even if the thermal conductivity of Boehmite is significantly lower than that of TiO₂ (Table 3.3). Coupled together, these evidences allow to conclude that spherical fillers exert an overall negligible effect also on the thermal conductivity of the respective PNCs.

Lastly, as oxygen permeability is concerned, a pronounced decrease in P is observed in the case of intercalated nanocomposites (see Figure 3.7) with respect to all other PNCs (SEP, BOE, and TiO₂), which are more or less dispersed. A decrease of 25% and 36% in permeability is predicted for intercalated systems with PP and PA6, respectively, while the effect is confined to less than 3% in all other cases. Based on these results it is evident that permeability strongly depends on the internal morphology and alignment of the fillers in the polymer matrix, more ordered (intercalated) arrangement of filler featuring the higher decrease in permeability.

3.4 Conclusion

In this work we presented the development and application of a multiscale molecular modelling (MsM) procedure for the prediction of the macroscopic properties of polymer-based nanocomposites. The results obtained from this *in silico* approach are very encouraging, as the predicted values for a selected set of thermophysical quantities are in outstanding agreement with the corresponding experimental counterparts. Moreover, the analysis of the entire panel of results allowed us to draw some general conclusions regarding the role of the single components with respect to the overall performance of the different PNCs. First, the presence of modifiers on the surface of the nanoparticles has a significant effect on the interactions between the polymeric matrix and the nanofiller which may reflect in a great influence on the intercalation/exfoliation process during the preparation of PNC. This, in turn, affects the overall structure of the nanocomposite and, ultimately, its macroscopic property. However, once a specific morphology is generated at the nanoscale level, the chemical/physical characteristics of the different surface modifiers are smeared out, and their individual contribution to the PNC macroscopic properties become negligible. On the other hand, the size and shape of the filler as well as the properties of the pure nanocomposite components are all aspects that have a big impact on overall material properties.

Spherical fillers affect mechanical and other thermal properties to a minimum extent, independently on nanoparticle dimensions. On the opposite, the impact of high aspect ratio nanoparticles such as fibres is significantly higher, and it can be further influenced by the change in fibre length or orientation within the polymeric matrix. In the case of clay, the aspect ratio of the platelets plays a key role in determining the ultimate properties of the relevant nanocomposites, as also confirmed by our previous studies in which we examined the effect of the different degree of exfoliation in polymer/MMT nanocomposites.²⁶ Quite intuitively, the best exfoliated structures result in the most enhanced mechanical properties.

Within the framework of our current material science and engineering research, we can conclude that a complete integration of all

available simulation scales (i.e., from atomistic molecular simulations via mesoscopic dynamics to finite element calculations) in a hierarchical procedure such as that proposed in the present work can be a very useful tool for the morphological investigation of polymer-based nanocomposite and the a priori prediction of the ultimate properties of these fascinating materials. Undoubtedly, further work is necessary to achieve a more refined multiscale integration for these materials; however, the simple approach proposed in this paper represents, at least in our opinion, the best compromise between the overall computational time required to carry out the entire multiscale molecular modeling procedure and the great quality of the results predicted.

3.5 References

- [1] A. Convertino, G. Leo, M. Striccoli, G. Di Marco and M.L. Curri. *Polymer***2008**, 49, 5526-5532.
- [2] J.N. Coleman, U. Khan, J.W. Blau and Y.K. Gunko. *Carbon***2006**, 44, 1624-1652.
- [3] S.S. Ray and M. Okamoto, *Progr. Polym. Sci.***2003**, 28, 1539-1641.
- [4] K. Chrissopoulou and S.H. Anastasiadis, SH. *Eur. Polym. J.* **2011**, 47, 600-613.
- [5] S.P Lonkar, S. Therias, N. Caperaa, F. Leroux and J.L. Gardette. *Eur. Polym. J.* **2010**,46, 1456-1464.
- [6] S. Xie, S. Zhang, F. Wang, M. Yang, R. Seguela and J.M. Lefebvre. *Compos. Sci. Technol.* **2007**, 67, 2334-2341.
- [7] Y. Xu and Y.V.Hoa. *Compos. Sci. Technol.* **2008**, 68, 854-861.
- [8] S. Pavlidou and C.D. Papaspyrides. CD. *Progr. Polym. Sci.***2008**, 33, 1119-1198.
- [9] G. Choudalakis and A.D. Gotsis. AD. *Eur. Polym. J.* **2009**, 45, 967-984.
- [10] C.J. Wu, A.K. Gaharwar, P.J. Schexnailder and G. Schmidt. *Materials***2010**, 3, 2986-3005.
- [11] Q. H. Zeng, A.B. Yu and G.Q. Lu. *Progr Polym. Sci.* **2008**, 33, 191-269.
- [12] M Alexandre and P. Dubois. *Mater. Sci. Eng.* **2000**, 28, 1-63.
- [13] R.P. Feynman. *Caltech Eng. Sci.* 1960, 23, 22-36.
- [14] S.A. Baeurle. *J. Math. Chem.* **2009**, 46, 363-426.
- [15] B. Minisini and F. Tsohnang. *Composites Part A***2005**, 36, 539-544.
- [16] G. Allegra, G. Raos and M. Vacatello. *Progr. Polym. Sci.* **2008**, 33, 683-731.
- [17] H.W. Wang, H.W. Zhou, R.D. Peng and L. Mishnaevsky Jr. *Compos. Sci. Technol.* **2011**,71, 980-988.
- [18] N. Sheng, M.C. Boyce, D.M. Parks, G.C. Rutledge, J.L. Abes and R.E. Cohen. *Polymer***2004**, 45, 487-506.
- [19] P.D. Spanos and A. Kotsos. *Prob. Eng. Mech.* **2008**, 23, 456-470.
- [20] C. Li and T.W. Chou. *Compos. Sci. Technol.* **2006**, 66, 2409-2414.
- [21] D. Luo, W.X. Wang and Y. Takao. Y. *Compos. Sci. Technol.***2007**, 67, 2947-2958.
- [22] A. Jafari, A.A. Khatibi and M.M. Mashhadi. *Composites Part B***2011**,42, 553-561.
- [23] Z. Boming, Y. Zhong, W. Yufeng and S. Hongwei, *Mater. Des.* **2010**, 31, 2312-2318.
- [24] V. Sansalone, P. Trovalusci and F. Cleri. *Acta Mater.* **2006**, 54, 3485-3492.
- [25] K. Matous, H.M. Inglis, X. Gu, D. Rypl, T.L. Jackson and P.H. Geubelle. *Compos. Sci. Technol.* **2007**, 67, 1694-1708.
- [26] a) M. Fermeglia, M. Ferrone and S. Pricl. *Fluid Phase Equilib.* **2003**, 212, 315-329; b) M. Fermeglia, M. Ferrone and S. Pricl. *Mol. Simul.* **2004**,30, 289-300; c) R. Toth, A. Coslanich,

- M. Ferrone, M. Fermeglia, S. Pricl, S. Miertus and E. Chiellini. *Polymer* **2004**, *45*, 8075-8083; d) R. Toth, M. Ferrone, S. Miertus, E. Chiellini, M. Fermeglia and S. Pricl. *Biomacromolecules* **2006**, *7*, 1714-1719; e) G. Scocchi, P. Posocco, M. Fermeglia and S. Pricl. *J. Phys. Chem. B* **2007**, *111*, 2143-2151; f) P. Cosoli, G. Scocchi, S. Pricl and M. Fermeglia. *Microporous Mesoporous Mater.* **2008**, *107*, 169-79; g) M. Fermeglia and S. Pricl. *Progr. Org. Coat.* **2007**, *5*, 187-99; h) M. Fermeglia, P. Cosoli, M. Ferrone, S. Piccarolo, G. Mensitieri and S. Pricl. *Polymer* **2006**, *47*, 5979-89; i) R. Toth, D.J. Voorn, J.W. Handgraaf, J.G.E.M. Fraaije, M. Fermeglia, S. Pricl and P. Posocco. *Macromolecules* **2009**, *42*, 8260-70; j) G. Scocchi, P. Posocco, A. Danani, S. Pricl and M. Fermeglia. *Fluid Phase Equilib.* **2007**, *261*, 366-374; k) S.P. Pereira, G. Scocchi, R. Toth, P. Posocco, D.R. Nieto, S. Pricl and M. Fermeglia. *J. Multiscale Modelling*, **2011**, *3*:151-176; l) G. Scocchi, P. Posocco, J.W. Handgraaf, J.G.E.M. Fraaije, M. Fermeglia and S. Pricl. *Chem. Eur. J.* **2009**, *15*, 7586-92; m) P. Posocco, Z. Posel, M. Fermeglia, M. Lisal and S. Pricl. *S. J. Mater. Chem.* **2010**, *20*, 10511-20; n) M. Maly, P. Posocco, S. Pricl and M. Fermeglia. *Ind. Eng. Chem. Res.* **2008**, *47*, 5023-38.
- [27] a) H. Zhang, X. Lu, Y. Leng, L. Fang, S. Qu, B. Feng and J.W.J. Wang. *Acta Biomater.* **2009**, *5*, 1169-81; b) S. Sutton and G. Sposito. *Geochim. Cosmochim. Acta* **2006**, *70*, 3566-81; c) Y. Han and J. Elliott. *Comput. Mater. Sci.* **2007**, *39*, 315-23.
- [28] H. Sun. *J. Phys. Chem. B* **1998**, *102*, 7338-64.
- [29] D. Rigby. *Fluid Phase Equilib.* **2004**, *217*, 77-87.
- [30] M. Bellotto, B. Rebours, O. Clause and J. Lynch. *J. Phys. Chem.* **1996**, *100*, 8527-8534.
- [31] M. Fermeglia and S. Pricl. *AIChE J.* **1999**, *45*, 2619-2627.
- [32] a) P.J. Hoogerbrugge and J.M.V.A. Koelman. *Europhys. Lett.* **1992**, *18*, 155-160; b) a) J.M.V.A. Koelman and P.J. Hoogerbrugge. *Europhys. Lett.* **1993**, *21*, 363-368; b) R.D. Groot and P.B. Warren. *J. Chem. Phys.* **1997**, *107*, 4423-4435.
- [33] a) P. Posocco, M. Fermeglia and S. Pricl. *S. J. Mater. Chem.* **2010**, *20*, 7742-7753; b) P. Posocco, S. Pricl, S.P. Jones, A. Barnard and D.K. Smith. *Chem. Sci.* **2010**, *1*, 393-404; c) S.P. Jones, N.P. Gabrielson, C.H. Wong, H.F. Chow, D.W. Pack, P. Posocco, M. Fermeglia, S. Pricl and D.K. Smith. *Mol. Pharmaceut.* **2011**, *8*, 416-429; d) A. Barnard, P. Posocco, S. Pricl, M. Calderon, R. Haag, M.E. Hwang, V.W.T. Shum, D.W. Pack and D.K. Smith. *J. Am. Chem. Soc.* **2011**, Just Accepted Manuscript, DOI: 10.1021/ja2070736.
- [34] M.A. Osman, V. Mittal and H.R. Lusti. *Macromol. Rapid. Commun.* **2004**, *25*, 1145-1149.
- [35] M. Heggli, T. Etter, P. Wyss, P.J. Uggowitzer and A.A. Gusev. *Adv. Eng. Mater.* **2005**, *7*, 225-229.
- [36] A.A. Gusev. *J. Mech. Phys. Solids* **1997**, *45*, 1449-1459.
- [37] D. Tabuani, S. Ceccia and G. Camino. *Macromol. Symp.* **2011**, *301*, 114-127.
- [38] R.C. Streller, R. Thomann, O. Torno and R. Mulhaupt. *Macromol. Mater. Eng.* **2008**, *293*, 218-227.
- [39] 6th EC FP IP *MultiHybrids* (026685-2IP) project consortium, private communication (**2011**).
- [40] PP data sheet: <https://polymers.lyondellbasell.com/>; b) R.J. Crawford. *Plastics Engineering* (3rd Edition). Elsevier; **1998**; c) Plastic materials data base (IDES): <http://www.ides.com>; d) L.K. Massey. *Permeability Properties of Plastics and Elastomers - A Guide to Packaging and Barrier Materials* (2nd Edition). William Andrew Publishing/Plastics Design Library, **2003**; e) PA6 data sheet: <http://www.rhodia.com>; f) W.K. Ho, J.H. and O.A. Ezekoye. *J. Nanomater.* **2010**, 1-11; g) TPU data sheet: <http://www.basf.com>; h) T.D. Fornes and D.R., *Polymer* **2003**, *44*, 4993-5013; i) R. Almanza and M.C. Lozano. *Sol. Energy* **1990**, *45*, 241-245; j) J. Winkler. *Titanium Dioxide*. European Coating Literature, **2003**; k) <http://www.ceram.com>; l) E. Bilotti, R. Zhang, H. Deng, F. Quero, H.R. Fischer and T. Peijs. *Compos. Sci. Technol.* **2009**, *69*, 2587-2595; m) M.R. Gallas and G.J. Piermarini. *J. Am. Ceram. Soc.* **1994**, *77*, 2917-2920; n) M.A. Thyveetil, P.V. Coveney, J.L. Suter JL and H.C. Greenwell. *Chem. Mater.* **2007**, *19*, 5510-5523.

- [41] a) H. Heinz, H. Koerner, K.L. Anderson, R.A. Vaia and B.L. Farmer. *Chem. Mater.* **2005**, 17, 5658-5669; b) Y.-T. Fu and H. Heinz. *Chem. Mater.* **2010**, 22, 1595-1605.
- [42] D. Marchant and K. Jayaraman. *Ind. Eng. Chem. Res.* **2002**, 41, 6402-6408.
- [43] T.D. Fornes, D.L. Hunter and D.R. Paul. *Macromolecules* **2004**, 37, 1793-1798.
- [44] F. Gardebien, A. Gaudel-Siri, J.L. Brédas and R. Lazzaroni. *J. Phys. Chem. B* **2004**, 108, 10678-10686.
- [45] H. Heinz, R.A. Vaia, R. Krishnamoorti and B.L. Farmer. *Chem. Mater.* **2007**, 19, 59-68.
- [46] J.N. Israelachvili. *Intermolecular and Surface Forces*. San Diego, CA, Academic Press, **1992**.
- [47] S. Cui, P.T. Cummings and H.D. Cochran. *J. Chem. Phys.* **2001**, 114, 7189-7194.
- [48] M. Fermeglia and S. Pricl. *Rheol. Acta* **2001**, 40, 104-110.
- [49] I. Bitsanis and G. Hadziioannou, *J. Chem. Phys.* **1990**, 92, 3827-3847.
- [50] S.J. Klatte and T.L. Beck. *J. Phys. Chem.* **1995**, 99, 16024-16032.
- [51] a) E. Manias, H. Chen, R. Krishnamoorti, J. Genzer, E.J. Kramer and E.P. Giannelis. *Macromolecules* **2000**, 33, 7955-7966; b) V. Kупpa, S. Menakanit, R. Krishnamoorti and E. Manias. *J. Polym. Sci. Part B: Polym. Phys.* **2003**, 41, 3285-3298.
- [52] a) A. Gaudel-Siri, P. Brocorens, D. Siri, F. Gardebien, J.L. Bredas and R. Lazzaroni. *Langmuir* **2003**, 19, 8287-8291; b) F. Gardebien, J.L. Bredas and R. Lazzaroni, *J. Phys. Chem. B* **2005**, 109, 12287-12296.
- [53] D.R. Paul, Q.H. Zeng, A.B. Yu and G.Q. Lu. *J. Colloid Interf. Sci.* **2005**, 292, 462-468.
- [54] F. R. Jones, in F. R. Jones (Ed.). *Interfacial Phenomena in Composite Materials*, Butterworths, London, **1989**, p. 25.
- [55] J. Móczó and B. Pukánszky. *J. Ind. Eng. Chem.* **2008**, 14, 535-563.
- [56] A.A. Gusev. *Macromolecules* **2001**, 34, 3081-3093.
- [57] S. Bocchini, Morlat-Therias, J.L. Gardette and G. Camino. *Eur. Polym. J.* **2008**, 44, 3473-3481.
- [58] C. Marega, V. Causin, A. Marigo, G. Ferrara and H. Tonnaer. *J. Nanosci. Nanotechnol.* **2009**, 9, 2704-2714.
- [59] T.D. Fornes, P.J. Yoon, D.L. Hunter, H. Keskkula and D.R. Paul. *Polymer* **2002**, 43, 5915-5933.
- [60] E. Bilotti, H.R. Fischer and T. Peijs. *J. Appl. Polym. Sci.* **2008**, 107, 1116-1123.
- [61] S. Bocchini, S. Morlat-Therias, J.L. Gardette and G. Camino. *Polym. Degrad. Stabil.* **2007**, 92, 1847-1856.
- [62] Flory P.J. *Principles of Polymer Chemistry*. Ithaca, NY: Cornell University Press; 1974.
- [63] Theodorou DN, Suter UW. *Macromolecules* **1986**; 19: 139-54.
- [64] Ewald P.P. *Ann Phys* **1921**; 64: 253-87.

4

In silico estimation of polymer surface wettability

In this work, molecular dynamics (MD) simulations were performed to investigate the wetting behavior of solid surfaces in the presence of model solvents. Four kinds of solid substrates were considered with different degree of hydrophobicity/hydrophilicity: polypropylene (PP), polystyrene (PS), polyamide 6 (PA6), and cellulose. Water, oil and a mixture of water and surfactants were selected as reference fluids to investigate the wetting ability. Additionally, we refined our methodology to discriminate the properties of seven different aromatic fluoropolymers in contact with a water nanodroplet. Two computational recipes were developed and compared to quickly and accurately provide direct microscopic evidence for the effect of fluids on the wettability of a solid substrate. Contact angle, interfacial tension, work

of adhesion, binding energies were predicted and provided a comprehensive understanding of the involved interfacial phenomena.

Part of this work is published in Nieto, D.R.; Santese, F.; Toth, R.; Posocco, P.; Pricl, S.; Fermeglia, M. *ACS Appl. Mater. Interfaces* **2012**, *4*, 2855–2859 and F. Santese; D. R. Nieto; P. Posocco; R. Toth; S. Pricl; M. Fermeglia; *ACS Appl. Mater. Interfaces*, **2013** submitted.

4.1 Introduction

Nowadays there is an increasing demand for surfaces with new functional properties in almost all industrial branches. During the next few years, research input will be required for the development of coatings exhibiting an easy-to-clean or self-cleaning ability, switchability so that they can act as sensors/actuators, and defined tribological/mechanical properties and long-term stability. To achieve such behavior, the development of new advanced functional coatings that exhibit the proper chemistry and surface structure is necessary. Accordingly, preparation and characterization of materials with tailored hydrophilic or hydrophobic surfaces have been extensively investigated. In addition to the scientific curiosity to understand the critical chemical and physical factors and/or parameters leading to the formation of such surfaces, potential technological applications of these materials in various fields, such as biomaterials, micro-electronics, micro-fluidics, coatings, textiles, and so forth, have been the major driving forces behind these studies. Moreover, the knowledge and control of interfacial wettability of hydrophilic (e.g., water) and hydrophobic (oil) substances on polymeric surfaces is one of the main issues in current practical surface science and interfacial engineering. For example, highly hydrophobic surfaces are designed to avoid the adhesion of snow and raindrops on car windshields, or in order to form self-cleaning surfaces on kitchen furniture tops. On the contrary, hydrophilic surfaces are sought in biomedical applications, e.g., tissue engineering and drug delivery. Therefore, investigating the structure and behavior of common fluids, such as water, oil, and mixtures of surfactant/water, with polymer of different chemical nature is of great, practical importance.

It is well-documented that wetting behavior of a substrate is mainly controlled by its chemical nature and surface topography or roughness.

Therefore, manipulating the hydrophobicity/hydrophilicity of a given surface necessarily requires understanding of the microscale principles that, in turn, control the macroscale surface wetting behavior.

A realistic modeling of the solid-liquid interface is complicated by the fact that solid surfaces are typically far from ideal and are characterized by a large set of (often unknown) parameters. This is in the first place the surface shape, which often contains variable amounts of roughness on different length scales. In the case of a hydrophilic surface, the density of polar surface groups, their spatial distribution on the surface, and the orientation of dipoles are largely unknown, and the same is true for charged surface groups. Likewise, the strength of the non-electrostatic interactions between surface groups and water molecules, which are typically subsumed under the heading of dispersion or van der Waals interactions, is not known. It is the sum of these effects that determines the effective interfacial tension (and thus the contact angle), and understandably, it is difficult to disentangle the influence of the separate parameters on the resulting macroscopic interfacial behavior.

In the past few years, substantial progress has been achieved in understanding wetting phenomena from both the experimental and theoretical fronts.¹ In particular, as an alternative to experimental campaigns, molecular simulations have been widely applied to the study of solid surfaces/liquid interactions, with especial focus on water spreading on both hydrophobic and hydrophilic material surfaces. Nonetheless, most of the work published so far was based on ideal surfaces, i.e., surfaces with regular, periodic conformation such as crystals and crystalline polymers. On the contrary, computational studies dealing with liquid spreading onto amorphous polymer surfaces are quite scarce, and this paucity may be ascribed to the fact that constructing a well-defined model for amorphous polymer surfaces and simulating systems having interfacial regions with unconfined roughness requires notable computational time and resources.

The wetting of a surface is essentially determined by molecular interactions between the surface and the liquid, contact angle (θ), surface tension (γ), and work of adhesion (W_{adh}) being the most popular physical parameters used to quantify these phenomena. Thus, approaches based on atomistic molecular simulations should, in principle, yield vital

insights on these interactions and constitute ideal tools to estimate the related technological parameter values. Nonetheless, accurate information for these solid/liquid interactions at an atomistic level have been scarcely achieved so far due to many factors, including the lack of well-defined amorphous polymer surface models. Also, the spread of experimental values for both θ and W_{adh} in the current literature highlights the technical difficulties inherent in this research field. For instance, deducing an actual value of the W_{adh} in a given system is a daunting task as most of the mechanical adhesion tests employed provide largely overestimated values of W_{adh} due to the large energy dissipation originating in the test samples during measurements.^[2]

In the present work we performed atomistic molecular dynamics (MD) calculation of different fluids (water, oil, and a mixture of surfactants/water) with various chemically heterogeneous ideal surfaces (PS, PP, PA6, and cellulose) varying their properties in a systematic way (i.e., from hydrophobic to hydrophilic) and explicitly calculated contact angles, interfacial tension, work of adhesion, as well as interaction energies. The correlation between the microscopic and macroscopic properties allowed us to characterize the interfacial/wetting behavior in a stringent fashion.

Amorphous polypropylene (PP) and polystyrene (PS) are two of the most generally produced plastics, with a variety of applications in different fields such as coatings, packaging, insulation, drug delivery, and biosensors.^[3] Polyamide 6 (PA6) is one of the most widely used engineering thermoplastics, with in-between hydrophilicity. Amorphous model cellulose films have been recently developed, and their molecular structure has been studied in many experimental efforts.^[4] Water and oil were chosen as representative wetting fluids; furthermore, we decided to investigate the effect of additives (i.e. soaps) in water droplets on surfaces, due to their industrial relevance.

Two computational recipes were developed and compared to quickly and accurately provide direct microscopic evidence for the effect of solvent on the wettability of a solid substrate. Contact angle (θ), interfacial tension(γ), work of adhesion (W_{adh}), binding energies were predicted and provided a comprehensive understanding of the involved interfacial phenomena. The results stemming from the accuracy of the

force field employed and the computational recipes adopted in the two simulation pathways not only yielded values comparable to each other but, perhaps more importantly, in excellent agreement with the corresponding experimental data.

Furthermore, the procedure thus validated has been applied to the study of different aromatic fluoropolymers. Fluoropolymers have many interesting properties not found in their hydrocarbon analogues^[5] thanks to their chemical structure. The strong C-F bonds and weak polarity of fluoropolymers imparts a unique set of properties to these types of polymers, such as low surface tension, low coefficient of friction, piezoelectric and pyroelectric properties high thermal stability, low permeability, and strong chemical resistance.^[6]

These properties make these polymers ideal candidates for many high performance applications such as aerospace, aeronautics, optics, microelectronics, paints and coatings, engineering and biomaterials, etc. Most commercially available fluoroalkenes are PTFE (Polytetrafluoroethylene), FEP (Fluorinated ethylene propylene), PFA (Perfluoroalkoxyethylene), ETFE (Ethylenetetra-fluoroethylene), ECTFE (Ethylenchlorotri-fluoroethylene), PCTFE (Polychlorotri-fluoroethylene), PVDF (Polyvinylidene fluoride). The properties vary between different fluoropolymers. The fully fluorinated polymers, such as PTFE, FEP and PFA, have better thermal (higher use temperature) and chemical resistance properties than their partially fluorinated counterparts like PVDF and ECTFE. However, partially fluorinated resins possess better mechanical properties, such as tensile strength, toughness, abrasion and cut-through resistance at ambient temperatures. The wettability of a surface can be strongly influenced by the distribution of acidic groups and/or surface dipoles across the interface. In contrast to fully fluorinated polymers, partially fluorinated resins possess enhanced acidity and increased polarity due to the differing electronegativities of carbon, fluorine, and hydrogen. The existence of polarity in the partially fluorinated polymers strongly influences the interfacial properties, which leads to an enhanced wettability toward contacting liquids as a function of the degree of polarity.^[7] The acidity of the monomers can be enhanced by the presence of the aromatic groups, so, among fluoropolymers, fluorinated aromatic polymers represent a new and interesting

generation^[8] and in the present work we want to provide a complete characterization of some of this type of polymers. The introduction of fluorine substituent or groups containing fluorine atoms into the aromatic polymers is regarded as effective ways to obtain increased solubility, glass transition temperature (T_g) and thermal stability, and also to achieve a decreased moisture absorption and dielectric constant^[9]. Currently, the most widespread applications of the aromatic fluoropolymers are films and coatings microelectronics devices^[10]. It is important to combine or enhance these basic characteristics of fluoropolymers in order to develop new materials. Thus, an atomistic understanding of the atomistic origin of many of these surface properties is essential for understanding adhesion and wettability^[11]. MD simulation has already been successfully used to study some aliphatic fluoropolymers^[12-13]. However, to our knowledge, aromatic fluoropolymers have not been investigated by computer simulation so far. In this work we present a study of the wettability phenomena of seven different aromatic fluoropolymers predicting some important surface properties, as surface tension, work of adhesion and contact angle and comparing these values with the corresponding experimental data.

4.2 Computational details and simulation methodology

In this work we employed two different computational protocols based on molecular dynamics (MD) simulations to quantify θ and W_{adh} and described the interfacial phenomena (see Figure 4.1).

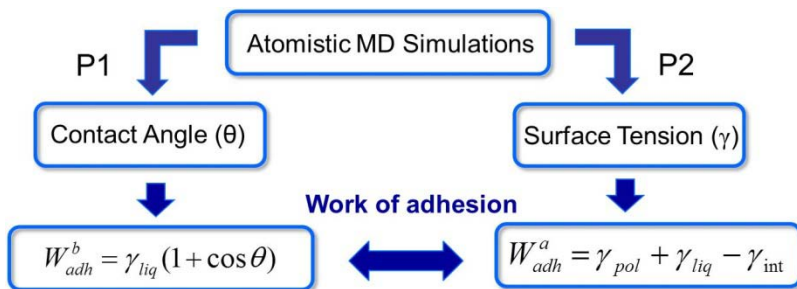


Figure 4.1: Diagram of the two simulation pathways adopted in this work.

4.2.1 Pathway 1 (P1)

Water droplet model.

In order to achieve a good compromise between accuracy and computational time, 500 SPC/E water molecules^[14] were employed in the construction of the water droplet model.^[15-18] The starting water cluster corresponded to a cubic liquid water configuration with side length 2.46 nm and density $d = 1 \text{ g/cm}^3$, energetically optimized using the *Compass* force field^[19] (FF) via a combination of conjugate gradient/Newton-Raphson iterations using a convergence criterion of $10^{-3} \text{ kcal}/(\text{mol } \text{Å})$. The particle mesh Ewald (PME) method^[18] and an atom-based cutoff of 12.5 Å were used to treat electrostatic and van der Waals interactions, respectively. Subsequently, the cubic lattice was removed and 100 ps of molecular dynamics (MD) simulations in the canonical (NVT) ensemble were performed at $T = 298 \text{ K}$ using the *Forcite* engine of *Materials Studio* (v. 5.1, Accelrys Inc., San Diego, CA, USA). These and all subsequent MD simulations were run in parallel using 8 CPUs of our *MOSE20* cluster. Temperature control was carried out with the Berendsen thermostat^[20], while the equations of motion were integrated using the Verlet algorithm with a step size of 2 fs. Long-range non-bonded interactions were again treated using the PME technique and the atom-based cutoff. After a few picoseconds of MD simulation, the water cluster evolved into a smooth drop-like profile, showing that the initial cubic configuration does not influence the final liquid droplet shape.

Oil and surfactant/water droplet model.

Octadecanoic (stearic) acid was selected as a prototypical representative of a fatty acid. The corresponding molecular model was energy minimized using the *Compass* FF and the same criteria adopted for the water droplet. 30 molecules of stearic acid were then placed in a cubic cell of side length 2.47 nm and $d = 0.94 \text{ g/cm}^3$. After system minimization, 500 ps of NVT MD simulations at $T = 298 \text{ K}$ were applied to relax the system. Also in this case, a spherical oil droplet was formed as the final MD configuration. The same modeling procedure described above was applied to model a droplet of surfactant/water mixture. Sodium laurate was selected as representative of a common surfactant. 500 molecules of water were placed together with 12 laurate ions and 12 Na⁺ in a cubic cell

of side length 2.56 nm and $d = 1.01 \text{ g/cm}^3$ and subjected to the MD simulation protocol until the droplet formation.

Polymer surface.

The generation of an accurate model of amorphous PP, PS, PA6, and cellulose was conducted as follows. First, three small PP chains each with a degree of polymerization (DP) equal to 5 were generated and subjected to energy relaxation using *Compass*. It is important to note here that, although such small oligomers would hardly capture a genuine response of the behavior of a real polymer chain, it has been shown that all typical features of the fast segmental dynamics of interfacial polymer chains can be explored indeed using much shorter molecules.^[21] The conformational search was carried out using our combined molecular mechanics/molecular dynamics simulated annealing (MDSA) protocol,^[22] according to which the relaxed structure were subjected to five repeated temperature cycles (from 298 to 600K and back) using NVT MD conditions. At the end of each annealing cycle, each structure was again energy minimized to converge below $10^{-4} \text{ kcal}/(\text{mol } \text{Å})$, and only those structures corresponding to the minimum energy were used for further modeling. Then, a cubic box was generated starting with the optimized *a*-PP chains using the Theodorou and Suter version of the Rotational Isomeric State (RIS) method^[23] at $T = 298\text{K}$ and $d = 0.93 \text{ g/cm}^3$ (and 0.96 g/cm^3 for PS, 1.08 g/cm^3 for PA6, and 1.5 g/cm^3 for cellulose). The energy of the system was relaxed using *Compass* and, in order to generate a surface with appropriate dimensions for the droplet spreading simulations, the periodic cell was replicated in x and y directions to yield a final cell with dimensions $7.31 \text{ nm} \times 7.31 \times 1.04 \text{ nm}$ ($6.82\text{nm} \times 6.82 \text{ nm} \times 1.71 \text{ nm}$ for PS, $6.95\text{nm} \times 6.95 \text{ nm} \times 1.74 \text{ nm}$ for PA6, and $6.96 \text{ nm} \times 6.96 \text{ nm} \times 1.39 \text{ nm}$ for cellulose).

Water, oil, and surfactant/water droplets on the polymer surface.

After each component was modeled, the overall systems (i.e., water/oil/surfactant&water droplet and PP surface) were built. As a first step, to avoid interference of neighboring images in the vertical direction, the z -dimension of the polymer cell was extended to 15 nm. Then, the equilibrated water/oil/surfactant&water droplet was placed centered on top of the polymer surface at an initial distance of about 3 Å , and the

resulting system was relaxed and subsequently subjected to 500 ps of NVT MD simulations at $T = 298$ K. In this case, the Ewald method was applied for treating all nonbonded interactions. The Berendsen thermostat with a decay constant of 0.1 ps was adopted for temperature control and 1 fs was chosen as the Verlet integration time step. The first 50 ps of the MD simulation were required to reach the equilibrium state (monitored by the large and rapid decay of the average internal energy of the system followed by a steady plateau). Following that, the remaining 450 ps of equilibrated MD trajectory were used for data harvesting and analysis.

Contact angle calculation.

The contact angle θ for water, oil, surfactant/water onto the amorphous surfaces was determined following the method proposed by Fan and Cagin.^[24] Briefly, according to this methodology, the θ value of a spherical liquid droplet on a given (e.g., polymeric) surface can be obtained as:

$$\cos\theta = 1 - h/R \quad (4.1)$$

where h is the height of the liquid droplet relative to the polymer surface and R is the radius of the spherical droplet. R in turn can be calculated as:

$$R = h/2 + S/(2\pi h) \quad (4.2)$$

in which S is the droplet interfacial area given by:

$$S = \pi R_s^2 \quad (4.3)$$

R_s being the radius of the droplet interfacial area S .

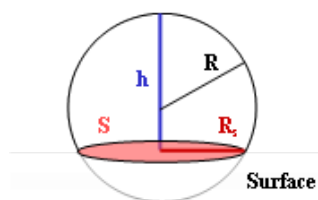


Figura4.2: Geometrical parameters for the calculation of the contact angle θ

For asymmetrical droplets spreading on a surface, however, the RDD cannot provide the value of the contact angle directly. Therefore, equation (4.1) was employed to obtain the information of the droplet shape.^[24] In the case of a nanoscopic irregular and asymmetric droplet,

radial density distribution in the z-direction (i.e., perpendicular to the surface) achieved by time-average statistics on the equilibrated MD conformation was employed to estimate the height h of the droplet, and the droplet shape was obtained applying the eq. (4.4):

$$r = \sqrt{\frac{1}{\rho\pi} \frac{\Delta m}{\Delta z}} \quad (4.4)$$

In eq. (4.1), r is the radius of the contact surface formed, ρ is the fluid density, and $\Delta m/\Delta z$ is the weight distribution along the z-axis. Once h and r values are known, the corresponding value of θ can be finally estimated.

We note that, occasionally, spontaneous evaporation from the droplet into the vacuum took place. However, very few water molecules escaped from the drop and the evaporated molecules eventually returned to the main body of the droplet, so that, ultimately, the volume of the cluster remained effectively constant.

Binding energies

From the equilibrated part of the MD trajectory of each droplet/polymer system, the interactions energies and, hence, the binding energies (E_{bind}) among all system components were extracted according to the procedure described in detail in [25], [26]. By definition, the binding energy E_{bind} is the negative of the interaction energy. As an example, the binary binding energy term $E_{bind}(PP/H_2O)$ is simply obtained from the following equation:

$$E_{bind}(PP/H_2O) = E_{PP} + E_{H_2O} - E_{PP/H_2O} \quad (4.5)$$

where E_{PP} , E_{H_2O} , and E_{PP/H_2O} are the potential energies for PP, water, and PP/H₂O systems. After deleting the water molecules, leaving the PP chains alone, we calculated the energy of the PP molecule, E_{PP} ; similarly, we deleted the PP molecules from the PP/H₂O system, and calculated the energy term E_{H_2O} . $E_{bind}(PP/oil)$ and $E_{bind}(PP/surfactant_H_2O)$ can be calculated in an utterly analogous fashion from the corresponding energy components:

$$E_{\text{bind}}(\text{PP/oil}) = E_{\text{PP}} + E_{\text{oil}} - E_{\text{PP/oil}} \quad (4.6)$$

$$E_{\text{bind}}(\text{PP/surfactant_H}_2\text{O}) = E_{\text{PP}} + E_{\text{surfactant_H}_2\text{O}} - E_{\text{PP/surfactant_H}_2\text{O}} \quad (4.7)$$

4.2.2 Pathway 2 (P2)

The second simulation protocol (P2 in Figure 4.1) was based on the adoption of the so-called Dupré equation^[27] to estimate the work of adhesion between a liquid droplet and a polymeric surface as follows:

$$W_{\text{adh}} = \gamma_p + \gamma - \gamma_i \quad (4.8)$$

where γ_p and γ are the surface tension of the polymeric surface and of the spreading liquid, respectively, while γ_i is the interface tension between the two condensed phases. To this purpose, an alternative MD protocols based on bulk (3D) and thin-film (2D) cell simulations was developed according to which the values of γ_p , γ_s and γ_i could be evaluated using Equations (4.9) and (4.10):

$$\gamma = \frac{\langle U_{2D} \rangle - \langle U_{3D} \rangle}{A} \quad (4.9)$$

$$\gamma_i = \frac{\langle U_i \rangle - (\langle U_l \rangle + \langle U_p \rangle)}{A_i} \quad (4.10)$$

In Equation (4.9), $\langle U_{2D} \rangle$ and $\langle U_{3D} \rangle$ represent the MD-averaged potential energies of the thin film and bulk phase simulations, respectively, and A is the corresponding value of the solvent-accessible surface area. In Equation (4.10), $\langle U_i \rangle$ is the average potential energy of the interface, $\langle U_l \rangle$ and $\langle U_p \rangle$ are the energy of the liquid and polymer thin film models, and A_i is the solvent-accessible interface area.

Water, oil, and surfactant/water droplet model.

To obtain equilibrated bulk models of the fluid, the approach originally proposed by Rigby^[16] was adopted. Thus, a cubic periodic cell with 500 water molecule at density d close to 1 g/cm³ at $T = 298$ K were placed in a cubic cell of side length 2.28 nm. For oil, again a cubic cell (2.47 nm) was built at the same temperature, using 30 molecules of stearic acid

at a density d close to 0.94 g/cm³; moreover, 500 water molecules, 12 laurate ions, and 12 Na⁺ were placed in a cubic cell of length 2.56 nm at a density d close to 1.01 g/cm³. After an initial energy minimization, the simulation cell was subjected to 0.05 ns of NVT MD simulation, using velocity scaling to quickly establish the temperature for the first 0.01 ns, followed by 0.04 ns using the Andersen thermostat.^[28] Density equilibration was then achieved by performing further 1 ns of constant pressure-constant temperature (NPT) MD simulations again using the Andersen thermostat and the Berendsen barostat^[20] to maintain pressure. *Compass* was again the force field of choice, since it has been demonstrated to be able to predict with high accuracy the densities of a number of liquids and liquid mixtures at different state points.^[16] The atom-based method with a cutoff of 9.5 Å was used to treat both electrostatic and Van der Waals interactions. All MD runs were performed with the *Discover* engine of *Materials Studio* (v. 5.1, Accelrys Inc., San Diego, CA, USA) using 24 CPUs of our *MOSE20* cluster. The final side lengths of the water, oil, and surfactants/water boxes obtained were 2.29 nm, 2.48 nm and 2.37 nm, respectively.

Polymer model.

A cell with a size length close to that of the fluid box was built for each polymer. The same procedure described for the polymer construction in pathway 1 was employed. The corresponding amorphous cell was then equilibrated at the required density by the same sequences of NVT and NPT MD simulations described above.

Generation of thin films.

Thin films of liquid and polymer were subsequently generated from the corresponding bulk model cells by elongating one of the periodic boundary conditions until the parent chains no longer interact with their images along that coordinate. Thus, each cell was extended to 15 nm in the z-direction.

Surface tension calculation.

The surface tension γ is one of the most important properties for characterizing a surface, which is related to the disruption of molecular interactions when new interfaces are created. For free surfaces, γ can be

calculated as the excess energy at the surface of a material compared to the bulk, i.e., the Gibbs definition, which can be adapted to the case of polymer films as follows. According to Mansfield and Theodorou,^[29] the fundamental equation for the film phase in energy representation is:

$$dU = T dS - P dV + \mu dn + \gamma da \quad (4.11)$$

where T , S , V , μ , n , γ and a stand for temperature, entropy, volume, chemical potential, number of moles, total surface area (both sides), and surface tension, respectively. If the Helmholtz free energy A is introduced as the first Legendre transform of the internal energy U with respect to entropy S , then:

$$dA = -S dT - P dV + \mu dn + \gamma da \quad (4.12)$$

Accordingly, the surface tension γ can be expressed as:

$$\gamma = \left. \frac{\partial A}{\partial a} \right|_{T,V,n} = \left. \frac{\partial U}{\partial a} \right|_{T,V,n} - T \left. \frac{\partial S}{\partial a} \right|_{T,V,n} = \gamma^U + \gamma^S \quad (4.13)$$

Furthermore, by a Maxwell relation on Eq. (4.12), the entropic contribution to γ , γ^S , can be shown to be equal to:

$$\gamma^S = T \left. \frac{\partial \gamma}{\partial T} \right|_{T,V,a} \quad (4.14)$$

so that a rearrangement of Eq. (4.13), combined with Eq. (4.14), yields:

$$\gamma^U = \left. \frac{\partial U}{\partial a} \right|_{T,V,n} = \gamma + T \left. \frac{\partial S}{\partial a} \right|_{T,V,n} \approx \gamma - T \frac{d\gamma}{dT} \quad (4.15)$$

Mansfield and Theodorou also demonstrated that very $\left(\frac{\partial U}{\partial a} \right)_{T,V,n}$ accurate values can be obtained by calculating the internal energy difference between a thin film model and a bulk liquid model with the same number of molecule at the same temperature.^[29] According to their approach, for such a configuration these values can be calculated using the following expression:

$$\gamma^U = \frac{\langle U_{2D} \rangle - \langle U_{3D} \rangle}{2L_x L_y} \quad (4.16)$$

in which $2L_xL_y$ denotes the total surface area of the two surfaces created on both sides of the bulk cell, L_x and L_y being the dimensions of the film in the x and y direction, respectively (whereas L_z is the direction normal to the film surface). $\langle U_{2D} \rangle$ and $\langle U_{3D} \rangle$ represent the average internal energy of the model system in the film and bulk states and, as such, can be calculated from the corresponding molecular dynamics simulations under the same NVT conditions.

Thus, each equilibrated bulk model and thin film cells obtained as described above was subjected to 400 ps of NVT MD simulation at 298 K. Of the entire trajectory, only the last 200 ps were used in the subsequent analysis. Under the perspective of the theory presented above, the internal energy contribution to the surface tension γ^U of each system was then calculated from the corresponding difference in the MD average energy between the thin film and the MD average energy of the corresponding bulk cell, divided by the surface area, as given by Eq. (4.17):

$$\gamma^U = \frac{\langle U_{2D} \rangle - \langle U_{3D} \rangle}{A} \approx \gamma \quad (4.17)$$

where $\langle U_{2D} \rangle$ and $\langle U_{3D} \rangle$ represent the average potential energy of each model system in the thin film and bulk states, respectively. These quantities were obtained directly from the equilibrated portions of the corresponding MD simulations.

In the present work, however, we reasoned that the use of a flat area (i.e., $2L_xL_y$ in Eq. (4.16)) for the calculation of γ^U was not appropriate for the thin film model as the surface of such model is rough. Thus, in order to properly account for amorphous polymer surface roughness, we replaced the flat area term $2L_xL_y$ with the corresponding value of the solvent accessible surface area $A^{[30]}$, as shown in Eq. (4.17). According to its concept,^[31] the solvent accessible surface area A of a given molecule is generated by the center of a solvent molecule probe, modeled as a rigid sphere, when it is being rolled over the van der Waals surface of the compound molecular model; obviously, different surface areas would be obtained using probes with different radii. In the present work, the van der Waals radius of one molecule of water (1.4 Å) was chosen as the probe radius for water. In the case of oil and surfactants/water, however, a series

of probes with different radii were tested by averaging the corresponding A values over 20 snapshots extracted from the oil equilibrated 300 ps MD trajectory. The value of the probe radius for which the corresponding value of A yielded a total volume equal to the volume of the 3D periodic simulation cell from which the thin film model was generated – 0.54 Å – was then selected. This criterion has already been successfully employed for normal alkanes and methyl methacrylate oligomers models.^[32]

Finally we note that, strictly speaking, the right-hand side of Eq. (4.15) is experimentally measurable. That means that, according to the present formulation, the entropic contribution to γ (i.e., $\gamma^s = T \left. \frac{\partial \Delta S}{\partial a} \right|_{T, V, n} = -T \frac{d\gamma}{dT}$) is neglected as we assume $\gamma \approx \gamma^\mu$ (Eq. (4.17)).

Importantly, however, in their seminal works Mansfield and Theodorou^[29] clearly demonstrated that for polymer surfaces the MD predicted values of γ^μ are within 7% of the corresponding experimental γ values. Also, in a series of related computational studies^[33] Mattice et al. found that reasonable predictions of surface tensions of different polymers could be obtained by ignoring the entropic term in Eq. (4.15). To provide further confirmation to the validity of the underlying $\gamma \approx \gamma^\mu$, the rationale proposed by Heinz^[34] can be adopted. Thus, in the case of water for instance, the entropic contribution to γ may arise from the first layer of partially immobilized, superficial water molecules. Now, the experimental melting enthalpy of ice is 6.01 kJ/mol at 273.15 K,^[35] and this corresponds to an entropy of freezing $\Delta S = -22$ J/(mol K). Thus, the calculated contribution of γ^s to γ for water in our case is equal to 0.53 mJ/m² which, compared to the corresponding γ ($\approx \gamma^\mu$) value of 62.3 ± 1.4 is clearly negligible.

The values of $\langle U_{2D} \rangle$, $\langle U_{3D} \rangle$, A , and the corresponding γ values obtained for amorphous polymer systems are listed in Table 4.1.

System	$\langle U_{2D} \rangle$ [mJ]	$\langle U_{3D} \rangle$ [mJ]	A [m ²]
PP	-6.13E-15 ± 2.23E-17	-7.97E-15 ± 1.97E-17	6.04E-17
PS	-1.50 E-15 ± 1.61E-17	-3.35E-15 ± 1.60E-17	4.14E-17
PA6	-3.34E-14 ± 1.65E-17	-3.66E-14 ± 1.86E-17	7.01E-17
cellulose	2.16E-14 ± 2.67E-17	1.92E-14 ± 2.20E-17	4.11E-17
water	-2.15E-14 ± 2.08E-17	-2.28E-14 ± 1.95E-17	2.01E-17
oil	-2.29E-14 ± 2.06E-17	-2.45E-14 ± 1.95E-17	4.31E-17
soap/water	-4.33 E-14 ± 2.39E-17	-4.49E-14 ± 2.28E-17	5.47E-17

Table 4.1: Values of the parameters $\langle U_{2D} \rangle$, $\langle U_{3D} \rangle$, and A obtained for the systems by the MD-based procedure employed in this work.

Interface tension calculation.

The models required to estimate interface tension values were prepared by placing the corresponding 3D liquid and polymer models in close vicinity but carefully avoiding overlaps^[36] with the aid of the *Layer Builder* modulus of *Materials Studio*. Thus, starting from the equilibrated 3D models of polymer and each liquid, after an initial minimization the resulting systems were subjected to 500 ps of NVT MD simulation at 298 K. In this case, the atom-based method with a cutoff of 15.5 Å was used to treat both electrostatic and van der Waals interactions. The last 100 ps of the equilibrated MD trajectories were exploited to calculate the interface energy and, by means of Equation (4.13), the interfacial tension could ultimately be estimated as:

$$\gamma_i = \frac{\langle U_i \rangle - (\langle U_l \rangle + \langle U_p \rangle)}{A_i} \quad (4.18)$$

Where $\langle U_i \rangle$ is the average potential energy of the interface, $\langle U_l \rangle$ and $\langle U_p \rangle$ are the energy of the liquid and polymer thin film models, respectively, and A_i is the interface area. Table 4.2 reports the values of all parameters in Eq. (4.18) as obtained for the systems investigated.

System	$\langle U_i \rangle$ [mJ]	$\langle U_l \rangle$ [mJ]	$\langle U_p \rangle$ [mJ]	A_i [m ²]
PP/water	-3.04E-14 ± 3.07E-17	-2.15E-14 ± 2.08E-17	-6.13E-15 ± 2.23E-17	6.04E-17
PS/water	-2.17E-14 ± 2.84E-17	-2.15E-14 ± 2.08E-17	-1.50 E-15 ± 1.61E-17	4.14E-17
CELL/water	-4.82E-16 ± 3.43E-17	-2.15E-14 ± 2.08E-17	2.16E-14 ± 2.67E-17	7.01E-17
PA6/water	-5.38E-14 ± 3.28E-17	-2.15E-14 ± 2.08E-17	-3.34E-14 ± 1.65E-17	4.11E-17
PP/oil	-2.67E-14 ± 2.46E-17	-2.29E-14 ± 2.06E-17	-6.13E-15 ± 2.23E-17	6.04E-17
PS/oil	-2.31E-14 ± 2.43E-17	-2.29E-14 ± 2.06E-17	-1.50 E-15 ± 1.61E-17	4.14E-17
CELL/oil	4.62E-16 ± 2.48E-17	-2.29E-14 ± 2.06E-17	2.16E-14 ± 2.67E-17	7.01E-17
PA6/oil	-5.20E-14 ± 5.51E-17	-2.29E-14 ± 2.06E-17	-3.34E-14 ± 1.65E-17	4.11E-17
PP/surfactant&water	-4.69E-14 ± 3.12E-17	-4.33 E-14 ± 2.39E-17	-6.13E-15 ± 2.23E-17	6.04E-17
PS/surfactant&water	-4.30E-14 ± 3.24E-17	-4.33 E-14 ± 2.39E-17	-1.50 E-15 ± 1.61E-17	4.14E-17
CELL/surfactant&water	-2.05E-14 ± 3.97E-17	-4.33 E-14 ± 2.39E-17	2.16E-14 ± 2.67E-17	7.01E-17
PA6/surfactant&water	-7.44E-14 ± 4.52E-17	-4.33 E-14 ± 2.39E-17	-3.34E-14 ± 1.65E-17	4.11E-17

Table 4.2: Values of the parameters $\langle U_i \rangle$, $\langle U_l \rangle$, $\langle U_p \rangle$, and A_i obtained for all the systems by the MD-based procedure employed in this work.

Work of adhesion calculation via P1 and P2.

Exploiting all information retrieved from both simulation pathways *P1* and *P2* presented in this work, the values of the work of adhesion W_{adh} between each polymer/fluid system was estimated using two, alternative

procedures. According to route 1, the values of the work of adhesion between a fluid and a polymer were calculated by substituting the appropriate contact angle value θ and inserting the surface tension values obtained via P2 simulation in the Young-Dupré equation^[27]:

$$W_{adh}^1 = \gamma_{liq}(1 + \cos\theta) \quad (4.19)$$

Following the route 2, the values of work of adhesion were estimating as using the appropriate values of surface tension and interfacial tension obtained via P2 simulation in the Equation (4.8).

4.3 Effect of surface nature on wetting behavior of amorphous polymers

4.3.1 Result from path 1

The hydrophilic/hydrophobic nature of surfaces determines to what extent they are wetted by liquids. The wetting property of a given surface is commonly characterized through a measurement of the contact angle that a droplet makes with the surface of the substrate. In this study, contact angles were determined from the equilibrium shape that a water droplet assumed when it was deposited on an amorphous surface. The equilibrium shape of the droplet corresponds to the situation where the center of mass of the droplet remains a constant distance from the substrate as a function of time.

Figures 4.3, 4.4, 4.5 and 4.6 shows MD snapshot views from the top and the side of the dynamics course of a typical droplet of pure water (left panels), oil (middle panels), and surfactants/water (left panels) spreading on polymer surface obtained from the application of protocol P1, while the corresponding radial density distribution (RDD) profiles obtained from the relevant equilibrated MD trajectories are shown in Figure 4.7. The relevant values of the contact angle θ estimated are listed in Table 4.3.

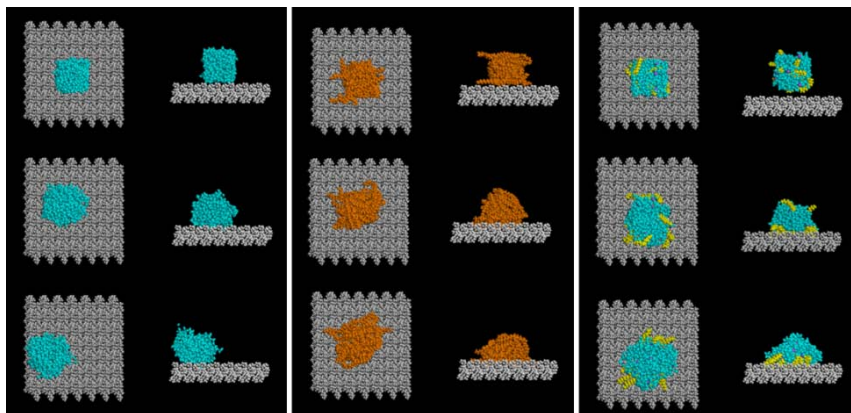


Figure 4.3: Snapshots (top and side views) of the dynamics course of water (light blue, left panels), oil (orange, middle panel) and surfactants/water(yellow and light blue, respectively) spreading on the PP surface (gray) at a simulation time of 0 ps, 250 ps, and 500 ps.

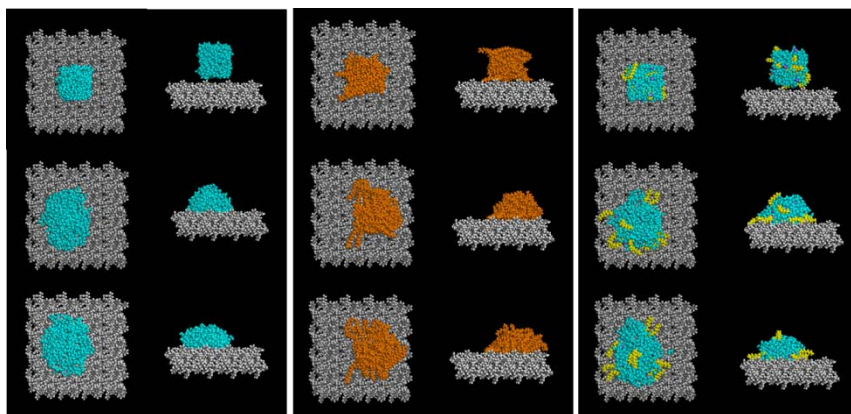


Figure 4.4: Snapshots (top and side views) of the dynamics course of water (light blue, left panels), oil (orange, middle panel) and surfactants/water(yellow and light blue, respectively) spreading on the PS surface (gray) at a simulation time of 0 ps, 250 ps, and 500 ps.

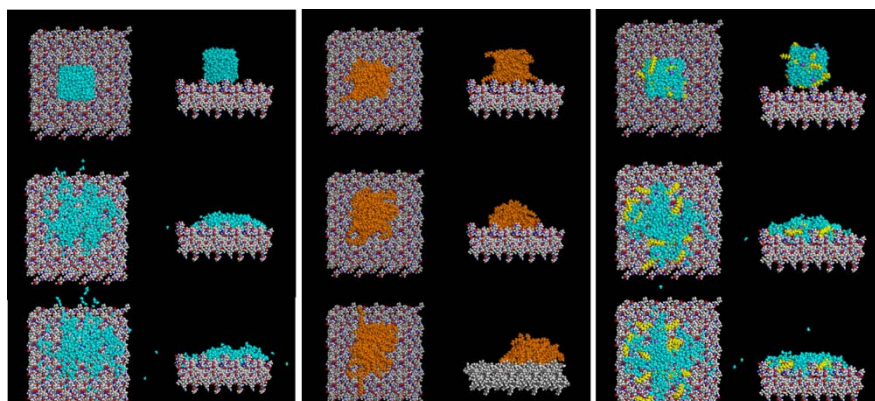


Figure4.5: Snapshots (top and side views) of the dynamics course of water (light blue, left panels), oil (orange, middle panel) and surfactants/water(yellow and light blue, respectively) spreading on the PA6 surface (gray/red/blue) at a simulation time of 0 ps, 250 ps, and 500 ps.

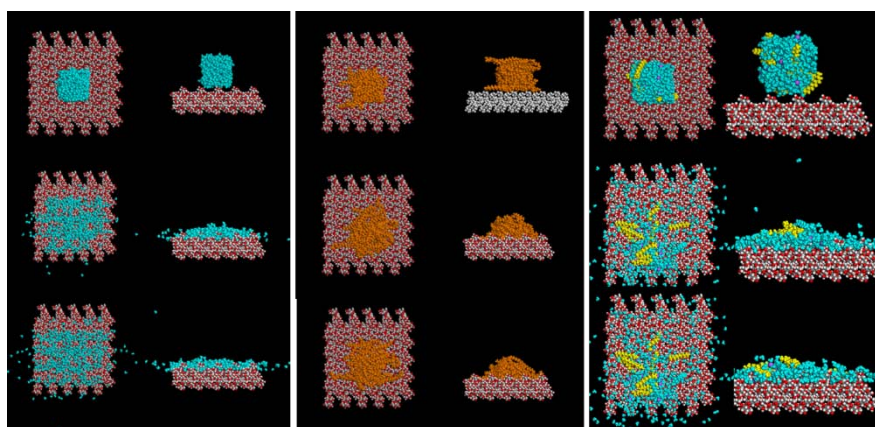


Figure 4.6: Snapshots (top and side views) of the dynamics course of water (light blue, left panels), oil (orange, middle panel) and surfactants/water(yellow and light blue, respectively) spreading on the cellulose surface (gray/red) at a simulation time of 0 ps, 250 ps, and 500 ps.

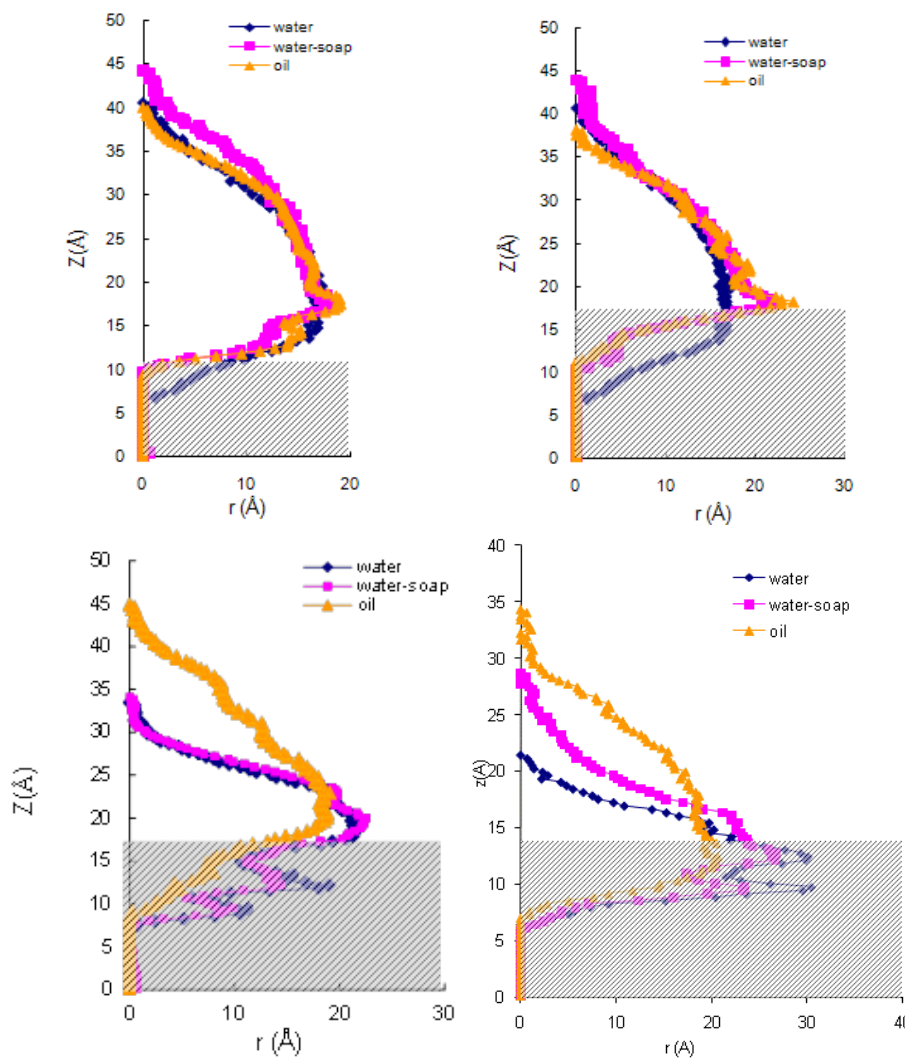


Figure4.7:Radial density distribution profiles for a water (blue), oil (orange), and surfactant/water (pink) droplet spreading on the PP (top left), PS (top right), PA6 (bottom left) and cellulose (bottom right).

System	θ	W_{adh}
PP/water	109 ± 6 (108) ^[26]	43.0±8.4
PS/water	91.1± 5.6(91) ^[27]	61.0 ± 7.7
PA6/water	72.7 ± 4.4(71) ^[28]	80.8 ± 6.4
cellulose/water	27.8 ± 6.8 (30) ^[29]	117.4 ± 5.4
PP/oil	103.2 ± 2.5	27.1 ± 3.9
PS/oil	80.8 ± 5.4	40.7 ± 7.4
PA6/oil	111.0 ± 2.9	22.5 ± 3.8
cellulose/oil	81.3 ± 1.5	40.4 ± 5.1
PP/surfactant&water	111.2 ± 4.0	19.3 ± 6.3
PS/ surfactant&water	101.5 ± 2.0	24.2 ± 8.4
PA6/ surfactant&water	73.0 ± 4.9	39.1 ± 10.8
cellulose/surfactant&water	54.9 ± 3.2	47.7 ± 12.4

Table 4.3: Contact angle θ (°) and work of adhesion W_{adh} (mN/m) according to Pathway 1 for the systems studied in this work. Available experimental values are shown in parenthesis for comparison.

Further evidences of the wetting behavior on different substrates can be retrieved from the binding energies of each polymer/fluid system reported in Table 4.4.

System	Binding energies [kcal/mol]	non bond tot [kcal/mol]	vdW [kcal/mol]	Coulomb [kcal/mol]
PP/water	-32.92	-50.64	-31.82	-18.82
PS/water	-208.41	-208.41	-99.89	-108.53
PA6/water	-1953.78	-1953.78	-196.73	-1757.05
cellulose/water	-2131.69	-2131.69	19.73	-2151.41
PP/oil	-170.43	-170.43	-169.85	-0.85
PS/oil	-261.12	-261.12	-246.20	-14.92
PA6/oil	-431.76	-431.76	-337.39	-94.37
cellulose/oil	-227.69	-447.69	-280.76	-166.93
PP/surfactant&water	-137.39	-137.39	-136.59	-0.79
PS/ surfactant&water	-327.02	-327.04	-202.31	-124.73
PA6/ surfactant&water	-1898.66	-1905.55	-430.66	-1474.89
cellulose/surfactant&water	-1922.55	-1925.01	-83.31	-1841.70

Table 4.4: MD calculated non bond contribution to the binding energies of each polymer/fluid system studied.

As indicated in Table 4.4, the interaction energy between water and PP is mostly comprised of van der Waals interactions; there is very little

electrostatic energy and no hydrogen bonding because PP does not have any polar groups or H-bond donors/acceptors. On the contrary, the interaction energy with cellulose is comprised mostly of electrostatic and hydrogen bonding energies, with the latter being the most important and explained by the interactions between water and the hydroxyl groups of cellulose. The van der Waals energy makes a small contribution to the total energy with a value on the same order as that for water and PP.

As highlighted in the results reported above, the contact angle of a water nanodroplet results larger than 90° for PP and PS, which indicates that they are hydrophobic surfaces; on the contrary, contact angles smaller than 90° indicate a hydrophilic surface, as in the cases of PA6 and cellulose. These is in agreement with experimental data.

In the presence of an oil nanodroplet PP and PS surfaces show a decrease in the contact angle with respect to water systems; on the contrary, PA6 and cellulose show an increase in the contact angles, this is due to the polar nature of the polymers which contrast the polar head of the oil chains.

Surfactants molecule, as we already said, are made up of a water soluble (hydrophilic) and a water insoluble (hydrophobic) component. In fact we can see the hydrophilic head (Na^+ ions) of the surfactant is orientated toward the water molecules and the hydrocarbon hydrophobic tail toward the polymeric surface, increasing the intermolecular interactions. We have found that the presence of surfactant molecules in the water nanodroplet increases the contact angle in all systems studied with respect to pure water. This confirms that surfactant plays an important role in the wettability process: increasing the contact angle with respect to water and decrease the work adhesion (see Table 4.3).

4.3.1.1 Results from Pathway 2

Figura4.8 shows the 3D and 2D models developed for PP and PA6, and the interface model for water/PP and water/PA6 systems employed in the calculation of the surface and interfacial tensions according to the second computational approach adopted (P2).

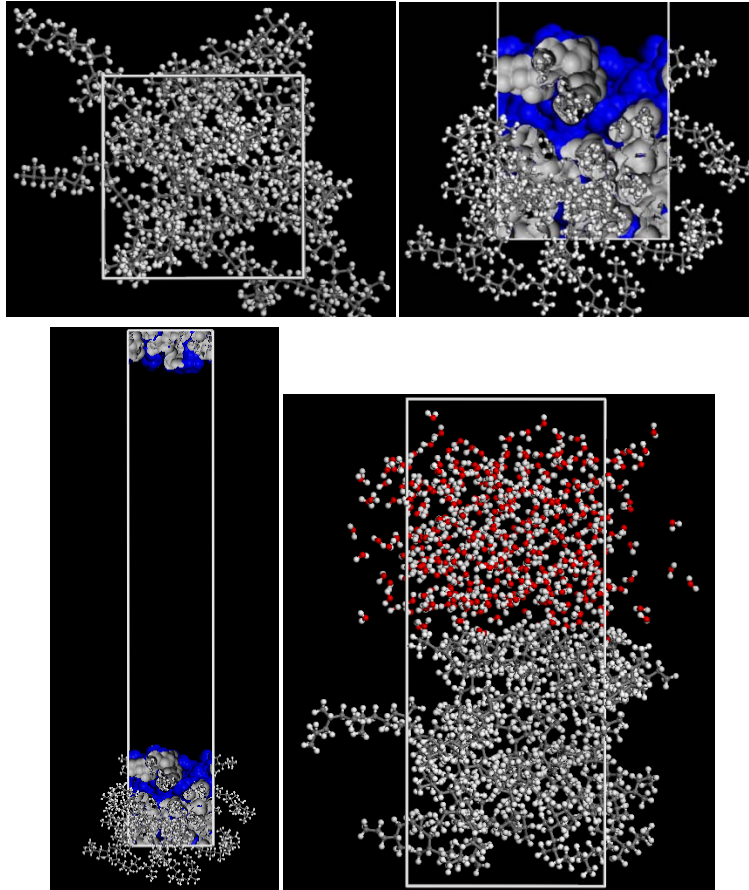


Figure 4.8: 3D model of PP (top left), zoomed view of the 2D model of PP (top right) shown in full in the bottom left panel, and interface model (bottom right) for the water/PP system.

Sysetm	γ_{calc}	γ_{exp}
PP	30.5 ± 5.0	$32.0^{[30]}$
PS	45.3 ± 2.8	$43.0^{[31]}$
PA6	46.2 ± 5.0	$48.0^{[28]}$
cellulose	58.7 ± 3.2	$57.7^{[32]}$
water	62.3 ± 1.4	$71.7^{[33]}$
oil	35.1 ± 3.0	$32.8^{[34]}$
surfactant/water	30.3 ± 3.0	$<30^{[34]}$

Table 4.5: Liquid surface tension γ_{calc} (mJ/m²) predicted according to the pathway 2. The corresponding experimental value γ_{exp} is reported in the last column

Further, Table 4.5 and Table 4.6 show liquid surface tension γ_{calc} , the polymer/liquid interfacial tension γ , the work adhesion W_{adh} , and the

spread coefficient S values obtained for each corresponding system as computed by path 2.

System	γ		W_{adh}		S
PP/water	44.4	\pm 7.3	48.3	\pm 8.9	-76.2
PS/water	33.1	\pm 9.4	74.5	\pm 11.0	-50.1
PA6_H2O	15.2	\pm 6.7	93.3	\pm 8.5	-31.3
cellulose/water	-11.9	\pm 10.6	132.9	\pm 12.5	8.3
PP/oil	40.3	\pm 6.6	25.3	\pm 8.8	-44.9
PS/oil	31.7	\pm 8.7	48.7	\pm 10.8	-21.5
PA6/oil	62.0	\pm 9.3	19.4	\pm 10.9	-50.9
cellulose/water	45.3	\pm 8.9	48.6	\pm 11.5	-21.7
PP/surfactant&water	42.1	\pm 7.6	18.7	\pm 10.9	-41.9
PS/ surfactant&water	43.9	\pm 10.6	31.7	\pm 13.5	-28.9
PA6/ surfactant&water	32.4	\pm 8.2	44.1	\pm 11.4	-16.5
cellulose/ surfactant&water	29.9	\pm 12.0	59.2	\pm 15.0	-1.5

Table 4.6: Polymer/liquid interfacial tension γ (mJ/m²), work of adhesion W_{adh} (mN/m), and spread coefficient S (-) for the systems studied in this work.

The spreading coefficient S is defined as $S = \gamma_p - \gamma - \gamma_l$; as such, positive values of S indicate that the liquid polymer will spread onto the polymer surface, while negative values imply that water tends to contract, and a value of zero means the liquid has no propensity to wet the solid surface.

The γ values for both water and oil estimated according to P2 are listed in the first column of Table 4.5, and are found to be in good agreement with the corresponding experimental counterparts. In the case of water, it is important to observe that the simple and relatively fast way proposed in the present work to predict the water γ is in excellent agreement with the values obtained from more sophisticated approaches such as the virial method ($\gamma = 63.7$ mJ/m²) and the test area method ($\gamma = 63.5$ mJ/m²).^[44, 46] Notably, also the value of γ_p obtained for PP (30.5 ± 1.2 mJ/m²) matches the most common value reported in literature of 32 mJ/m².^[41] The corresponding values of the interfacial tensions γ are reported in the first column of Table 4.6.

The second column of Table 4.6 show the value of W_{adh} estimated for each fluid/polymer system via P2 using Equation (4.8). As can be inferred from these data, the W_{adh} value obtained in the case of water and PP is

higher than that estimated for oil on the same polymeric surface, as expected.

To further verify the reliability of both computational pathways in predicting consistent and reliable values of θ , γ_l , and W_{adh} for the systems considered, we finally exploited the θ values for water, oil, and surfactant/water obtained via P1 and the γ values obtained by P2 in the alternative W_{adh} expression given by Equation (4.8), obtaining the values reported in Table 4.6. Pleasingly, the two sets of W_{adh} values estimated by the two different MD simulation protocols adopted in the present work are in good agreement with each other, thus confirming the reliability of the computational recipes in predicting the values of fundamental quantities characterizing the spreading of water and oil onto an amorphous polymeric surface (see Figure 4.9)

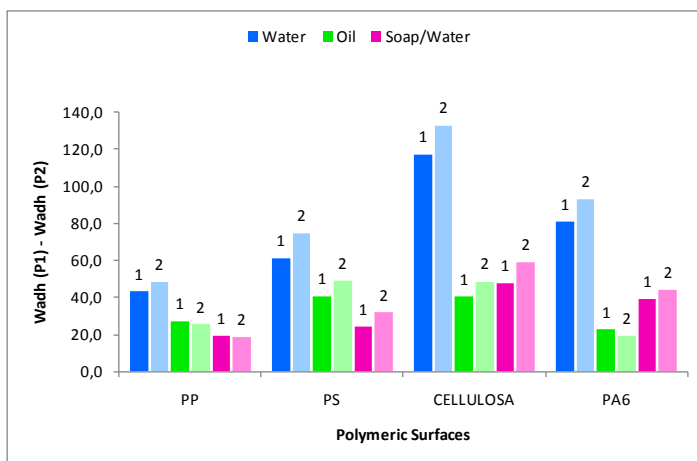


Figure 4.9: Comparison of W_{adh} values obtained via path1 and via path 2 for all system studied

4.3.2 Wettability analysis of fluorinated amorphous surfaces

We employed the computational protocols proposed in the previous paragraphs to analyze the wettability of seven different aromatic fluoropolymers (Figura4.10). MD simulations of these polymer in contact with water nanodroplet were performed using *Material Studio* (v. 5.0, Accelrys Inc., San Diego, CA, USA) and employing the COMPASS force field to describe the potential of the systems. COMPASS force field has been demonstrated to be able to predict with high accuracy the densities

of a number of liquids at different state points [28]. Moreover, the accuracy of COMPASS to treat fluoropolymers has been already demonstrated in other works.^[47]

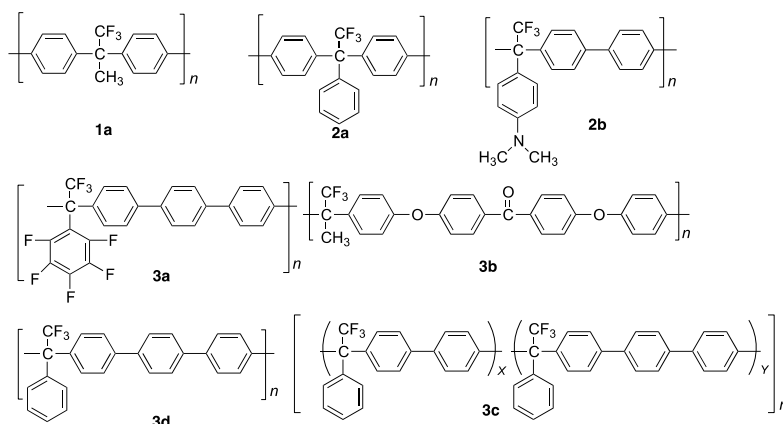


Figura4.10: Structures of Amorphous aromatic fluoropolymers and acronyms. **(1a)** = Trifluoroacetone with benzene (CF3_74); **(2a)** = 2,2,2 - Trifluoroacetophenone with biphenyl (CF3_194); **(2b)** = Aminobenzaphenone with biphenyl (CF3_137); **(3a)** = Pentafluoroacetophenone with terphenyl (CF3_138); **(3b)** =Trifluoroacetone with 4,4 Diphenoxybenzophenone (CF3_140); **(3c)** = Trifluoroacetophenone with biphenyl and terphenyl (CF3_277); **(3d)** = Trifluoroacetophenone with therphenyl (CF3_279).

4.3.2.1 Computational recipe

We quantify contact angle (θ), surface tension (γ) and work of adhesion (W_{adh}) of a polymeric surface in contact with water using a combination of the two different computational recipes described before: the first one to calculate γ (Eq.4.9 and 4.10) and the second one to compute θ (Eq. 4.1, 4.2, 4.3, and 4.4). Finally we combine the θ and γ values resulting from the two simulation pathways to obtain the corresponding values of W_{adh} using the Young- Dupré equation (Eq. 4.19).

In addition we evaluate other two parameter. The first one is the surface roughness, which plays a significant role in influencing the surface properties; and the other one is the partition coefficient, that is a measure of the hydrophobicity of a substance.

Surface roughness

Another fundamental feature of surfaces is the texture, or roughness, of polymer surfaces, and its role in molecular interactions. Surface roughness is, in fact, an important parameter to be considered since it plays a significant role in influencing the surface properties and

hence the performance of materials. The surface and interfacial properties depend critically upon details of the molecular structures at the polymer surface or interface. It has been well-established that the wettability of a solid surface is governed by both the surface chemical composition and the surface geometrical microstructures. The chemical compositions^[48] determine the surface free energy and thus have great influence on wettability. However, it has certain limitation. For example, the -CF₃-terminated surface was reported to possess the lowest free energy and the best hydrophobicity, while on flat surfaces, the maximum contact angle could only reach about 120°^[49].

The surface topographic nanostructure is also an important factor that influences the wettability. The irregularity of a surface may be described^[50] through the measurement of the fractal dimension d_f of the surface. According to a known, validated procedure,^[51-54] the value of d_f , usually interpreted as the fractal dimension of the surface available to adsorption, may be obtained from the slope of the $\log(A_c) - \log(r_p)$ curve as follows:

$$2 - d_f = \frac{d \log(A_c)}{d \log(r_p)} \quad (4.16)$$

A_c is the contact component of the Connolly molecular surface^[55-57] and r_p is the probe radius. According to this definition, the molecular surface consists of the van der Waals surface of the atoms that can be touched by a solvent-sized probe sphere (thus called contact surface), connected by a network of concave and saddle surfaces (globally called reentrant surface). Thus, A_c accounts for the superficial contacts between different macromolecules. Consequently, d_f gives information concerning the surface roughness and accessibility of macromolecules. Indeed, according to its definition, as a molecular surface becomes more irregular, the corresponding fractal dimension increases, starting from its lower value $d_f = 2$, equivalent to an entirely smooth surface, up to an extreme, volumelike irregularity ($d_f = 3$).^[58]

Partition Coefficient

Hydrophobicity, can be also measured experimentally using 1-octanol to water partition coefficients, P , i.e. the ratio of the concentration

of the compound in the oil phase divided by its concentration in water. Because of the order of magnitude variation in P , $\log(P)$ is considered; the larger $\log(P)$, the more hydrophobic is the molecule. The partition coefficient ($\log P$) of small molecules can be calculated as the sum of the contributions of each of the atoms in the molecules. So the value of $\log(P)$ can also now be estimated quite accurately from the chemical formula based on previous correlations between molecular structure and experimental $\log(P)$ data. We have calculated $\log(P)$ using the ALOGP method, which is among the most prominent methods of predicting $\log P$ and it is implemented in Material Studio package. ALOGP is the atomic contribution method developed by Ghose and Crippen^[59,60] and later refined by Ghose and co-workers.^[61-63] This method is based on an additive scheme of atomic lipophilicity constants, it assigns to the individual atoms in the molecule additive contributions to molecular $\log P$. This is accomplished by classifying atoms into chemically distinct types and fitting the contributions on a data set of experimentally determined $\log P$ values.

4.3.2.2 Results and discussion

The adhesion of water on a polymer surface is determined by the intermolecular forces such as electrostatic interactions, Van der Waals forces and chemical interactions, (ionic and covalent bonding). The effects of molecular and chemical interactions at material interfaces are not accounted in many analytical models and are difficult to ascertain experimentally. MD simulation can provide information on interfacial strength at a more fundamental level.

The wetting of a surface is essentially determined by molecular interactions between the surface and the liquid, contact angle (θ), surface tension (γ), and work of adhesion (W_{adh}) being the most popular physical parameters used to quantify these phenomena. Thus, approaches based on atomistic molecular simulations should, in principle, yield vital insights on these interactions and constitute ideal tools to estimate the related technological parameter values.

The contact angle is the interaction between the liquid and solid in the geometric form, while the surface tension is an intrinsic property of the polymer that means, the force that needed for break tension of the

area. However in order to get a better understanding of the wetting phenomenon the work of adhesion needs it.

Through these efforts, we wished to develop a greater understanding of the relationships between the structure and the interfacial properties of aromatic fluoropolymer surfaces. Importantly, the observed trends in wettability are evaluated here for the first time in the context of surface properties of aromatic fluoropolymers. Manipulating the hydrophobicity/hydrophilicity of a given surface necessarily requires understanding the micro-scale principles that, in turn, control the macro-scale surface wetting behavior. Therefore, understanding the structure and behavior of common fluid such as water at the interface with aromatic fluoropolymers is of great practical importance. On the contrary, computational studies dealing with water spreading onto amorphous polymer surfaces are quite scarce, and this paucity may be ascribed to the fact that constructing a well-defined model for amorphous polymer surfaces and simulating systems having interfacial regions with unconfined roughness requires notable computational time and resources.

To the best of our knowledge, this is the first attempt to study the behavior of water molecules on aromatic fluoropolymer surfaces, estimating Contact angle, Work adhesion and surface tension by molecular dynamic simulation. Figure 4.10 shows some MD snapshot of a pure water droplet spreading on three of the fluoropolymers surface studied. It is represented the fluoropolymer with the smaller hydrophobic character (CF3_74), the polymer with the bigger hydrophobic character (CF3_279), and CF3_137 which has an intermediate behavior. The values obtained from the simulations and experimental data of contact angle, surface tension, work of adhesion spread coefficient and interface surface tension are listed in Tables 4.7 and 4.8. The instantaneous contact angle is calculated for the last 100 frames of the MD trajectory of each system. As can be inferred from these values, the application of our computational protocol yielded a θ value for water in contact with aromatic fluoropolymers in astoundingly good agreement with the corresponding experimental evidence. Weaker attractions between liquid and solid molecules result in higher contact angles and lower work of adhesion. The smaller angle (θ) indicates a surface that is more wettable and therefore would allow a more effective bond to be achieved. Generally, if the water

contact angle is larger than 90° , the solid surface is considered hydrophobic. Highly hydrophobic surfaces made of low surface energy.

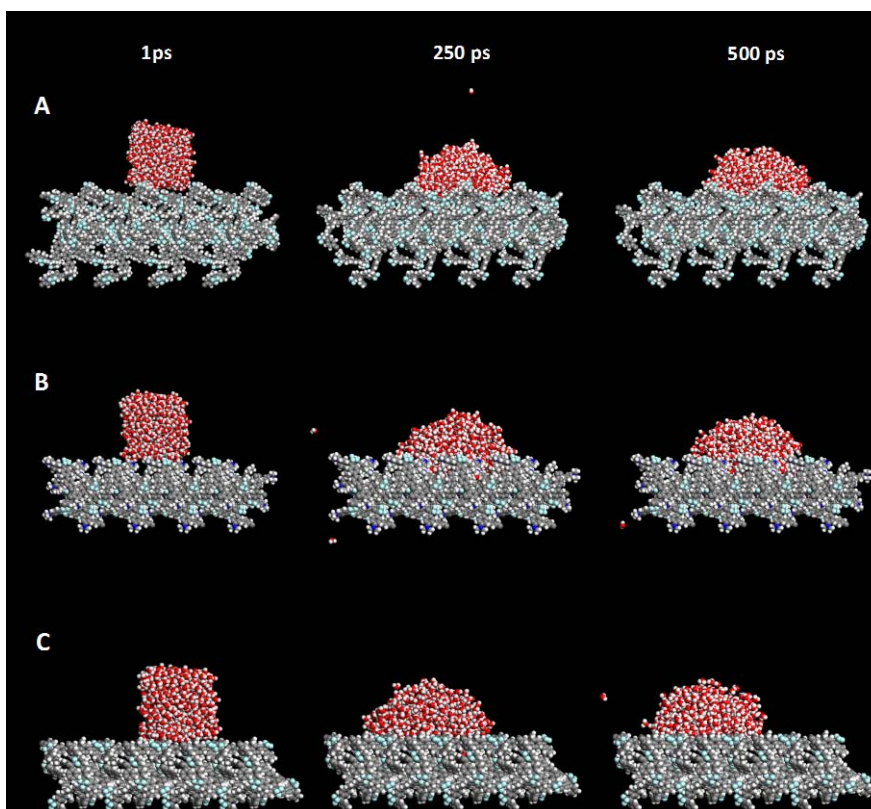


Figure 4.11: Snapshots of the MD simulations of water droplet on aromatic fluoropolymer surfaces. In panel A it is reported CF3_74, in panel B CF3_137 and in panel C CF3_138.

System	θ		γ (mJ/m ²)		Wadh (mJ/m ²)	
	Exp.	Sim.	Exp.	Sim.	Exp.	Sim.
CF3_74	85,0 ± 2,0	88,7 ± 4,3	15,3 ± 0,3	16,8 ± 5,5	67,6 ± 3,8	63,8 ± 4,5
CF3_140	94,6 ± 2,3	96,6 ± 3,1	23,4 ± 0,5	22,8 ± 6,5	57,3 ± 3,9	55,2 ± 4,7
CF3_194	90,5 ± 1,4	92,2 ± 3,3	24,4 ± 0,6	21,8 ± 6,8	61,7 ± 2,9	59,9 ± 4,9
CF3_277	94,5 ± 2,3	96,5 ± 3,2	14,9 ± 1,6	18,4 ± 5,4	57,4 ± 3,8	55,3 ± 4,8
CF3_279	94,9 ± 2,0	97,2 ± 2,7	19,9 ± 0,8	21,4 ± 6,1	57,0 ± 3,5	54,4 ± 4,2
CF3_137	90,8 ± 3,0	92,7 ± 3,5	24,8 ± 0,8	22,1 ± 6,8	61,4 ± 4,8	59,4 ± 4,7
CF3_138	93,2 ± 2,8	95,5 ± 5,2	20,9 ± 1,4	22,9 ± 5,2	58,8 ± 4,4	56,3 ± 6,9

Table 4.7: Wettability surfaces properties: Contact angle θ , Surface tension γ , Work of adhesion Wadh, in the simulation and experimental way.

System	S	γ_i (mJ/m ²)	%F _{surf}
CF3_74	-60,8	15,3	22
CF3_140	-69,4	29,9	17
CF3_194	-64,7	24,4	16
CF3_277	-69,3	25,1	31
CF3_279	-70,1	29,2	19
CF3_137	-65,3	25,1	7
CF3_138	-68,3	28,9	18

Table 4.8: Spread coefficient S, the Interface tension γ_i and the percentage of fluorine atoms on surface respect to all fluorine atoms in the simulation cell.

Figura4.12 show that, not only the contact angle values, but also data of surface tension and work of adhesion resulting from the simulations are in excellent agreement with experimental data from Zolutikhin et al. and demonstrate the accuracy of our model also for complex systems like aromatic fluorocarbons.

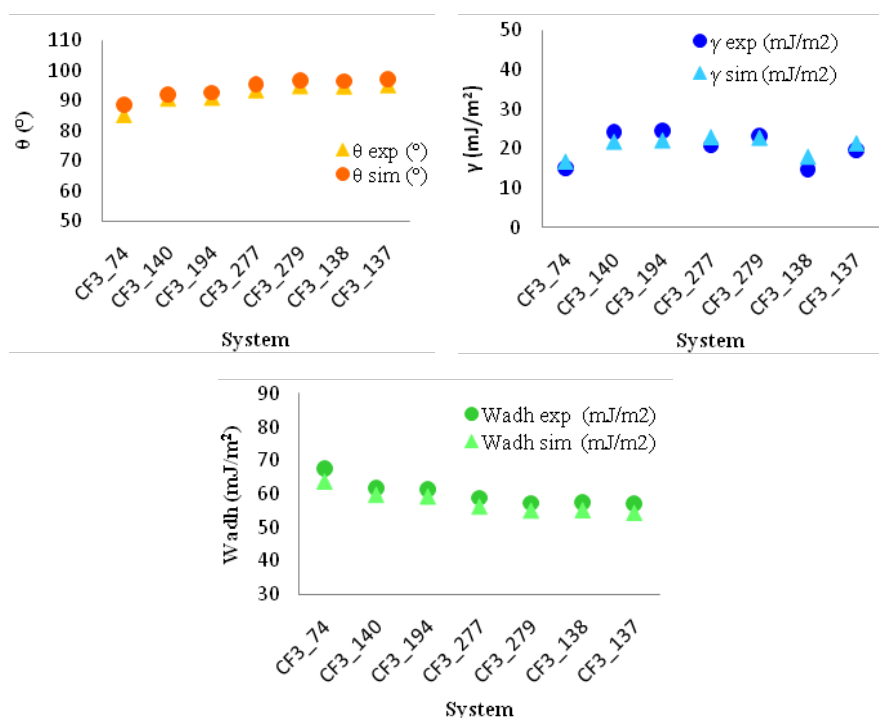


Figura4.12: Comparison between simulated (solid triangle) and experimental values (solid circle) of contact angle, surface tension and work of adhesion.

The contribution of fluorine atoms drastically affects the surface tension, due to the strong C-F bonds; moreover, it is also important taking

into account the contribution of number of aromatic rings in the polymer chain. CF3_74 and CF3_277 have the lowest surface tension (15.3 and 14.9 respectively) and it is because they have 22% and 31% of the total fluorine atoms on the surface. Instead in the case of CF3_137 the bigger value of surface tension corresponds to the lower presence of C-F bond on the surface.

In order to understand the behavior of the work of adhesion, we apply the descriptor of the contribution of the polar and a-polar functional groups. We use a simple and fast QSAR descriptor, implemented in Material Studio package, of the Total A-polar Surface Area (TASA) and Total Polar Surface Area (TPSA) and secondly the Relative A-polar surface area (RPSA) and Relative A-polar Surface Area (RASA)(see Tabella4.9). TPSA is the sum of solvent-accessible surface areas of all polar atoms and TASA is the sum of solvent-accessible surface areas of all apolar atoms; RPSA and RASA are the total polar surface area or the apolar surface area respectively divided by the total solvent-accessible surface area. Forces within liquids and solids and across their interfaces include: *polar interactions* (Van der Waals), Ion-ion, Ion-dipole (H-bond), Dipole-dipole, Dipole-induced dipole and *a-polar interactions* (Hydrophobic dispersion, coulomb forces); the first are represented by TPSA and the second from TASA.

System	Bindingenergies	Vdw	Q	TPSA (Å)	RPSA	TASA (Å)	RASA	AlogP
CF3_74	-91.98	-48.07	-43.90	46.60	0.16	239.07	0.84	6.24
CF3_140	-26.03	-8.34	-17.68	85.28	0.17	411.38	0.83	8.63
CF3_194	-26.58	-14.62	-11.95	43.56	0.13	293.13	0.87	7.45
CF3_277	-16.20	-9.08	-7.13	89.56	0.13	615.50	0.87	15.3
CF3_279	-37.90	-25.23	-12.67	47.09	0.11	377.46	0.89	9.45
CF3_137	-29.70	-11.84	-17.86	51.10	0.13	347.40	0.87	7.73
CF3_138	-30.49	-14.90	-15.59	126.16	0.28	321.81	0.72	9.84

Table 4.9: Binding Energies, van der Waals interactions and electrostatic interactions of all polymer/water systems studied. Total polar surface area (TPSA), Total a-polar surface area (TASA), Relative Polar Surface Area(RPSA), Relative A-polar Surface Area (RASA) and AlogP of aromatic fluoropolymers

Hydrophobicity can be also measured experimentally using 1-octanol to water partition coefficients, P, i.e. the ratio of the concentration of the compound in the oil phase divided by its concentration in water. Because of the order of magnitude variation in P, log(P) is considered; the larger log(P), the more hydrophobic is the molecule. The partition

coefficient ($\log P$) of small molecules can be calculated as the sum of the contributions of each of the atoms in the molecules. Accordingly, the value of $\log(P)$ can also now be estimated quite accurately from the chemical formula based on previous correlations between molecular structure and experimental $\log(P)$ data. We calculated $\log(P)$ using the ALOGP method, which is among the most prominent methods of predicting $\log P$ and it is implemented in Material Studio package. ALOGP is the atomic contribution method developed by Ghose and Crippen^[64,65] and later refined by Ghose and co-workers^[66-68]. This method is based on an additively scheme of atomic lipophilicity constants, it assigns to the individual atoms in the molecule additive contributions to molecular $\log P$. This is accomplished by classifying atoms into chemically distinct types and fitting the contributions on a data set of experimentally determined $\log P$ values.

The trifluoroacetone with benzene (CF3_74) has the smallest contact angle of all fluoropolymers, 85.02°; this is due to its higher polar surface area (RPSA=0.16), which increases the interaction at the interface with the polar water molecules. In fact, more the values of RPSA are large, greater the charge difference and greater the dipole moment of the molecule. Consequently its hydrophobic character is the lowest of all the fluoropolymers, as confirmed also by the values of the highest spread coefficient, -60.8, and of the lower partition coefficient, 6.24 (see Table 4.9). To characterize the interfacial behavior more fully, we calculated the binding energies, which are defined as is the negative of the interaction energy. In Table 4.9 we can see that the binding energy of the trifluoroacetone with benzene is the more negative value (-91.98 kcal/mol) and it has the stronger van der Waals interaction at the interface.

The CF3_279 exhibit the maximum contact angle of all fluoropolymers, 97.2°, this is due to its lower relative polar surface area RPSA of 0.11, which decreases the interaction with the water molecules; consequently, the hydrophobic character of the structure of this polymer is also one of the highest of all the polymers (9.45). Its behavior is confirmed also by the low binding energy (-37.90 kcal/mol).

CF3_140 has a high contact angle of 96.6°, even if the contribution of the polar surface area (RPSA=0.17) is one of the maximum; however the polymer structure consists of four polar groups (trifluoromethyl, carbonyl

and ethers groups) alternated with nucleophilic aromatic rings, and this results in a neutralization of the global charge. We can confirm the hydrophobic character of the CF3_140 with the very low value of binding energy (-26.03 kcal/mol).

Polymer of the *Trifluoroacetophenone* with biphenyl (CF3_194), with a contact angle of 92.2°, represent an intermediated behavior. In fact the value of the corresponding RPSA is 0.13 and therefore the interaction with the molecules of water are greater than CF3_279, but they are less than CF3_74, consequently these fluoropolymer has an intermediate hydrophobic character, as represented by the AlogP value of 7.45.

The co-polymer *Trifluoroacetophenone* with biphenyl and terphenyl (CF3_277) exhibit one of the highest contact angle of all fluoropolymers, 96.5°, because it forms a small polar surface area (RPSA=0.13) and thus the interaction in the interface with the polar molecules of water decrease, this hydrophobic character is also reflected in the highest value of AlogP (15.3) and in the lower value of binding energy (-16.2 kcal/mol). The surface tension of CF3_277 ($\gamma = 18.4$ mN/m) is one of the lower and this because it has the major number of fluorine atoms on the surface (31%).

The aminatedtrifluoroacetophenone with biphenyl group (CF3_137), whose contact angle is 92.7°, represents an intermediate behavior, similar to that of CF3_194. The RPSA is the same of that of CF3_194 and it is low since the polar amine group can balance the polar trifluoromethyl group, neutralizing the charge of the molecule; that means that the dipole moment of the molecule is reduced and consequently can increase the interaction with the molecules of water. Therefore, also the AlogP value is one of the less of all the polymers (7.73), similar to CF3_194. The surface tension of CF3_137 is the one of the highest between the simulation results ($\gamma = 22.1$ mN/m), the highest among the experimental data ($\gamma = 24.8$ mN/m), because it has the lower percentage of fluorine atoms on the surface (7%).

The fluorinated trifluoroacetophenone with terphenyl (CF3_138) has a contact angle of 95.5°, even though its relative polar surface is the highest (0.28), due to the fluorine atoms on the aromatic ring that increase the electronegativity of the molecule. However, the hydrophobic character of the structure is confirmed also by the high AlogP (9.84) and the low binding energy (-30.49 kcal/mol). As a consequence, the

fluorinated aromatic rings may arrange themselves inside, exposing to the interface only the trifluoromethyl groups.

It is worth to note that for CF3_140, CF3_137, CF3_138 the predominant forces in the binding energies are the Coulomb forces, due to the presence of the polar groups as carbonyl, amine and pentafluoroacetophenone groups. On the other hand, in the CF3_74, CF3_140, CF3_277 and CF3_279, the predominant forces in the binding energies are the van der Waals forces.

4.4 Conclusions

In this work we developed two, alternative atomistic MD simulation-based computational protocols to estimate the contact angle θ , the surface and interface tensions γ , and the work of adhesion W_{adh} for water, oil, and mixtures of fluids (i.e., surfactant/water solution) in contact with amorphous polymer surface of different nature. Both methodologies yielded reliable values of the contact angles and surface tensions, in agreement with available experimental data. Moreover, reasonable and comparable values of W_{adh} (a quantity affected by large errors during experimental determination), were also obtained using both computational recipes, thus confirming the internal consistency in the presented methodologies. Currently, further and highly encouraging work is in progress to expand this computer-based ansatz to the study of liquid spreading onto surfaces of different nature (e.g., crystalline and non-polymeric), and to the inclusion of different effects such as temperature, droplet size, and surface roughness.

4.5 References

- [1] a) Gao, L.; McCarthy, T. J. *Langmuir* 2009, 25, 14105–14115; b) Samsonov, V. M. *Curr. Op. Colloid Interface Sci.* 2011, 16, 303-309.
- [2] Dee, G. T.; Sauer, B. B. *J. Colloid Interface Sci.* 1992, 152, 85-103.
- [3] G. Chatterjee, S. Prasad, *Polystyrene: Properties, Performance and Applications*, Nova Science Publishers, New York, 2011.
- [4] a) E. Kontturi, M. Suchy, P. Penttilä, B. Jean, K. Pirkkalainen, M. Torkkeli, R. Serimaa, *Biomacromolecules* 2011, 12, 770-777; b) C. H. Stephens, P. M. Whitmore, H. R. Morris, M. E. Bier, *Biomacromolecules* 2008, 9, 1093-1099; c) S. Gunnars, L. Wågberg, M. A. Cohen Stuart, *Cellulose* 2002, 9, 239-249.
- [5] Lovinger, A. J. *DeVelopment in Crystalline Polymers*; Applied Science: London, 1982; Vol.1

- [6] a) Garbassi, F.; Morra, M.; Occhiello, E. *Polymer Surfaces: From Physics to Technology*; Wiley: Chichester, U.K., **1994**) Tsuruta, T.; Hayashi, T.; Kataoka, K.; Ishihara, K.; Kimura, Y. *Biomedical Applications of Polymeric Materials*; CRC: Boca Raton, FL, **1993** c) Lee, S.; Knaebel, K. S. *J. Appl. Polym. Sci.* **1997**, *64*, 455 d) Lee, S.; Knaebel, K. S. *J. Appl. Polym. Sci.* **1997**, *64*, 477
- [7] Lee, S.; Park J.S.; and Randall Lee T. *Langmuir* **2008**, *24*, 4817-4826
- [8] R. Souzy, B. Ameduri*, B. Boutevin *Prog. Polym. Sci.* **29** **2004** 75–106
- [9] a) R.D. Miller, *Science* **286** (5439) **1999**, 421 b) G. Maier, *Prog. Polym. Sci.* **26** **2001**, 3 c) T.M. Long, T.M. Swager, *J. Am. Chem. Sci.* **125** **2003**, 14113 d) B.J. Liu, G.B. Wang, W. Hu, Y.H. Jin, C.H. Chen, Z.H. Jiang, W.J. Zhang, Z.W. Wu, Y. Wei, *J. Polym. Sci. Part A: Polym. Chem.* **40** **2002**, 3392
- [10] a) R.H. Vora, P.S.G. Krishnan, S.H. Goh, T.S. Chung, *Adv. Funct. Mater.* **11** (5) **2001**, 361 b) V. Kute, S. Banerjee, *Macromol. Chem. Phys.* **204** **2003**, 2105–2112.
- [11] Stamm M. *AdvPolymSci* **1992**;100:357
- [12] a) Karasawa, N.; Goddard, W. A. *Macromolecules* **1995**, *28*, 6765 b) Karasawa, N.; Goddard, W. A. *Macromolecules* **1992**, *25*, 7268 c) Richard H. Gee, Laurence E. Fried, and Robert C. Cook *Macromolecules* **2001**, *34*, 3050-3059 d) Sanghun Lee, Jaeon Chang, Richard L. Jaffe, and Do Y. Yoon *Macromolecules* **2007**, *40*, 7407-7412
- [13] a) Richard H. Gee, Amitesh Maiti, Sorin Bastea, and Laurence E. Fried *Macromolecules* **2007**, *40*, 3422-3428 b) B. Prathab, Tejraj M. Aminabhavi, R. Parthasarathi, P. Manikandan, V. Subramanian *Polymer* **47** **2006**, 6914-6924
- [14] H. J. C. Berendsen, J. R. Grigera, T. P. Straatsma, *J. Phys. Chem.* **1987**, *91*, 6269-6271.
- [15] M. B. Plazzer, D. J. Henry, G. Yiapanis, I. Yarovsky, *J. Phys. Chem. B* **2011**, *115*, 3964-3971.
- [16] D. Rigby, *Fluid Phase Equilib.* **2004**, *217*, 77-87.
- [17] H. Heinz, R. A. Vaia, B. L. Farmer, R. R. Naik, *J. Phys. Chem. C* **2008**, *112*, 17281-17290.
- [18] W.-J. Lee, S.-P. Ju, *Langmuir* **2009**, *26*, 438-446.
- [19] a) H. Sun, *J. Comput. Chem.* **1994**, *15*, 752-768; b) H. Sun, *J. Phys. Chem. B* **1998**, *102*, 7338-7364; c) H. Sun, P. Ren, J. R. Fried, *Comput. Theor. Polym. Sci.* **1998**, *8*, 229-246; d) J. Yang, Y. Ren, A.-m. Tian, H. Sun, *J. Phys. Chem. B* **2000**, *104*, 4951-4957; e) S. W. Bunte, H. Sun, *J. Phys. Chem. B* **2000**, *104*, 2477-2489; f) M. J. McQuaid, H. Sun, D. Rigby, *J. Comput. Chem.* **2004**, *25*, 61-71.
- [20] H. J. C. Berendsen, J. P. M. Postma, W. F. van Gunsteren, A. Di Nola, J. R. Haak, *J. Chem. Phys.* **1984**, *81*, 3684-3690.
- [21] E. Manias, V. Kuppa, *Eur. Phys. J. E* **2002**, *8*, 193-199.
- [22] M. Fermeglia, S. Pricl, *AIChE J.* **1999**, *45*, 2619-2627.
- [23] D. N. Theodorou, U. W. Suter, *Macromolecules* **1986**, *19*, 139-154.
- [24] C. F. Fan, T. Çağın, *J. Chem. Phys.* **1995**, *103*, 9053-9061.
- [25] R. Toth, A. Coslanich, M. Ferrone, M. Fermeglia, S. Pricl, S. Miertus, E. Chiellini, *Polymer* **2004**, *45*, 8075-8083.
- [26] R. Toth, D.-J. Voorn, J.-W. Handgraaf, J. G. E. M. Fraaije, M. Fermeglia, S. Pricl, P. Posocco, *Macromolecules* **2009**, *42*, 8260-8270.
- [27] A. Dupré, *Théorie Mécanique de la Chaleur*, Gauthier-Villars, Paris, **1869**.
- [28] T. A. Andrea, W. C. Swope, H. C. Andersen, *J. Chem. Phys.* **1983**, *79*, 4576-4584.
- [29] a) K. F. Mansfield, D. N. Theodorou, *Macromolecules* **1990**, *23*, 4430-4445; b) K. F. Mansfield, D. N. Theodorou, *Macromolecules* **1991**, *24*, 6283-6294.
- [30] M. Connolly, *Science* **1983**, *221*, 709-713; b) M. Connolly, *J. Appl. Crystallogr.* **1983**, *16*, 548-558; c) M. L. Connolly, *J. Am. Chem. Soc.* **1985**, *107*, 1118-1124.
- [31] a) B. Lee, F. M. Richards, *J. Mol. Biol.* **1971**, *55*, 379-IN374; b) F. M. Richards, *Annual Review of Biophysics and Bioengineering* **1977**, *6*, 151-176.
- [32] C. Li, P. Choi, *J. Phys. Chem. B* **2006**, *110*, 6864-6870.
- [33] W.-K. Kim, W. L. Mattice, *Langmuir* **1998**, *14*, 6588-6593.

- [34] H. Heinz, R. A. Vaia, B. L. Farmer, R. R. Naik, *Journal of Physical Chemistry C***2008**, 112, 17281-17290.
- [35] D. R. Lide, *CRC Handbook of Chemistry and Physics*; 84th ed., Boca-Raton, **2003**.
- [36] T. C. Clancy, W. L. Mattice, *Comput. Theor. Polym. Sci.***1999**, 9, 261-270.
- [37] M. E. Schrader, *Langmuir***1995**, 11, 3585-3589.
- [38] S. Wu, *Journal of Polymer Science Part C: Polymer Symposia* 1971, 34, 19-30.
- [39] K. e. a. Gotoh, *Polymer Surface Modification: Relevance to Adhesion*, ed., VSP, The Netherlands, **2000**.
- [40] C. Aulin, S. Ahola, P. Josefsson, T. Nishino, Y. Hirose, M. Osterberg, L. Wågberg, *Langmuir***2009**, 25, 7675-7685.
- [41] E. G. Shafrin, *Polymer Handbook*, 2nd Ed., Vol. III, Wiley-Interscience, New York.
- [42] E. G. Shafrin, W. A. Zisman, *Upper Limits for the Contact Angles of Liquids on Solids* **1963**.
- [43] H. Y. Erbil, R. A. Meric, *J. Phys. Chem. B***1997**, 101, 6867-6873.
- [44] C. Vega, E. de Miguel, *J. Chem. Phys.* **2007**, 126, 154707-154710.
- [45] L. D. A. Chumplitaz, L. F. Coutinho, A. J. A. Meirelles, *JAOCs***1999**, 76, 379-382
- [46] G. J. Gloor, G. Jackson, F. J. Blas, E. de Miguel, *J. Chem. Phys.***2005**, 123,
- [47] a) R. H. Gee, A. Maiti, S. Bastea, and L. E. Fried *Macromolecules***2007**, 40, 3422-3428 b) R. H. Gee, L. E. Fried, and R. C. Cook *Macromolecules***2001**, 34, 3050-3059 c) Prathab, T. M. Aminabhavi, R. Parthasarathi, P. Manikandan, V. Subramanian *Polymer* **47** **2006**, 6914-6924
- [48] Sun, T.; Song, W.; Jiang, L. *Chem. Commun.* **2005**, 1723-1725
- [49] Nishino, T.; Meguro, M.; Nakamae, K.; Matsushita, M.; Ueda, Y. *Langmuir***1999**, 15, 4321-4323
- [50] Richards, F. M. *Annu. Rev. Biophys.***1977**, 6, 151
- [51] Mandelbrot, B. B. *The Fractal Geometry of Nature*; Freeman: San Francisco, **1983**
- [52] Priel, S.; Fermeglia, M. *Carbohydr. Polym.* **2001**, 45, 23-33
- [53] Priel, S.; Fermeglia, M.; Ferrone, M.; Asquini, A. *Carbon***2003**, 41, 2269-2283
- [54] Metullio, L.; Ferrone, M.; Coslanich, A.; Fuchs, S.; Fermeglia, M.; Paneni, M. S.; Priel, S. *Biomacromolecules***2004**, 5, 1371-1378
- [55] Connolly, M. L. *J. Appl. Crystallogr.* **1983**, 16, 548-558
- [56] Connolly, M. L. *Science***1983**, 221, 709-713
- [57] Connolly, M. L. *J. Am. Chem. Soc.***1985**, 107, 1118-1124
- [58] J. F. Douglas *Macromolecules***1989**, 22, 3707-3716
- [59] Ghose, A. K.; Crippen, G. M., *J. Comput. Chem.* **1986**, 4, 565.
- [60] Ghose, A. K.; Crippen, G. M., *J. Chem. Inf. Comput. Sci.***1987**, 27,21.
- [61] Ghose, A.; Pritchett, A.; Crippen, G. M. *J. Comput. Chem.***1988**, 9, 80.
- [62] Viswanadhan, V.; Ghose, A. K.; Revankar, G. R.; Robins, R. K., *J. Chem. Inf. Comput. Sci.***1989**, 29, 163-72.
- [63] Ghose, A. K.; Viswanadhan, V.; Wendoloski, J. J., *J. Phys. Chem. B***1998**, 102, 3762.
- [64] Ghose, A. K.; Crippen, G. M., *J. Comput. Chem.* **1986**, 4, 565.
- [65] Ghose, A. K.; Crippen, G. M., *J. Chem. Inf. Comput. Sci.***1987**, 27,21.
- [66] Ghose, A.; Pritchett, A.; Crippen, G. M. *J. Comput. Chem.* **1988**, 9, 80.
- [67] Viswanadhan, V.; Ghose, A. K.; Revankar, G. R.; Robins, R. K., *J. Chem. Inf. Comput. Sci.***1989**, 29, 163-72.
- [68] Ghose, A. K.; Viswanadhan, V.; Wendoloski, J. J., *J. Phys. Chem. B***1998**, 102, 3762.

5

Characterization of polymer-grafted silica-based polymer nanocomposites

Spherical nanoparticles (NPs) with polymer brush surfaces in a melt of homopolymer chains not only are an important system for technical applications, but also provide a very important model system in the field of soft colloidal particles. To yield the desired superior performances, however, these polymer-grafted NPs must be well dispersed in the polymer matrix, and it is therefore unfortunate that long melt chains have the general tendency of destabilizing the colloidal dispersions. This phenomenon is strongly related to the wetting autophobicity of a polymer melt on top of a chemically identical, polymer brush. So far, a systematic investigation of the wetting behavior of melt-grafted-NP brush systems, in which experimental observations are

paralleled and tightly coupled to multiscale molecular simulations, and paying attention to all key variables such as NP grafting density, grafting chain length, and volume fraction, has not been carried out.

Thus in this work we want to study the dispersion/aggregation mechanism of nanocomposites made of well-defined polymer (polystyrene) grafted-NPs (silica) mixed with free chains of the same polymer using a combination of scattering (SAXS and SANS), imaging (TEM), and multiscale molecular simulation techniques.

Part of this work is published in P. Posocco, F. Santese M. Meyer, E. Hübner, O. Pravaz, J.W. Handgraaf, W. Pyckhout-Hintzen, D. Richter, M. Fermeglia, and Sabrina Pricl *RSC Advances*, **2013** submitted.

5.1 Introduction

In our days, colloidal filler material in polymers have a great tradition and applied in many fields of our daily life. The addition of inorganic particles can generate an almost infinite variety of materials with unique physical properties. The best known example is the application of micron-sized carbon black or silica particles (SiO_2) for a reinforcement in tires. These effects of classical micro-composites were studied on macroscopic as well as microscopic length scales within the last decades and are well understood by now^[1].

In recent years, the further development in chemistry allowed the synthesis of now nanometer-sized particles, which lead to a new class of nanocomposites. These nanocomposites are characterized by an enormous increase of the particle-polymer interface, i.e. surface-to-volume ratio of the fillers, which is supposed to alter the polymeric properties in a similarly enormous way. However, several experimental observations are contradictory to the behavior predicted for classical composites. Tuteja et al.^[2], for example, showed an unexpected decrease in the viscosity of polystyrene in op position to the Stokes-Einstein relation. The origin of this and other discrepancies between conventional and nano-composites is of highest scientific, but also industrial, interest and still not known.

The colloidal distribution of nanoparticles in the melt is not trivial, since weak forces, such as van-der-Waals, play a significant role on the spatial distribution of nano-sized objects^[3]. A special class of nano-fillers

are surface modified nanoparticles, which are grafted with polymers. These polymer chains are covalently bond onto the surface of the particles, mediating an interaction between the blend and the particles. The so-formed inter-phase between the tethered and matrix polymers is important for an optimal compatibility of filler and blend material^[4].

The focus of this work is the structural characterization of the polymeric corona formed by atactic polystyrene tethered onto the surface of silica nanoparticles. The influence of the grafting density, i.e. the number of chains per particle, as well as of the molecular weight of the graft on the microscopic structure is investigated. Small angle neutron scattering (SANS) offers the possibility to study the static properties of these grafted nanoparticles and is combined with other complementary methods like transmission electron microscopy (TEM) and small angle X-ray scattering (SAXS).

Within this project, multi-scale simulation and experimental techniques were combined to investigate the relation between the macroscopic properties and the microscopic structure of nanocomposites, basing on model systems of polystyrene grafted nanoparticles dispersed in a polystyrene melt. The microscopic information on the conformation of matrix and grafted polymer chains evaluated in this thesis were provided to the partners for the important verification and validation of the various simulations methods.

5.2 Materials and methods

Silica nanoparticles (NPs) ($D = 10\text{-}15$ nm, manufacture's data) were obtained as 30 wt % solution in *n*-butyl acetate (NBAC-St) from Nissan Chemical Industries and used as received. To achieve an high grafting density, in this work a new "grafting to" technique proposed by Hübner et al.^[5] was employed for the functionalization of silica nanoparticles using anionic polymerization. Briefly, it is based on a two steps method. First, the silica particles were modified with dimethylchlorosilanes. This procedure replaces the original Si-OH surface groups by Si-Cl functionalities (see Figure 5.1). Then, previously anionically synthesized PS polymer chains were linked to the nanoparticle. After synthesis, the free polymer was separated from the functionalized NPs by fractionation with toluene/methanol. The upper concentration limit for an optimal

separation was found at a concentration of 0.4% wt of the crude mixture in toluene. Subsequent addition of methanol until precipitation starts at temperature of 36-37°C and slow cooling of the solution lead to precipitation of the nanoparticles while the free polymer remains in solution.

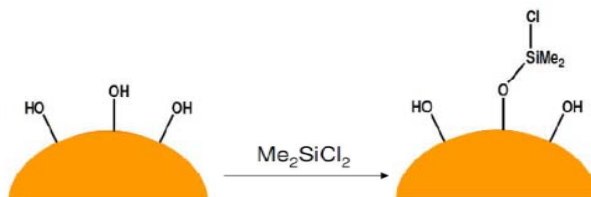


Figure 5.1: Functionalization of silica with a linking group for living anionic polymer.

The polymer content of the synthesized particles was determined by elemental analysis (EA) and corrected for remaining fractions of ungrafted polymer and free solvent in the samples, determined by size exclusion chromatography (SEC), small angle light scattering (SALS), and nuclear magnetic resonance (NMR). The average number of grafted chains per particle, $\langle f \rangle$, was derived using the molecular weight of the polymer, known from SEC. Table 5.1 summarizes the grafted particles synthesized and reports selected properties, such as number average molecular weight M_n , polydispersity index PDI , and number of grafted chains $\langle f \rangle$.

System	M_n (KDa)	PDI (M_w/M_n)	$\langle f \rangle$ (-)
A	2.00	1.08	356 ± 32
B	9.77	1.02	279 ± 24
C	9.99	1.02	389 ± 34
D	20.61	1.07	224 ± 20
E	20.67	1.11	632 ± 67
F	103.5	1.02	370 ± 34

Table 5.1: List of the synthesized grafted nanoparticles with selected properties.

A summary of the nanocomposites prepared and investigated in this work is reported in Table 5.2. All nanoparticles were dispersed in a PS matrix of approximately 94 kDa molecular weight.

System	NP ^a	M _n (KDa)	σ (chains/nm ²)	c ^b (% vol)	P/N ^c
1	A	2.00	0.51 ± 0.03	0.25	4.7
2	B	9.77	0.40 ± 0.03	0.25	9.6
3	C	9.99	0.55 ± 0.05	0.25	9.4
4	D	20.61	0.32 ± 0.03	0.25	4.6
5	E	20.67	0.90 ± 0.10	0.25	4.5
6	D	20.61	0.32 ± 0.03	5.0	4.6
7	E	20.67	0.90 ± 0.10	5.0	4.5
8	F	103.5	0.53 ± 0.05	0.25	0.9

Table 5.2: Nanocomposites studied in this work. ^aType of nanoparticle, labelling according to Table 5.1; ^bNanoparticle concentration (volume percent of NP); ^cMolecular weight ratio, where P and N are the free and graft molecular weights, respectively.

5.2.1 SANS experiments

Small angle neutron scattering (SANS) measurements were carried out at the instruments KWS-1 and KWS-2 at the research reactor FRM II, Julich Centre for Neutron Science @ Garching, Germany. The neutron wavelength was $\lambda = 7\text{\AA}$ with a wavelength resolution $\Delta\lambda/\lambda = 0.1$ for KWS-1 and $\lambda = 4.5\text{\AA}$ with $\Delta\lambda/\lambda = 0.2$ for KWS -2 respectively. Scattering intensities were measured over a scattering range from 0.002 to 0.2 \AA^{-1} (0.008 to 0.3 \AA^{-1} , KWS-2) using sample-to-detector distances of $L = 2$ m, 8 m and 20 m ($L = 2$ m and 8m, KWS-2). Accordingly, size determinations of approx. 5 to 500 \AA ($1/q$) are allowed. For $L = 2$ m and 8 m a collimation length of $l = 8$ m was used, whereas for $L = 20$ m the collimation length was $l = 20$ m. Measurements were carried out at 25 °C. Scattering from the samples was corrected for sensitivity and dark current of the detector and empty beam. The scattered intensities were calibrated to absolute unit (cm^{-1}) using a PMMA secondary standard.

5.2.2 SAXS experiments

Small-angle X-ray scattering (SAXS) measurements were performed at the Swiss Light Source (Paul Scherrer Institute, Villigen, Switzerland) on the cSAXS beamline with 11.2 keV X-rays (corresponding to a wavelength of $\lambda = 0.111$ nm) and a sample-detector distance of 8 meters. Nanocomposites were cast in thin films and PS matrix film was measured separately and subtracted from the data. Two-dimensional SAXS patterns

were radially averaged and the resulting scattering curves were fitted using the software SASFIT.^[6]

5.2.3 Transmission electronic microscopy

Polymeric samples were ultramicrotomed at room temperature using a Diatome diamond knife on a Reichert-Jung UltraCut E Microtome to give 80 nm thick sections, which are then transferred onto 600-mesh copper grids for transmission electron microscopy (TEM) imaging. TEM was performed on a Philips CM100-Biotwin operated at 80 keV.

5.2.4 Computational details

In this work we proposed a multiscale modeling approach to predict aggregation/dispersion behavior of PS-grafted silica nanoparticles. This procedure couples atomistic and mesoscale simulations through three distinctive steps: i) 3D atomistic simulation of representative planar PS-modified silica/PS interfaces are employed to derived interaction energies among each system component; ii) mesoscale simulation of the planar silica/polymer interface, as a function of grafting density and length of the grafted chains, are performed to predict mesoscale interaction parameters (namely, first level of coarse-graining); iii) each grafted chain was then lumped in a simplified icosahedral nanosphere, and nanoparticles were embedded in the polymer melt at different loadings (second level of coarse-graining) to investigate dispersion/aggregation mechanisms.

5.2.4.1 Atomistic simulation

Silica surface model

The amorphous bulk silica ($30.1\text{\AA} \times 30.1\text{\AA} \times 30.1\text{\AA}$) with a density of 2.2 g/cm^3 was obtained by a well-established melt-quench molecular dynamics (MD) simulation technique^[7,8,9] starting from a crystalline α -quartz model^[10]. The procedure consisted in:^[11] i) MD heating of the crystalline model at 8000 K to melt the sample and remove crystal memory; ii) 100 ps of MD equilibration at a density of 2.2 g/cm^3 ; iii) continuous MD cooling to 300 K in 1540 ps (cooling rate = 5 K/ps) under NVT periodic boundary conditions; iv) final 350 ps MD equilibration at

300 K (Nosé-Hoover thermostat with $\tau = 0.1$ ps) using the leapfrog Verlet integration algorithm with integration step $\Delta t = 2$ fs. The COMPASS force field,^[12] which has been previously employed successfully to model polymer and organic-inorganic systems, including silica-organic interface properties,^[13,14,15] was chosen to model the energy of all systems, including silica. The Ewald summation method was used for treating both van der Waals and electrostatic interactions.

The surface model of amorphous silica was then obtained from the bulk model by: i) slicing the amorphous SiO₂ bulk model in the Y-direction and taking the lower part of the bulk taken as the surface; eventual uncoordinated Si atoms were saturated with O atoms. All surface oxygen atoms were saturated with hydrogen; ii) inserting 50 Å vacuum gap at the top in the Y-direction; iii) relaxing the system at 2000K with 20ps NVT MD and 80 ps NVE MD; iv) cooling to 300K in 340 ps (cooling rate = 5 K/ps) and equilibrating the system for 20 ps. The resulting slab had a thickness of 19 Å.

Polymer model

A representative PS chain with a polymerization degree of 96 was considered to model the atactic and amorphous PS matrix at the atomistic level. The initial conformations of the PS molecule at T= 448K were obtained using the rotational isomeric state (RIS) algorithm, as modified by Theodorou and Suter,^[16] and following our well-validated combined molecular mechanics/molecular dynamics simulated annealing (MDSA) protocol.^[17,18,19] In order to obtain a reasonable sampling of the polymer conformational space, we built and energy minimized 5 different PS configurations.

To validate the molecular models of the PS chains and the use of the COMPASS FF, we simulated the PVT behavior of the DP=96 PS systems and compared the results with the available experimental data. The employed molecular dynamics (MD) procedure to obtain the PVT behavior was the following: i) each simulation cell was built at 527 K. 5 conformations for each PS chain were prepared to have enough data for statistical significance; ii) each cell was equilibrated at 527 K and 10 MPa for 10-20 ns using NPT MD, using the leapfrog Verlet integration algorithm ($\Delta t = 4$ fs) and the Berendsen thermostat ($\tau_T = 0.5$ ps, $\tau_p = 1$ ps); iii)

after equilibration, the pressure value P was adjusted to reproduce the actual density value; iv) after compression, P was fixed and more MD equilibration steps were performed (5-10 ns); v) each systems was then cooled down in almost-stationary stepwise procedure ($\Delta T = 20\text{K}$) (cooling rate = 50 K/ns). All results were expressed as average values of the 5 system conformations.

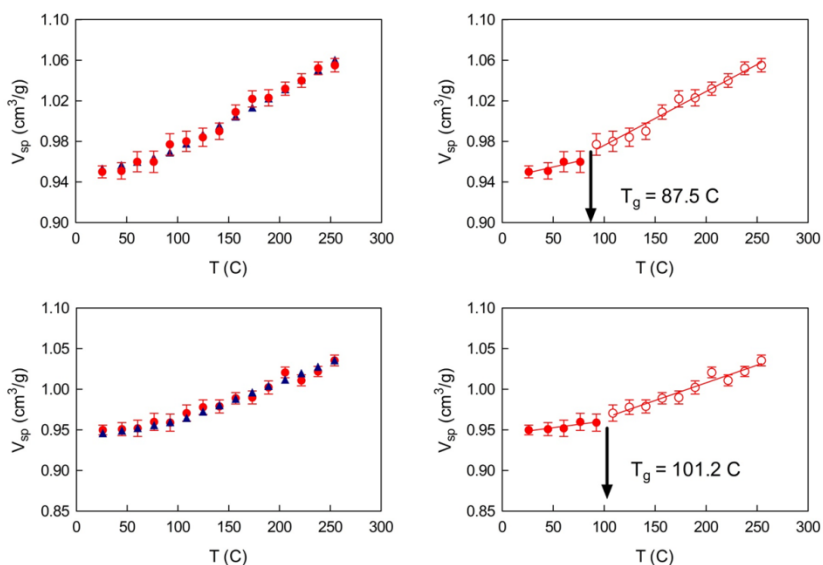
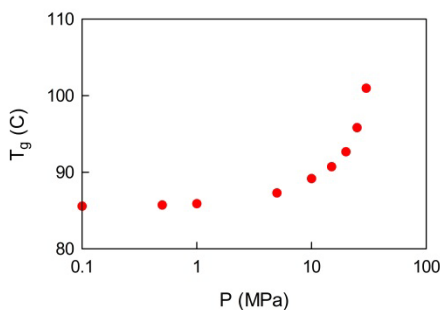


Figure 5.2: Simulated (red) and experimental (blue) specific volume for PS 10kDa at 5 MPa (top row) and 30 MPa (bottom row). The corresponding T_g were estimated from the point of inflection in the PVT curves.



P (MPa)	T_g^{calc} (°C)	T_g^{exp} (°C)
5	87.5	87.9
10	88.8	89.2
15	91.2	90.7
20	93.9	92.7

25	95.8	104.2
30	102.2	101.0

P (MPa)	T_g^{calc} (°C)
1	85.9
0.5	85.7
0.1	85.6

Figure 5.3: Simulated glass temperature T_g as a function of pressure P for PS (graph) and comparison with experimental values (tables).

Grafted PS model

We first modeled the silane moiety which connects the bare SiO₂ surface to the PS grafted chains. After being sketched, the geometry of the silane molecule was optimized using the COMPASS force field. The molecule conformational search was carried out using a MDSA^[17,18,19] protocol, in which the relaxed molecular structure was subjected to five repeated temperature cycles using NVT MD conditions. At the end of each annealing cycle, the structure was again energy minimized, and only the structure corresponding to the minimum energy was used for further modeling. The electrostatic charges for the geometrically optimized silane molecule was finally obtained by restrained electrostatic potential fitting, and electrostatic potentials were produced by single-point quantum mechanical calculations at the Hartree–Fock level with a 6-31 G* basis set.

A suitable number of silane molecules were then randomly placed onto the SiO₂ surface to reproduce an average grafting density of 0.32 chains/nm² and reacted with the correct number of O atoms. A PS chain of a representative length of 19 monomers obtained through the MDS^[17,18,19] protocol was then chemically linked to each silane linker.

Ternary model system

Once the modified silica surface models were constructed, a free PS polymer chain was added copying one of the 5 configurations extracted from the corresponding equilibrated MD simulations in 5 different cells, thus obtaining 5 different model systems.

Resorting to atomistic MD simulations in the NVT ensemble allows retrieving important information on the interaction and binding energy values between the different components of a multicomponent system,^{[18-}

^{23]} such as PS-grafted SiO₂ nanoparticle immersed in a PS matrix. The technique we developed to this purpose basically consists in simulating the interface between the modified nanoparticle and the polymer by building a cell that is “stretched” along the *c*-direction (up to 150 Å); in this way, even if the model is still 3-D periodic, there are no interactions between the periodic images in the *c*-direction, ultimately resulting in a pseudo 2-D periodic system, from which the binding energies between all system components can be calculated.

Minimization and NVT simulations were then performed using the Compass FF. During each MD, the SiO₂ atoms were treated as rigid bodies by fixing all cell dimensions. All other atoms were allowed to move without any constraint. Each NVT simulation was run at 448K for 100ns, applying the Ewald summation method for treating both van der Waals and electrostatic interactions. An integration time step of 1fs, and the Nosé thermostat (Q ratio = 1) were also adopted.

From the equilibrated part of the MD trajectory of each system, the interaction energies among all system components were extracted according to a well-validated procedure.^[17-20,24,25] Since, by definition, the binding energy (E_{bind}) between each generic pair of components A and B is the negative of the corresponding interaction energy, each E_{bind} term can be simply obtained from the corresponding interaction energies as:^[17-20,24,25]

$$E_{bind}^{A/B} = E_A + E_B - E_{A/B} \quad (5.1)$$

Data collected have then been averaged over the 5 different model systems to ensure statistical meaning of the values.

All atomistic simulations were run using *Materials Studio* package.

5.2.4.2 Mesoscale simulation

First level of coarse-graining (CG-I)

In order to simulate the morphology of the silica-based nanocomposite systems at a mesoscopic level, we employed the dissipative particle dynamics (DPD)^[26] simulation tool as implemented in the *Culgi*^[27] modelling suite. In the framework of a multiscale approach, the interaction parameters needed as input for the mesoscale level DPD

calculations have been obtained by a mapping procedure of the binding energy values between different species obtained from simulations at a lower (atomistic) scale using our procedure.^[17-19,28] The DPD nanocomposite model contains four species of different beads or mesoscale units: one for the free polymer chain (P_M) and two for the grafted PS chain-linker moiety (one for the linker silane moiety (L), and one for the PS tail (P_L)). The last one is for the silica surface (S).

Starting mesoscale model generation with the free polymer chain, we mapped the real polymer chain onto a chain consisting of Kuhn segments. Consequently, each DPD bead represents a statistically correlated unit or Kuhn segment of the polymer. A DPD chain should, therefore, be made up of N_{DPD} beads, where $N_{DPD}=N_{mon}/C_\infty$ and N_{mon} is equal to the degree of polymerization of the molecular chain and C_∞ is its characteristic ratio. If so, the mesoscale simulations should capture in a reliable way two essential features of a given polymer chain, namely its dimension (given by N_{mon}) and flexibility (given by C_∞). C_∞ is an intrinsic property of the chain, and in the developed recipe was estimated using a molecular dynamics procedure based on the RIS method. According to our recipe,^[29] a given number of different chain configurations at a fixed number of monomers N_{mon} – say C_1, C_2, C_3 – are generated via rotational isomeric state (RIS) algorithm^[16]. Each C_i then undergoes independent cycles of molecular mechanics minimization and simulated annealing procedures before running productive constant volume-constant temperature (NVT) MD simulations. After the simulation is done, the end-to-end distance of the chains is estimated, and the C_∞ is calculated. The procedure is repeated, for each configuration at different chain length N_{mon} , until a constant value of C_∞ is obtained. The final value of C_∞ is estimated by averaging over all the configurations considered. Figure 5.2 below illustrates the procedure described above to calculate the C_∞ value for PS as applied to PS chains of molecular mass from 0.5 to 60 kDa.

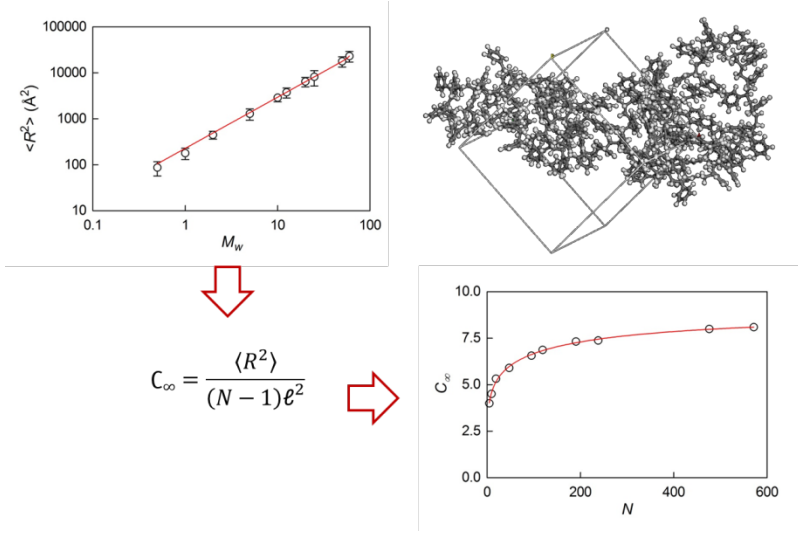


Figure 5.4: Illustration of the RIS-based procedure to obtain the value of C_∞ for a PS chain. $\langle R^2 \rangle$ is the average square end-to end distance of the chain, N is the degree of polymerization of the chain, and ℓ is the monomer length.

Following this methodology, a value of 7.3 was predicted for a PS of 100 kDa, as corrected for its temperature dependence. Accordingly, our PS free chain is constituted by a number of 131 N_{DPD} .

The modeling of the silica surface in the context of DPD has been addressed by freezing locally the particles representing the silica solid boundaries. These particles behave as fluid particles but maintain a fixed position and possess zero velocity. Therefore, they interact with each bead in the system with a potential of the same form as the bead-bead conservative force.^[19]

System	M_n [kg/mol]	f	N_L^a	N_{PL}^b	t_{av}^{calc} [Å]	t_{av}^{exp} [Å]
A	2.00	57	1	4	46 ± 8	-
B	9.77	45	1	12	66 ± 8	76 ± 7
C	9.99	62	1	12	85 ± 6	99 ± 10
D	20.61	36	1	25	108 ± 4	109 ± 13
E	20.67	101	1	22	158 ± 8	170 ± 17
F	103.5	60	1	133	336 ± 11	347 ± 34

Table 5.3: CG-I model of each grafted chain studied in this work. ^aNumber of beads of type L ; ^bNumber of beads of type PL ; ^cAverage brush height calculated from DPD simulation; ^dAverage brush height as derived from our SANS experiments.

Each PS grafted chain mesoscale model was derived matching the DPD average brush height with the average brush height predicted by

SANS experiments. An initial guess of groups of atoms that should encompass the soft-core beads was made for each grafted length considered in this work. Then, a suitable number of chains were randomly placed on the top of a silica slab of approximately 10.6 nm in order to reproduce the same grafted density as reported in Table 5.1 for each system. Also in this case, the interface between the modified silica surface and the polymer was simulated by building a cell that is “stretched” along the *c*-direction (up to 150 Å). The average brush height was calculated after 5×10^6 steps (a dimensional time step $\Delta t = 0.01$) of DPD dynamics and compared to the value extracted from SANS analysis. If they do not match, we varied the bead number (i.e. the number of beads *S* and *P_L*) of the chain. In the final step we went back to the assignment of the atoms to the molecular fragments and optimized these as well by swapping, if needed, atoms between the molecular fragments. In this way we found that intramolecular size of an atomistically detailed model of a grafted PS molecule has an optimal mapping if its coarse-grained chain model has the structure reported in Table 5.3.

The bead-bead interaction parameter for the matrix PS-matrix PS interaction was set equal to $a_{PMPM} = 19.6$ taking into account the PS compressibility [26c,30,31] and in the hypothesis of an adimensional density value $\rho = 3$ [26c]. For the pair S/L the parameter a_{ij} was set it to the value of 5 in order to reproduce the covalent S/L interaction. Having fixed these two parameters, their values were then associated to the corresponding values of the DPD energies rescaled from MD simulations. All the remaining DPD interaction parameters a_{ij} could then easily be derived following this criterion.[17-19,28] In the case of silica/silica interaction, since no energy values could be extracted from the MD simulations, we set $a_{SS} = 15$. The final sets of DPD parameters, obtained from the scaling procedure starting from atomistic MD simulation energies are listed in Table 5.4.

We adopted in all simulations the standard DPD units, where r_c is a unit of length, $k_B T$ is a unit of energy and bead mass is a unit of mass. A value of the spring constant of $4k_B T$ was used for all the chains.

<i>A</i>	<i>S</i>	<i>L</i>	<i>P_L</i>	<i>P_M</i>	<i>B</i>	<i>S</i>	<i>L</i>	<i>P_L</i>	<i>P_M</i>
<i>S</i>	15				<i>S</i>	15			
<i>L</i>	5	24.8			<i>L</i>	5	24.8		
<i>P_L</i>	30.9	30.6	25.6		<i>P_L</i>	31.3	31.2	28.9	
<i>P_M</i>	28.3	28.1	26.2	19.6	<i>P_M</i>	29.4	29.2	27.4	19.6

<i>C</i>	<i>S</i>	<i>L</i>	<i>P_L</i>	<i>P_M</i>	<i>D</i>	<i>S</i>	<i>L</i>	<i>P_L</i>	<i>P_M</i>
<i>S</i>	15				<i>S</i>	15			
<i>L</i>	5	24.9			<i>L</i>	5	25.0		
<i>P_L</i>	31.3	31.4	29.1		<i>P_L</i>	33.6	32.3	30.3	
<i>P_M</i>	29.6	29.4	27.2	19.6	<i>P_M</i>	30.6	30.2	28.6	19.6

<i>E</i>	<i>S</i>	<i>L</i>	<i>P_L</i>	<i>P_M</i>	<i>F</i>	<i>S</i>	<i>L</i>	<i>P_L</i>	<i>P_M</i>
<i>S</i>	15				<i>S</i>	15			
<i>L</i>	5	24.9			<i>L</i>	5	24.9		
<i>P_L</i>	33.1	32.4	31.8		<i>P_L</i>	37.2	35.4	32.9	
<i>P_M</i>	31.9	31.5	29.3	19.6	<i>P_M</i>	32.6	32.8	31.2	19.6

Table 5.4: DPD-CG-I parameters for the PS-linker-modified silica/PS matrix nanocomposites as obtained from the developed multiscale molecular model.

Second level of coarse-graining (CG-II)

Dispersion/aggregation of nanoparticles in polymer melts at both low and high filler contents involves dozen of nanoparticles. The last step of our multiscale procedure consists in a further coarse-graining step, involving the lumping of the solid nanoparticle and its relevant grafted chains into one single nano-object. To this purpose, we adopted the following methodology. Each DPD grafted silica nanoparticle is modeled by a rigid icosahedral structure,^[29,32] devised as being constituted by a central DPD bead, connected to 12 other DPD beads on each vertex of the icosahedrons. Each vertex of the icosahedron represents either a bare silica portion or a lumped PS-L grafted chain. According to this model, different length of the grafted PS-L chains can be modulated by averaging the contribution of the corresponding a_{ij} parameters of all beads making up the PS-L chain in a new, hybrid bead H . At the same time, different degrees of grafting can be simulated (from 0 to 100%) by considering the 12 beads of the icosahedral particle as representing bare silica or the grafted chains, respectively. As in CG-I simulations, the free PS chain is modelled as a string of P_M beads of $131N_{DPD}$.

All simulations were performed using DPD method with periodic boundary conditions imposed in the three directions in a $35rc \times 35rc \times 35$

rc cubic box. Overall adimensional density was set to $\rho = 3$. More than $7 \cdot 10^6$ DPD steps were carried out in each DPD simulation using a time step of $\Delta t = 0.04$, depending on the system concerned. All simulations were performed with an in-house developed code.^[33]


5.3 Results and discussion

As we already described before, we started mesoscale model generation with the free polymer chain, we mapped the real polymer chain onto a chain consisting of Kuhn segments. Consequently, each DPD bead represents a statistically correlated unit or Kuhn segment of the polymer. A DPD chain should, therefore, be made up of N_{DPD} beads, where $N_{DPD} = N_{mon} / C_\infty$ and N_{mon} is equal to the degree of polymerization of the molecular chain and C_∞ is its characteristic ratio and it has been obtained by the RIS-based procedure described in the previous paragraph. Figure 5.3 shows an example of the obtainment of N_b for a PS of 2 kDa from the corresponding value, as corrected for its temperature dependence.

C_∞ for 2K at 448K corrected for temperature effect to 358K:


 $C_{2K} \sim 4.5$
 $\frac{d \ln C}{dT} = 0.9 \times 10^{-3}$

The number of DPD beads for each PS 2K chain:



$$N_b = \frac{N}{C_{2K}} = 4$$

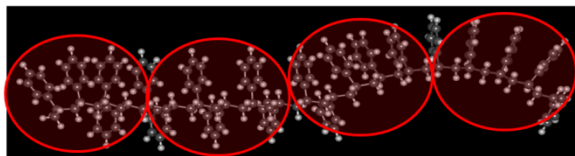


Figure 5.5: Mapping of a real 2 kDa PS chain onto the corresponding DPD chain via the corresponding temperature corrected value of C_∞ obtained as described above and illustrated in Figure 5.1.

The DPD nanocomposite model contains four species of different beads: one for the polymer chain (P_M) and two for the grafted PS chain-linker moiety (one for the linker head (L), and one for the PS tail (P_L)). The

lastone is for the silica surface (S). This is schematically illustrated in Figure 5.4.

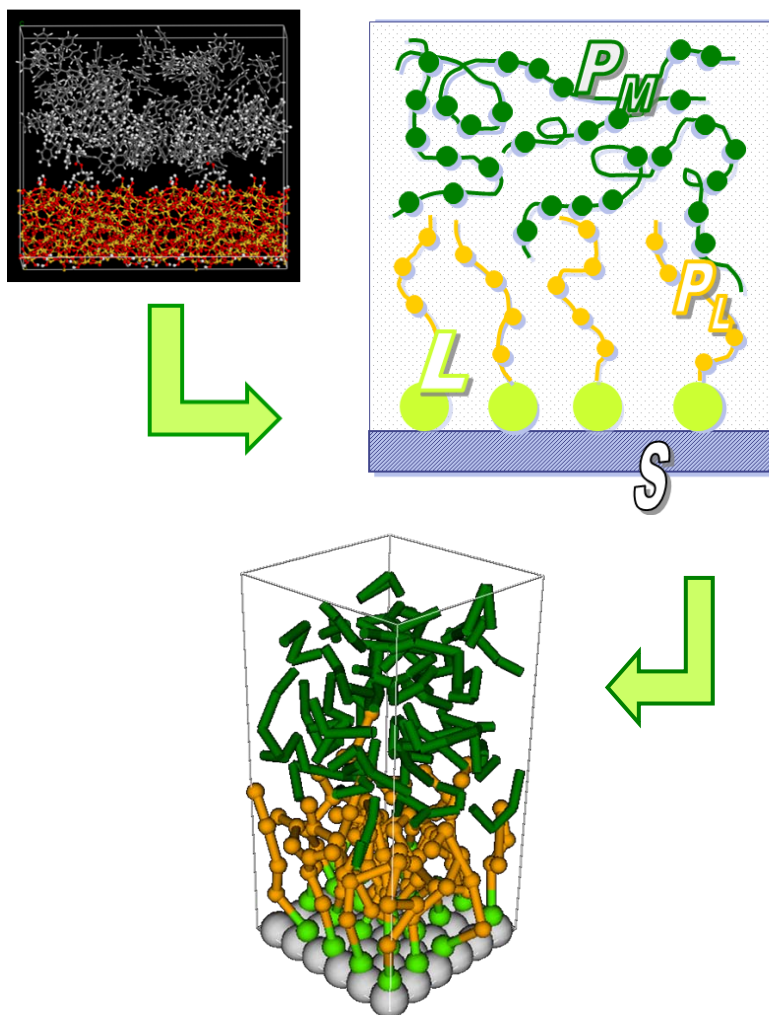


Figure 5.6: Mapping of the atomistic nanocomposite silica/linker-PS grafted chains/PS matrix chains model system onto the corresponding DPD model.

The interaction parameters needed as input for the mesoscale level DPD calculations have been obtained using a combinatorial approach to rescale the binding energies derived from the MD simulations. The bead-bead interaction parameter for the matrix PS-matrix PS interaction was set equal to $a_{\text{PMPM}} = 25$ in agreement with the correct value for a density value $\rho = 3$. In the case of silica/silica interaction, since no energy values could be

extracted from the MD simulations, we set $a_{SS} = 15$. Having fixed these two parameters, their values were then associated to the corresponding values of the DPD energies rescaled from MD simulations. All the remaining DPD interaction parameters a_{ij} could then easily be derived following this criterion. Finally, for the pair S/L the parameter a_{ij} was not calculated using the scaling law, but we set it to the value of 5, because of its strong negative value of the rescaled energy. The final set of DPD parameters, obtained from the scaling procedure starting from atomistic MD simulation energies are listed in Table 5.4.

The last step, enabling the running of DPD simulations consists in a further coarse-graining step, involving the lumping of the solid nanoparticle and its relevant grafted chains into one single nano-object. To this purpose, we adopted the following methodology. Each DPD grafted silica nanoparticle is modeled by an icosahedral structure, devised as being constituted by a central DPD bead, connected to 12 other DPD beads on each vertex of the icosahedrons, as shown in Figure 5.5. Each vertex of the icosahedron represents either a bare silica portion or a lumped PS-L grafted chain. The average diameter of the icosahedral nanoparticle is 15 nm.

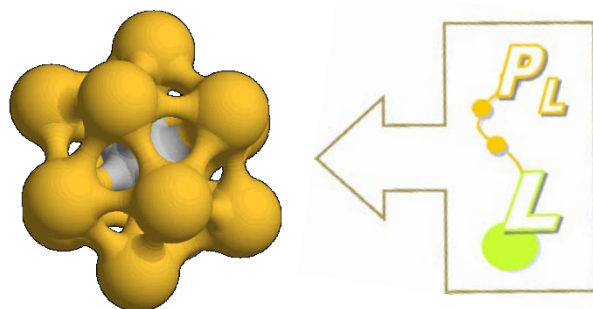


Figure 5.7: Icosahedral nanoparticle model representing the PS-linker grafted silica nanoparticle in our DPD simulations. Each vertex of the icosahedron represents a lumped PS-L grafted chain.

According to this model, different length of the grafted PS-L chains can be modulated by averaging the contribution of the corresponding a_{ij} parameters of all beads making up the PS-L chain. At the same time, different degrees of grafting can be simulated (from 0 to 100%) by considering the 12 beads of the icosahedral particle as representing bare silica or the grafted chains, respectively. Thus, taking

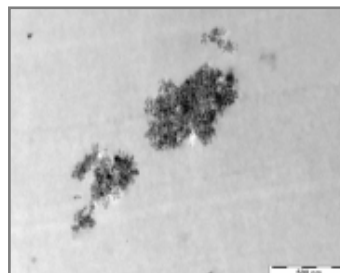
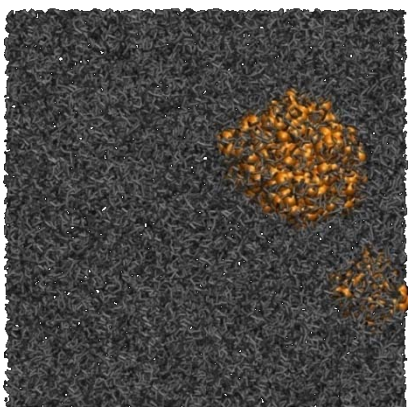
the PS-L of molecular mass equal to 2 kDa as an example, the DPD parameter of Table 5.4 were rescaled and set to the values shown in Table 5.5.

a_{ij}	H	P_M
H	25.4	26.6
P_M	26.6	19.6

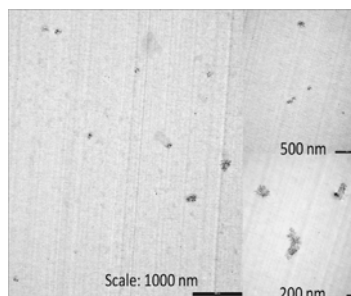
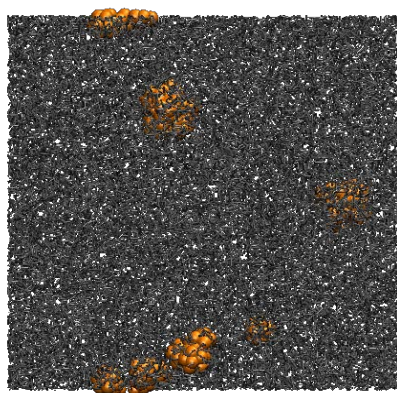
Table 5.5: DPD parameter set used to perform DPD simulations for a system in which the silica nanoparticles and the 2 kDa grafted PS-L chains are represented by icosahedral particles. In this case the surface coverage was considered equal to 100%.

5.3.1 Aggregation vs dispersion

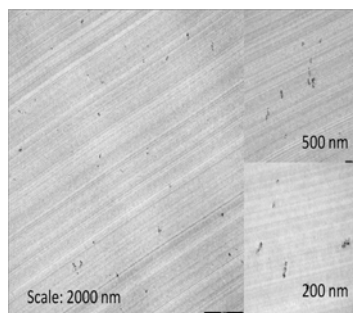
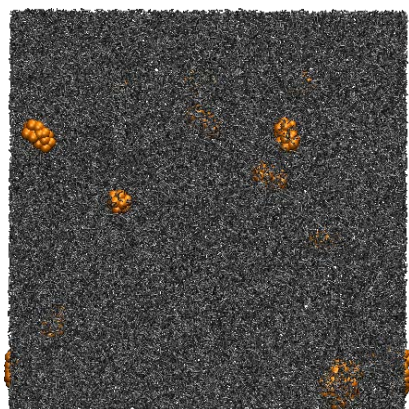
Figure 5.8 presents the DPD snapshots and the corresponding TEM images for all systems studied as listed in Table 5.2.



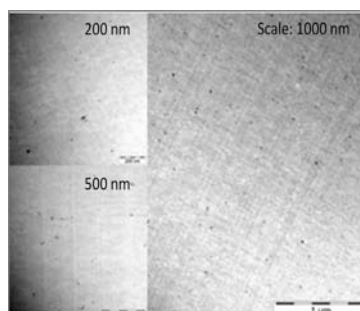
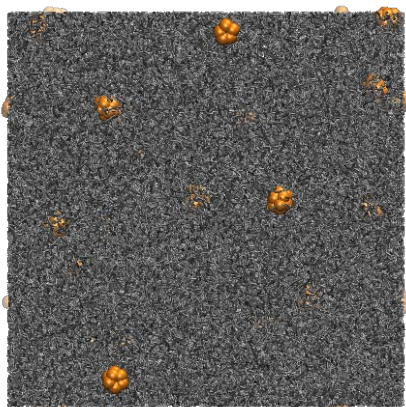
System 1: 0.25 % wt, 2.00 kDa and 0.51 chains/nm²



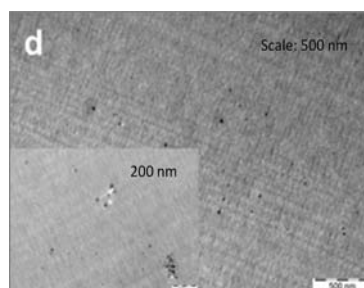
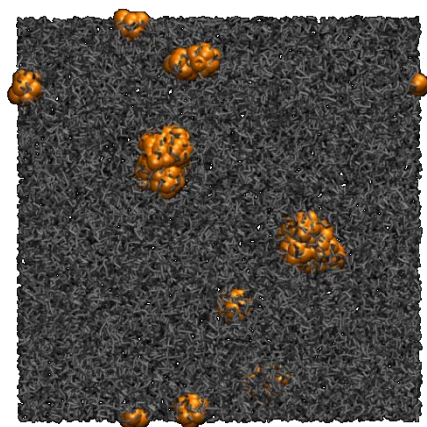
System 2: 0.25 % wt, 9.77 kDa and 0.40 chains/nm²



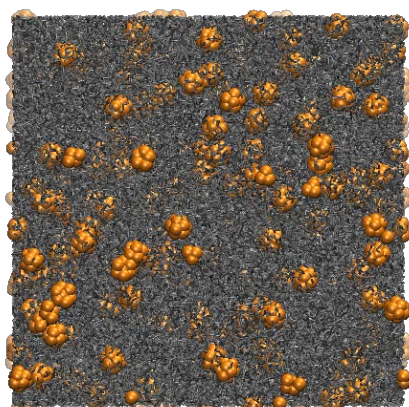
System 3: 0.25 % wt, 9.99 kDa and 0.55 chains/nm²



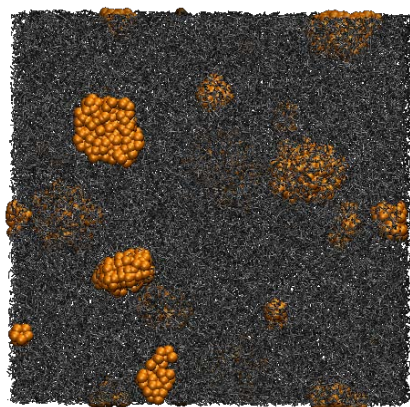
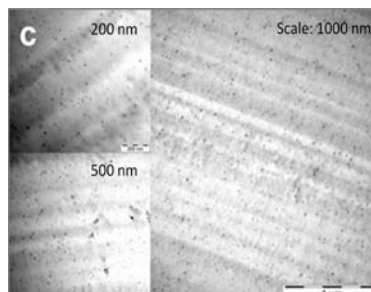
System 4: 0.25% wt, 10.61 kDa and 0.32 chains/nm²



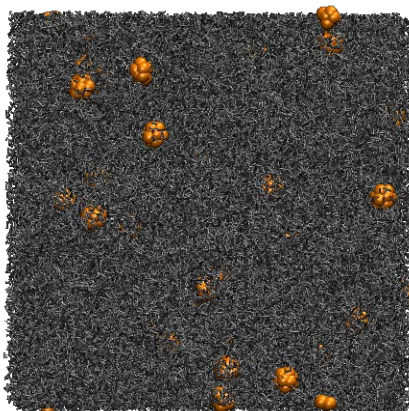
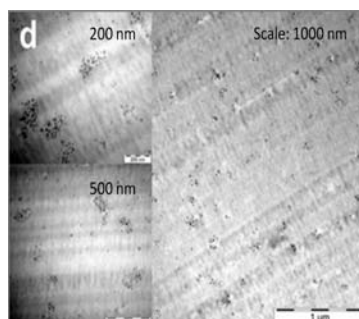
System 5: 0.25% wt, 20.67 kDa and 0.90 chains/nm²



System 6: 5.0 % wt, 20.61 kDa and 0.32 chains/nm²



System 7: 5.0 % wt, 20.67 kDa and 0.90 chains/nm²



System 8: 0.25 % wt, 103.5 kDa and 0.53 chains/nm²

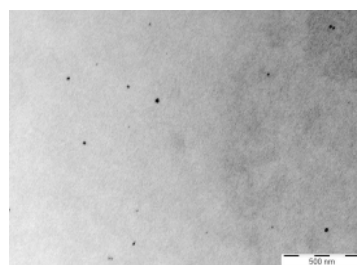


Figure 5.8: PS-silica NP (orange) dispersion/aggregation in PS matrix (grey) as obtained from the second level coarse-grained DPD simulation of all systems studied and the corresponding TEM images.

Pictures show that increasing grafted chains density leads from well dispersed NPs to aggregation. Contrariwise, increasing NP concentration from 0.25% wt to 5% does not alter dispersion. Moreover, increasing grafted chain length favors uniform distribution of NP in the matrix.

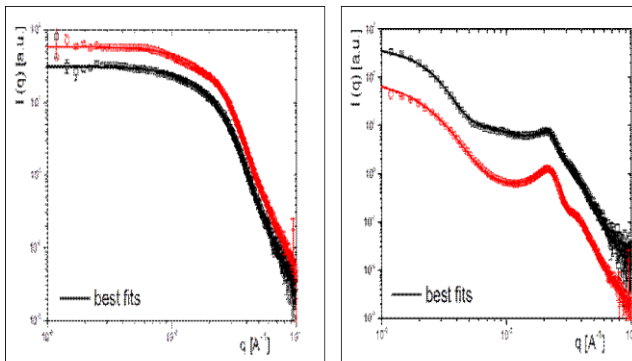


Figure 5.9: SAXS curves for system 4 with 0.25% wt and 0.32 chains/nm² (black line) and for system 6 with 5.0% wt and 0.32 chains/nm² (red line).

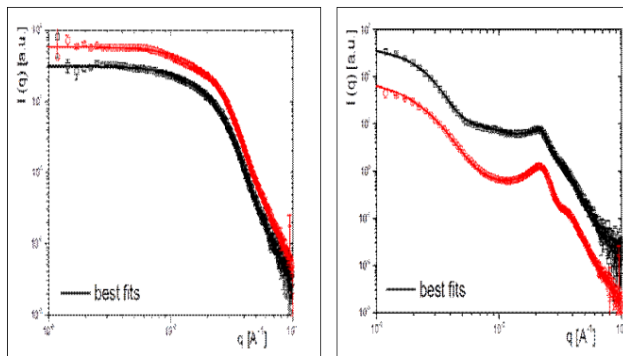


Figure 5.10: SAXS curves for system 5 with 0.25% wt and 0.90 chains/nm² (red line) and for system 7 with 5.0% wt and 0.90 chains/nm² (black line).

Figure 5.9 and Figure 5.10 report the SAXS results for the systems 4, 5, 6 and 7.

Comparing system 4 and 6 we can see that the scattered intensity $I(q)$ flattens as the magnitude of the scattering vector q approaches low values. This scattering behavior is characteristic of non interacting and uniformly dispersed NPs, from which the primary particle size $R=6.6\pm 1.8$ nm has been extracted through fitting a spherical form factor at high q -values. These observations are consistent with TEM evidences. Further, the surface roughness of the primary particle can be extracted from their Porod slope, $I_{\text{tot}}(q \rightarrow \infty) \sim q^{-4}$, thus corresponding to a smooth surface NP.

In the cases of system 5 and 7 the $I(q)$ shows a strong upturn in the low q region, the slope of which is indicative of aggregate structure. The similar shape of the scattering curves indicates minor effects of the filler concentration on the NP dispersion quality and allows the application of the same fitting model for both systems. Our fitting model considers the scattering of NPs partly under dilute conditions ($S(q)=1$), and partly in a high volume fraction phase. The concentrated phase corresponds to aggregates in which NPs are highly structured, as visible from the enhanced forward scattering and the development of a NP-NP correlation peak. Both NPs and aggregates are considered to behave as homogeneous spheres with log-normal size distributions for the fitting. From the fitting parameters and for both systems, we find a mean radius for spherical filler of $R=6.6\pm 2.5$ nm. At high- q values, curve follows a q^{-4} decay characteristic for smooth NP interfaces. The peaks at $q \sim 0.02 \text{ \AA}^{-1}$ originate from hard sphere structure factor of NPs in a high volume fraction phase. The mean center-to-center distance between neighboring NPs in the dense phase is about 28 nm with a volume fraction of 0.325. These dense phases are visible in the increase of the forward scattering and are assimilated to aggregates. No correlation between aggregates is observed ($S(q)=1$). An additional scattering contribution from diluted NPs is necessary to correctly fit the flat region between $q \sim 0.007 \text{ \AA}^{-1}$ and $q \sim 0.017 \text{ \AA}^{-1}$. In system 5, the contribution of these well dispersed single NPs is found significant ($n_{\text{NP}^{\text{single}}}/n_{\text{NP}^{\text{aggr}}} \sim 25\%$). In contrary, in system 7 basically all NPs are involved in aggregation ($n_{\text{NP}^{\text{single}}}=0$).

Analyzing SANS results, we obtain consistent information. An example of evolution of the SANS signal as a function of the grafting density is presented in the Figure 5.11. We can see that at high q , the scattering intensity decreases as q^{-4} . At low q , a remarkable point of these

two systems is the presence of a substantial upturn in intensity in the case of system 5 for q tending to 0. This suggests the presence of aggregates, as confirmed by SAXS and by TEM (see above).

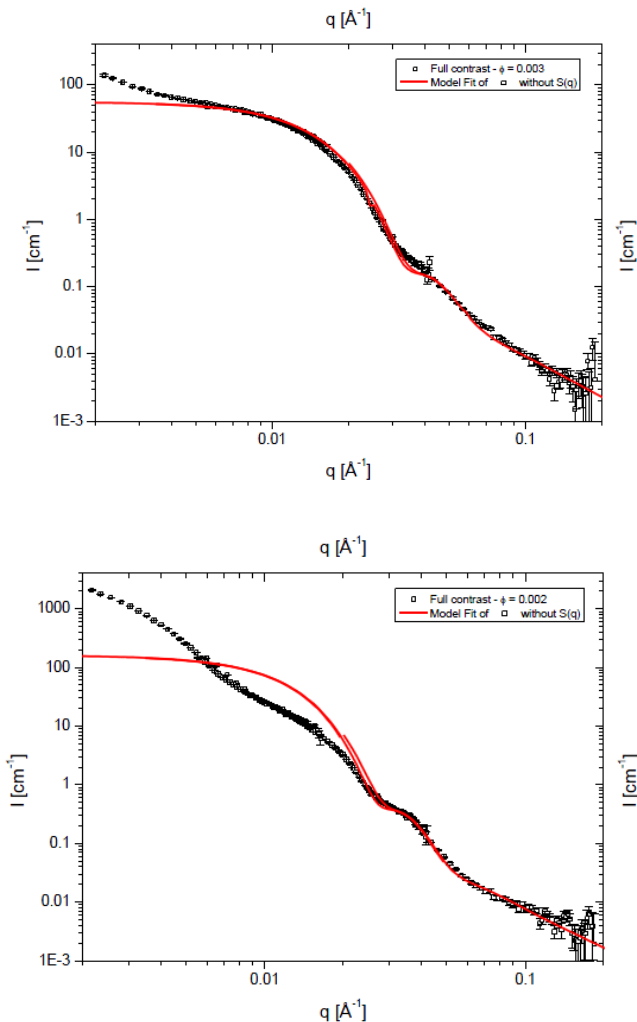


Figure 5.11: SANS curves for system 4 with 0.25 wt, 20.61 kDa and 0.32 chains/nm² (top) and for system 5 with 0.25 wt, 20.67 kDa and 0.90 chains/nm² (bottom).

A qualitative analysis of the data reveals for all samples an slight upturn at low q deviating from the expected flat scattering at q tending to 0. However for system 8, with a molecular weight of the grafted chain of 103.5 kDa, the deviation is less pronounced (Figure 5.12). This confirm that also the length of polymer grafted chains play a crucial role in the

aggregation/dispersion mechanisms. If we compare three systems with a similar grafted chain density but with very different molecular weight of polymer grafted chains, i.e. system 1 with NP of 2.0 kDa, system 4 with NP of 20.6 kDa and system 8 with NP of 103.5 kDa, we can observe that increasing grafted chain length favors uniform distribution of NP in the matrix (see Figure 5.8).

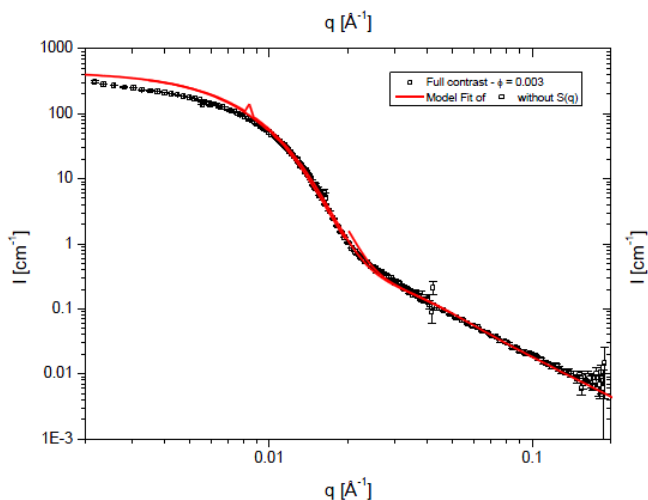


Figure 5.12: SANS curve for system 8 with 0.25% wt, 103.5 kDa and 0.53 chains/nm².

By coupling the experimental and computational evidences on the systems studied, we conclude that one of the key parameters controlling the aggregation/dispersion state of the silica/polystyrene nanocomposites is the density of the polystyrene chains grafted onto the silica nanoparticles ρ . Indeed, a minimum threshold value for chain length exists below which the interparticle interactions are no longer screened and the overall nanocomposite morphology presents extensive aggregation. However, independently of ρ , if the grafted chains are long enough the morphologies of the systems are predicted to be well-dispersed in the entire range of nanoparticle concentration considered.

5.3.2 Conclusions

The influence of several parameters (i.e. grafting chain length, grafting chain density, nanoparticle concentration) on the morphology of several nanocomposites were evaluated. Our computational procedure has been validated by scattering and imaging techniques. Thus the

structure-property relationships obtained constitute a rational for an optimal design of these systems; further, the knowledge of the fundamental phenomena stemming from this simulation-experimental combined approach could be applied to other nanostructured materials. Moreover we were able to characterize polymer grafted chains nanoparticles with very high grafting density, in a range that has not been investigated so far.

In the next future, the proposed procedure could be employed to predict aggregation behavior and macroscopic properties of alternative systems of industrial interest, featuring different type of nanoparticle, grafting chain length and density, nanoparticle concentration, and polymer matrix.

5.4 References

- [1] T. A. Vilgis, G. Heinrich, and M. Klüppel. Reinforcement of polymer nanocomposites: theory, experiments and applications. Cambridge Univ. Press, 2009.
- [2] A. Tuteja, M. E. Mackay, S. Narayanan, S. Asokan, and M. S. Wong. Breakdown of the continuum stokes-einstein relation for nanoparticle diffusion. *Nano Letters*, 7(5):1276–1281, May 2007.
- [3] K. I. Winey and R. A. Vaia. Polymer nanocomposites. *Mrs Bulletin*, 32(4):314–319, April 2007.
- [4] L. S. Schadler, S. K. Kumar, B. C. Benicewicz, S. L. Lewis, and S. E. Harton. Designed interfaces in polymer nanocomposites: A fundamental viewpoint. *Mrs Bulletin*, 32(4):335–340, April 2007.
- [5] E. Hübner, J. Allgaier, M. Meyer, J. Stellbrink, W. Pyckhout-Hintzen and D. Richter, *Macromolecules*, 2010, **43**, 856.
- [6] J. Kohlbrecher, SASFIT, Berlin Neutron Scattering Centre (BENS), Berlin, (2000).
- [7] N. T. Hu, E. Demiralp, T. Çagin and W. A. Goddard III, *J. Non-Cryst Solids*, 1999, **253**, 133.
- [8] D. A. Litton and S. H. Garofalini, *J. Appl. Phys.*, 2001, **89**, 6013.
- [9] A. Pedone, *J. Phys. Chem. C*, 2009, **113**, 20773.
- [10] G. S. Smith and L. E. Alexander, *Acta Cryst.*, 1963, **16**, 462.
- [11] Y. Qin, X. Yang, Y. Zhu, and J. Ping, *J. Phys. Chem. C*, 2008, **112**, 12815.
- [12] H. Sun, *Comput. Theo. Polym. Sci.*, 1998, **8**, 229.
- [13] H. C. Lay, M. J. S. Spencer, E. J. Evans, and I. Yarovsky, *J. Phys. Chem. B*, 2003, **107**, 9681.
- [14] G. Yiapanis, D. J. Henry, S. Maclaughlin, E. Evans, and I. Yarovsky, *Langmuir*, 2012, **28**, 17263.
- [15] W. Sun, Q. Zeng, and A. Yu, *Langmuir*, 2013, **29**, 2175.
- [16] D. N. Theodorou and U. W. Suter, *Macromolecules*, 1986, **19**, 139.
- [17] R. Toth, F. Santese, S. P. Pereira, D. R. Nieto, S. Pricl, M. Fermeglia and P. Posocco, *J. Mater. Chem.*, 2012, **22**, 5398.
- [18] G. Scocchi, P. Posocco, J.-W. Handgraaf, J. G. E. M. Fraaije, M. Fermeglia and S. Pricl, *Chem. Eur. J.*, 2009, **15**, 7586.

- [19] R. Toth, D.-J. Voorn, J.-W. Handgraaf, J. G. E. M. Fraaije, M. Fermeglia, S. Pricl and P. Posocco, *Macromolecules*, 2009, **42**, 8260.
- [20] R. Toth, M. Ferrone, S. Miertus, E. Chiellini, M. Fermeglia and S. Pricl, *Biomacromolecules*, 2006, **7**, 1714.
- [21] K. S. Katti, D. Sikdar, D. R. Katti, P. Ghosh and D. Verma, *Polymer*, 2006, **47**, 403.
- [22] F. Gardebien, J.-L. Bredas and R. Lazzaroni, *J. Phys. Chem. B*, 2005, **109**, 12287.
- [23] D. R. Paul, Q. H. Zeng, A. B. Yu and G. Q. Lu, *J. Colloid Interface Sci.*, 2005, **292**, 462.
- [24] R. Toth, A. Coslanich, M. Ferrone, M. Fermeglia, S. Pricl, S. Miertus and E. Chiellini, *Polymer*, 2004, **45**, 8075.
- [25] M. Fermeglia and S. Pricl, *Prog. Org. Coat.*, 2007, **5**, 187.
- [26] (a) P. J. Hoogerbrugge and J. M. V. A. Koelman, *Europhys. Lett.*, 1992, **18**, 155; (b) J. M. V. A. Koelman and P. J. Hoogerbrugge, *Europhys. Lett.*, 1993, **21**, 363; (c) R. D. Groot and P. B. Warren, *J. Chem. Phys.*, 1997, **107**, 4423.
- [27] The Chemistry Unified Language Interface (Culgi), version 5.0, Culgi B.V., The Netherlands (2004-2010).
- [28] G. Scocchi, P. Posocco, M. Fermeglia and S. Pricl, *J. Phys. Chem. B*, 2007, **111**, 2143.
- [29] M. Maly, P. Posocco, S. Pricl and M. Fermeglia, *Ind. Eng. Chem. Res.*, 2008, **47**, 5023.
- [30] E. E. Keaveny, I. V. Pivkin, M. Maxey and G. E. Karniadakis, *J. Chem. Phys.* 2005, **123**, 104107.
- [31] J. E. Mark, Ed. *Polymer Data Handbook*; Oxford University Press:New York, 1999.
- [32] (a) P. Posocco, Z. Posel, M. Fermeglia, M. Lísal and S. Pricl, *J. Mater. Chem.*, 2010, **20**, 10511; (b) Z. Posel, P. Posocco, M. Fermeglia, M. Lísal and S. Pricl, *Soft Matter*, 2013, **9**, 2936.
- [33] (a) M. Lísal, and J. K. Brennan, *Langmuir*, 2007, **23**, 4809; (b) Z. Posel, M. Lísal and J. K. Brennan, *Fluid Phase Eq.* 2009, **283**, 38; (c) P. Petrus, M. Lísal and J. K. Brennan, *Langmuir*, 2009, **23**, 4809; (d) P. Petrus, M. Lísal and J. K. Brennan, *Langmuir*, 2010, **26**, 14680-14693.

6

Conclusions

The development of new multifunctional materials necessitates a comprehensive understanding of the phenomena at different time and length scales. In the past decade or so, this need has significantly stimulated the development of computer modeling and simulation, either as a complementary or alternative technique to experimentation. In this connection, many traditional simulation techniques (e.g., MC, MD, BD, LB, Ginzburg–Landau theory, micromechanics and FEM) have been employed, and some novel simulation techniques (e.g., DPD, equivalent-continuum and self-similar approaches) have been developed to study polymer nanocomposites. These techniques indeed represent approaches at various time and length scales from molecular scale, to and then to macroscale, and have shown success to various degrees in addressing many aspects of polymer nanocomposites.

In recent years, the advent of ever more powerful, massively parallel computers, coupled with spectacular advances in the theoretical framework that describes materials, has enabled the development of new

concepts and algorithms for the computational modeling of materials. As the field of computational materials science develops and matures, the notion is taking hold in the community that modeling efforts should be an integral part of interdisciplinary materials research and must include experimental validation.

The simulation techniques developed so far have different strengths and weaknesses, depending on the need of research. For example, molecular simulations can be used to investigate molecular interactions and structure on the scale of 0.1–10 nm. The resulting information is very useful to understanding the interaction strength at nanoparticle–polymer interfaces and the molecular origin of mechanical improvement. However, molecular simulations are computationally very demanding, thus not so applicable to the prediction of mesoscopic structure and properties defined on the scale of 0.1–10 μm , for example, the dispersion of nanoparticles in polymer matrix and the morphology of polymer nanocomposites. To explore the morphology on these scales, mesoscopic simulations such as coarse-grained methods, DPD and dynamic mean field theory are more effective. On the other hand, the macroscopic properties of materials are usually studied by the use of mesoscale or macroscale techniques such as micromechanics and FEM. But these techniques may have limitations when applied to polymer nanocomposites because of the difficulty to deal with the interfacial nanoparticle–polymer interaction and the morphology, which are considered crucial to the mechanical improvement of nanoparticle-filled polymer nanocomposites.

In recent years, the advent of ever more powerful, massively parallel computers, coupled with spectacular advances in the theoretical framework that describes materials, has enabled the development of new concepts and algorithms for the computational modeling of materials. As the field of computational materials science develops and matures, the notion is taking hold in the community that modeling efforts should be an integral part of interdisciplinary materials research and must include experimental validation.

Therefore, despite the progress over the past years, there are a number of challenges in computer modeling and simulation. In general, these challenges represent the work in two directions. First, there is a

need to develop new and improved simulation techniques at individual time and length scales. Secondly, it is important to integrate the developed methods at wider range of time and length scales, spanning from quantum mechanical domain to molecular domain, to mesoscopic domain, and finally to macroscopic domain, to form a useful tool for exploring the structural, dynamic, and mechanical properties, as well as optimizing design and processing control of polymer nanocomposites.

Several examples have been reported in this work showing different methodologies and describing different simulation protocols to study various aspects of polymer nanocomposite materials and coatings. A general good agreement in the comparison with experimental data of the results is obtained, thus showing that the molecular simulation modeling is a mature tool that may be used in the design and development of new coatings. Advances in computational materials science in general will continue to facilitate the understanding of materials and materials processing, the prediction of properties and behavior, and the design of new materials and new materials phases, thus facilitating the application of process system engineering to more sophisticated and innovative processes.